Synthesis and Studies of II-VI and IV-VI Nanostructured Compound Semiconductors and Some Conjugated Polymers

A Thesis Submitted

By

Gouri Sankar Paul

Roll No: 05615103

In Partial Fulfillment of the Requirements for the Award of the Degree of

Doctor of Philosophy

Centre for Energy
Indian Institute of Technology Guwahati
Guwahati-781 039, Assam, INDIA

March, 2010

Statement

The work contained in the thesis entitled **"Synthesis and Studies of II-VI and IV-VI Nanostructured Compound Semiconductors and Some Conjugated Polymers"** has been carried out by me under the supervision of Dr. Pratima Agarwal, Associate Professor, Department of Physics & Centre for Energy, Indian Institute of Technology Guwahati, Assam, India. This work has not been submitted elsewhere for the award of any degree.

3rd March, 2010

(Gouri Sankar Paul)
Centre for Energy
Indian Institute of Technology Guwahati
Guwahati – 781 039, Assam, India.

Certificate

It is certified that the work contained in the thesis entitled **"Synthesis and Studies of II-VI and IV-VI Nanostructured Compound Semiconductors and Some Conjugated Polymers"** submitted by Mr. Gouri Sankar Paul, a Ph.D. student of the Centre for Energy, Indian Institute of Technology Guwahati, Assam, India for the award of the degree of *Doctor of Philosophy* has been carried out under my supervision. This work has not been submitted elsewhere for the award of any degree.

3rd March, 2010

(Dr. Pratima Agarwal)
Associate Professor
Department of Physics & Centre for Energy
Indian Institute of Technology Guwahati
Guwahati – 781 039, Assam, India.

Dedicated

to

My Family for their Love and

Encouragement

Acknowledgements

First and foremost, I would like to thank my thesis supervisor, Dr. Pratima Agarwal for her support, understanding and patience during the past four years over this project. Without her guidance as a great mentor, this work would not have been possible, and I certainly wouldn't be here. It has been a great experience working with her. I will never forget her cool and down to earth behavior. The way she guided me, and the way she preceded with my thesis, it was a learning experience for me. Not only did I learn the subject from her that included diverse subjects like experimental techniques, condense mater physics, solar photovoltaic and other advanced physics topics, but, numerous things in my personal life also. It was really incredible learning all these till the time of my thesis submission.

I would also like to thank Dr. P. K. Iyer, Associate Professor, Department of Chemistry, IIT Guwahati for his guidance during the synthesis of conjugated conducting polymers.

I would also like to offer my thanks to the doctoral committee (DC) members, Prof. P. Mahanta (Chairman), Prof. A. Srinivasan and Dr P. K. Iyer for their fruitful suggestions that helped to improve the quality of my work.

My special gratitude goes to my fellow lab mates, Mrs. Purabi. Gogoi, Mr. J. Anto Pradeep and Mr. Himansu Shekhar Jha. They themselves have made the environment, interesting to work. I am also thankful to Mr. Pranjol Jyoti Sarmah and Mr. Gunin Saikia, research scholars, Department of Chemistry, IIT Guwahati for their support during polymer synthesis.

I am thankful to central workshop, engineering section for their cooperation and, central instrumental facility (CIF), IIT Guwahati, for enabling me to avail several sophisticated instruments to perform the experiments. I am thankful to Mr. Chandan Borgohain, Mr. Kula Kamal Senapati (Scientific Officers) and Mr. Madhurjya Borah (Junior Technical Superintendent), CIF for their help. I am also thankful to Centre for Nanotechnology, IIT Guwahati for extending X-ray diffractometer facility and Department of Chemical Engineering for Thermo Gravimetric Analysis.

I am thankful to all research scholars of Centre for Energy for pleasant memories had with them. Here, I would also like to thank Mr. Pankaj Kalita and Mrs. Lepaksi Barbara (Scientific Officers) for their friendly behavior and cooperation. I wish to thank Mrs.

Archana Rajbanshi (Junior Assistant) and Mr. Dhiren Hujuri (Junior Technical Superintendent) of our Centre for their help.

I thank to Mr. Debabrata Mishra and all my friends for the memorable life in IITG campus.

Without the love and support of my family, this would have been a very hard journey. I thank my father for teaching me good values such as hard work and appreciation for the gift of life and my mother without whom I would not be the person that I am today. My love for them is eternal. My sincere gratitude to my two younger brothers Umasankar and Shibsankar for their supports. Finally, I am grateful to my wife and soulmate, Nabanita, for giving me an unwavering love and support.

Last but not the least, I am grateful to Indian Institute of Technology Guwahati and Council of Scientific and Industrial Research (CSIR, SRF), Govt. of India, for giving me the financial support to carry out the present thesis work.

Gouri Sankar Paul

IIT Guwahati, INDIA, March 2010

Preface

The II-VI, IV-VI groups' nanocrystalline compound semiconductors and conjugated polymers have been the subject of extensive research both in fundamental studies and for potential applications in devices. The broad range of band gaps and lattice constants available from these materials, and the unique fundamental phenomena they exhibit, make them attractive for a wide range of applications such as infrared lasers and detectors, blue-green lasers and light emitting diodes (LEDs), nonlinear optical materials, magneto-optical devices, radiation detectors and photovoltaic devices.

In II-VI compound semiconductors, CdS and ZnS are the prime attention of current researchers due to following properties: direct band gap, high absorption coefficient, good conversion efficiency, high thermal stability and easy to synthesize. Due to the wide band gap, CdS (2.41 eV) and ZnS (3.61 eV) are used as a window layer as well as n-type semiconducting material in heterojunction solar cells. Whereas, IV-VI compound semiconductors, like SnS and PbS usually exhibits p-type conduction and are reported to have a direct band gap of about 1.32 eV for SnS and 0.41 eV for PbS. This phenomenon shows that SnS and PbS have appropriate electrical and optical features for use in solar cells. Additionally, SnS has the advantage of its constituent elements being abundant in nature and not posing any health and environmental hazards. It's narrow band gap (1.32 eV) is ideal for photoelectric energy conversion. Therefore, SnS can be potentially used as a p-type material in thin film solar cells and as an electrode in lithium ion batteries. PbS also exhibits unique structural and electronic properties, which make it potential candidate for different technological applications, e.g., thermoelectric, optoelectronic and spintronic devices. Its importance for long-wavelength sensors, infrared diode lasers, and thermo-photovoltaic energy converters has been recognized during the last decades.

Semiconducting conjugated polymers like **p**oly **p**ara-**p**henylene (PPP) and **p**oly**f**lourene (PF) and their derivatives have also attracted attention of current researchers because of their potential applications in light emitting devices, photovoltaic cells, organic lasers, rechargeable batteries, all polymer field effect transistors and ion exchange membranes combined with attractive material properties such as low weight and ease of processing. Conductivity of these polymers, which are otherwise highly insulating, can be enhanced by several orders of magnitude by doping with metals and other compounds making them useful for device applications. Composites of nanoparticles and conjugated

polymers are interesting as they enhance the electroluminescence and electrical properties by encompassing the properties of both materials.

In my research work, I have prepared CdS, ZnS, SnS and PbS nanostructures by Solvothermal process whereas PPP and PF conjugated polymers have been prepared by oxidative polymerization technique and Suzuki coupling process respectively. Nanostructured and polymer based thin films have been prepared by doctor blade technique and drop casting technique respectively. I have also fabricated p-SnS/n-CdS based heterojunction solar cells and different physical parameters are obtained.

The above samples are characterized by using X-ray diffraction (XRD), Transmission electron microscopy (TEM), Scanning electron microscopy (SEM) and Energy dispersive spectrum (EDS). Thermal stability of these materials is carried by Thermo gravimetric analysis (TGA). Temperature dependence of dark and photoconductivity, rise and decay of photocurrents, persistent photocurrents and intensity variation of photoconductivity are also measured to understand the electrical properties of these materials.

The present thesis is divided into seven chapters, namely,

(1) Introduction (2) Experimental Details (3) Synthesis and studies of II-VI nanostructured semiconductors (4) Synthesis and studies of IV-VI nanostructured semiconductors (5) Synthesis and studies of conducting polymers blend with nanostructured semiconductors (6) Fabrication and studies of nanostructured p-SnS/n-CdS based heterojunction solar cells (7) Summary and Conclusions.

Chapter 1 serves as a general introduction to the materials of interest to this thesis work. Here, I have mainly discussed about the different types of compound and organic semiconductors and their important properties and various applications. Basic differences between bulk and nanocrystalline semiconductors have been discussed.

Chapter 2 has been devoted to experimental details, where the method of material preparation and physical characterizations such as structural, optical, thermal stability and electrical conductivity discussed. Here I have also discussed different models which I have used during this thesis work.

In Chapter 3, the results and discussions on CdS and ZnS nanostructures prepared for different reaction times have been presented. Typical diameter of the CdS nanorods powder samples is found to vary from 10-50 nm and length from 80-750 nm. In optical absorbance spectra, a peak is observed at 488 nm which is basically due to the band to band absorption of the CdS nanorods. CdS nanorods thin films also show a sharp emission peak at 520 nm. Thermal stability studies on these as-synthesized powder samples have shown that CdS

nanorods are stable up to 650 °C. Electrical transport measurements done on CdS films in coplanar geometry show thermally activated dark conductivity. The films show a good photosensitivity ($S= \sigma_L/ \sigma_d$) ≈ 10^5 at 300 K (under ~ 10 mW/cm^2 light from halogen lamp), which is decreased to 5.76 at 453 K. An increase in photocurrent is observed with time at all temperature. Further, the photocurrents do not instantaneously drop to dark value after cutting off the light. Rather, a rapid decrease followed by a slow decay of photo current is observed. There is always a persistent photocurrent (PPC) at all temperatures which do not go to zero even for a long time after the light pulse is cut off. During each subsequent light exposure, the photocurrent is found to be larger than earlier value and the PPC is also found to be larger than the previous value. The rise and decay of photocurrent do not appear to be due to presence of traps as the decay time τ_1 and τ_2 are found to increase with increase in temperature. A model with homogeneous potential fluctuation of conduction and valence band edge has been proposed to explain the decay phenomenon. In the model, a fraction of photogenerated carriers are separated before recombination, thus giving rise to the PPC. Whereas, as-synthesized ZnS powder samples consist of disc like nanoparticles with diameters varying from 50 nm to several micrometers and surface morphology and crystallinity of the ZnS powder samples are improved with reaction times. A broad emission peak is observed at 363 nm (3.42 eV) for all the samples along with two sharp peaks at 422 nm and 439 nm for excitation wavelength at 250 nm. The broad emission peak at 363 nm for 250 nm of excitation wavelength is slightly blue shifted to 355 nm (3.49 eV) in case of 300 nm of excitation wavelength. The peaks observed at 355 and 363 nm for two different excitation wavelengths are assigned to excess Zn^{2+} and S^{2-} in ZnS. The additional peaks observed at 422 and 439 nm could be due to interstitial and vacancy states of sulfur in ZnS as observed for colloidal ZnS nanocrystals. The I-V characteristics of the ZnS nanostructured thin films (sandwich geometry) prepared for 5 h samples is measured using silver paste as top electrode which forms an ohmic contact with the ZnS. The dark conductivity for these nanostructure thin films is of the same order as that of bulk samples. The thermal activation energy for the dark and photoconductivity is calculated as 1.68 eV and 1.5 eV respectively (the illumination intensity for 10 mW/cm^2). The dark activation energy is nearly half of the band gap energy (close to the Fermi level), suggesting that ZnS thin films are intrinsic in nature.

In Chapter 4, the results and discussions on SnS and PbS nanostructures prepared for different reaction times have been presented. As-synthesized SnS powder samples consist of nanoflakes with thickness varying from 50-80 nm and length from 200 nm to several

micrometers. From TGA curves it is observed that SnS powder samples are stable up to 620 °C. The dark conductivity of the SnS thin films prepared by doctor blade technique show thermally activated behavior in the temperature range from room temperature to 463 K. The activation energy from the slope of the ln σ vs 1000/T is found to be nearly 0.48 eV suggesting the conduction via deep acceptor levels associated with the excess of tin atoms for these films. Whereas, the average particle size of the PbS nanocubes is found to vary from 25–300 nm with an increase in size with increasing reaction times. PbS nanocubes show good photoluminescence properties. The emission spectrum shows a broad peak at around 310 nm along with two relatively narrow peaks at 358 nm and 384 nm and a shoulder at around 430 nm for 250 and 300 nm of excitation wavelengths. PbS nanocubes are stable up to 700 °C. After 900 °C, some amount of weight loss is observed, which could be due to the evaporation of sulfur from the broken PbS bonds. The I-V characteristics of the PbS thin films using silver paste exhibits ohmic nature. The conductivity is nearly constant in the temperature range 300-450 K. This is due to its low band gap. The films do not show any photoconductivity for the visible photon flux, which is not surprising as PbS is known to be material for IR detector.

In Chapter 5, the results and discussions on PPP, PF and their blends with semiconducting nanomaterials have been presented. Both PPP and PF shows blue luminescence and are suitable for blue LEDs. The thermal stability of PPP is enhanced by adding CdS nanoparticles. The virgin PPP films are found to be highly insulating ($\sigma \approx 10^{-13}$ Ω^{-1} cm^{-1}) near room temperature. When doped with CdS nanoparticles, conductivity is enhanced by several orders of magnitude near room temperature. The activation energy for polymer blend in the range 333 to 403 K is found to be 0.68 eV. Above 403 K, when conductivity is ~ 10^{-4} Ω^{-1} cm^{-1}, the activation energy is decreased to 0.08 eV. Structural and morphological properties of the PF and its nanostructured blends are also studied. The absorption peaks located in the range from 378 to 390 nm are due to π-π* transition of conjugated polyfluorene backbone. Onsets of absorption spectra of the PF incorporated with nanostructured materials is found to have shifted to 393 nm (corresponding band gap 3.16 eV) in dilute chloroform solution, whereas in thin film, absorption peaks are centered at 390 nm. In emission spectroscopy, two peaks are observed at 411 and 433 nm respectively for pure PF in dilute chloroform solution for the excitation wavelength of 370 nm. In case of thin films, emission peaks are observed at 421 and 441 nm respectively. In comparison with dilute solutions, the emission spectra of polymers in film state are slightly red shifted and can be

attributed to the aggregation of polymer chains. For all the samples, I-V curves are straight lines passing through origin and suggest that evaporated Al forms an ohmic contact with polymer and its nanocomposites blends. Pure PF shows conductivity around ~10^{-11} $\Omega^{-1}cm^{-1}$ at 300 K. After incorporation of nanostructured materials in PF matrix, the dark conductivity of their blends has increased slightly.

Chapter 6 deals with p-SnS/n-CdS nanostructured based heterojunction solar cells. CdS and SnS films are deposited by doctor blade technique on ITO coated glass substrates. Silver paste is used as a back contact and ITO is used as a transparent electrode. Typical parameters for these solar cells under illumination of 100 mW/cm^2 are: Open circuit voltage (V_{OC}) = 100 mV, short circuit current (I_{SC}) = 240 μA, fill factor (FF) = 0.52, series resistance (R_S) = 166 Ω, shunt resistance (R_{Sh}) = 2 kΩ and efficiency (η) of 0.32%. Spectral response curve indicates that around 75% of incident photons are absorbed in the wavelength range of 500-600 nm. It is observed that efficiency of the cells depends on the thickness of the CdS and SnS layers. As the thickness of SnS layers is increased efficiency increase.

Summary, conclusions and scope for future work on these materials are presented in the last chapter. Important physical parameters of the CdS, ZnS, SnS and PbS are given in Appendix I. The papers published in journals and conference proceedings during this present thesis work are listed at the end of the thesis.

List of Abbreviations used in this Thesis

eV Electron Volt

en Ethylenediamene

CdS Cadmium Sulfide

ZnS Zinc Sulfide

SnS Tin Sulfide

PbS Lead Sulfide

PPP Poly (para-phenylene)

PF Polyfluorene

LED Light Emitting Diode

XRD X-ray diffraction

TEM Transmission Electron Microscopy

SEM Scanning Electron Microscopy

EDAX Energy Dispersive Analysis of X-ray

UV-Vis-NIR Ultraviolet-Visible-Near Infra Red

PL Photoluminescence

PLE Photoluminescence Excitation

TGA Thermo Gravimetric Analysis

SDTA Simultaneous Differential Thermal Analysis

DTG Derivative Thermogravimetry

GPC Gel Permission Chromatography

PDI Poly Dispersity Index

DMSO Dimethyl Sulfoxide

THF Tetrahydrofuron

NMR Nuclear Magnetic Resonance

PC Photoconductivity

PPC Persistent Photoconductivity

SR Spectral Response

List of Symbols used in this Thesis

σ Conductivity

Ω Ohm

λ Wavelength

θ Bragg's angle

D Grain size

β Full-width at half-maximum

δ Dislocation density

N Number of crystallites per unit area

ε Strain

μ Micron

h Planck's Constant

k Boltzmann's Constant

Å Angstrom

ν Wave number

°**C** Degree Celsius

T Temperature

K Kelvin

α Absorption Coefficient

ε_0 Dielectric Constant

η Efficiency

Table of Contents

Content **Page No.**

List of Figures

Chapter 1:

Chapter 2:

Chapter 3:

Chapter 4:

Chapter 5:

Chapter 6:

List of Tables

Chapter 2:

Chapter 3:

Chapter 4:

Chapter 5:

Chapter 6:

CHAPTER-1

Introduction

Chapter 1: Introduction

A semiconductor is usually defined rather loosely as a material with electrical resistivity lying in the range of 10^{-2}-10^{9} Ω cm. Alternatively, it can be defined as a material whose energy gap for electronic excitations lies between zero and about 4 eV. The best-known semiconductor is undoubtedly silicon (Si). However, there are many semiconductors besides silicon. In fact, many minerals found in nature, such as zinc-blende (ZnS), cuprite (Cu_2O) and galena (PbS), to name just a few, are semiconductors. Including the semiconductors synthesized in laboratories, the family of semiconductors forms one of the most versatile classes of materials known to scientific community.

During the recent decades, advances in semiconductor materials are resulted in the development of a wide range of electronic and optoelectronic devices that affects many aspects of the technological society. From semiconductors to microelectronic and optoelectronic devices (i.e., integrated circuits and devices for the generation and detection of light) for information applications (i.e., computing, memory storage, and communication), these advances and applications are catalyzed by an improved understanding of the interrelationship between different aspects (i.e., structure, properties, synthesis and processing, performance, and characterization of materials) of this multidisciplinary field.

Due to high manufacturing cost of Si, the solar photovoltaic and other optoelectronic devices made by crystalline Si is very high. For this reason current researchers are looking for low cost materials for device fabrications. Among them II-VI and IV-VI semiconductors and organic semiconductors are very useful and have wide applications due to low cost, high thermal stability and easy to syntheses.

1.1. Compound Semiconductors

A compound semiconductor is a semiconductor compound composed of elements from two or more different groups of the periodic table. Compounds formed from elements of the groups II-VI (such as CdS, CdTe, CdSe, ZnS, ZnTe, ZnSe), III-V (GaAs, InP), IV-VI (SnS, SnSe, PbS, PbSe) of the periodic table have properties very similar to their group IV counterparts. In going from the group IV elements to the II-VI, III–V and IV-VI compounds, the bonding becomes partly ionic due to transfer of electronic charge from the group II, III and IV atoms to the group IV, V and VI atoms. The ionicity causes significant changes in the

semiconductor properties. It increases the Coulomb interaction between the ions and also the energy of the fundamental gap in the electronic band structure. The ionicity becomes even larger and more important in the II–VI compounds such as CdS and ZnS. As a result, most of the II–VI compound semiconductors have band gaps larger than 1 eV and are also important for photovoltaic and others optoelectronic device applications [1.1]. The large ionicity of the binary compounds formed from group IV and VI elements, such as PbS, PbTe and SnS also favors six-fold coordinated ions. They are similar to the mercury chalcogenides in that they have very small band gaps inspite of their large ionicity. These small band gap IV–VI semiconductors are also important as infrared detectors and others optoelectronic device applications [1.1].

1.1.1 Nanostructured Semiconductors

If the geometrical extent of a semiconductor, typically embedded in the matrix of another semiconductor, is reduced in one, two or three directions of space below the size of the "de Broglie wavelength" of a charge carrier—in other words, if it is reduced in size to only a few nanometers—it is a *nanostructure*. Reduction of dimensionality in one, two or three directions leads to quantum wells, wires or dots, respectively. The electronic, and to a lesser extent, the vibronic properties of low-dimensional structures (including their interactions such as electron–electron, electron–hole and electron–phonon interaction) depend qualitatively on the dimensionality of the structure and quantitatively on details of the geometry of the structure (its size and shape) and of the distribution of atoms inside. The electronic properties in turn control the linear and nonlinear optical and transport properties. Thus "geometrical architecture" opens enormous opportunities for designing completely novel materials or heterostructures. These opportunities extend far beyond the well-known "chemical architecture", where properties are modified by varying the chemical composition.

Radically different from three-, two-, and one-dimensional structures in their electronic properties are zero-dimensional structures: quantum dots. Their "density of electronic states" is described by delta-function and they show no dispersion of energy, thus resembling an atom in a dielectric matrix instead of a classical semiconductor. The Hamilton and momentum operators of quantum dots do not commute, leading again to novel physical properties. Figure 1.1 show the variation of the density of states in structures of varying dimensionality.

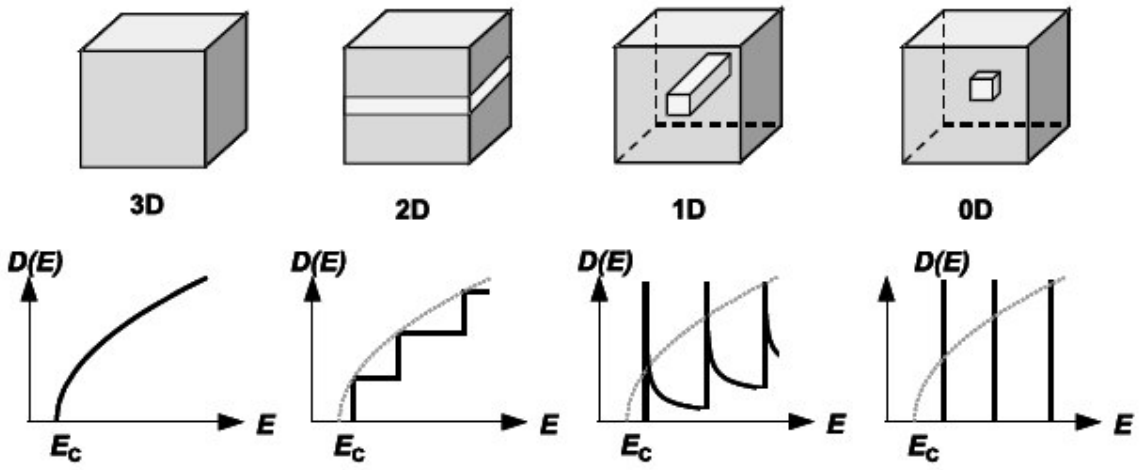

Figure 1.1: Top: Schematic representations of three-, two-, one- and zero-dimensional heterostructures; Bottom: Densities of electronic states for the given case of dimensionality [1.2].

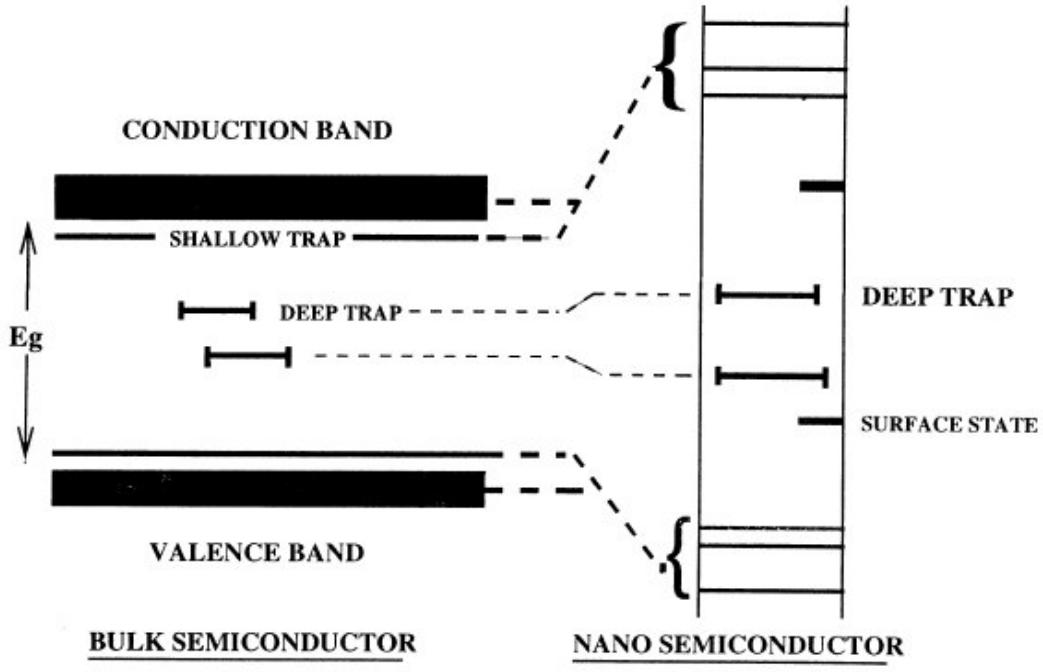

Figure 1.2: The energy level diagram of a bulk and a nanocrystalline semiconductor. Surface states arising due to increased surface-to-volume ratio is shown in the figure [1.3].

Physics of nanocrystalline states has been of great research interest because of their potential uses and applications in several branches of science and technology. Several methods both physical and chemical have been reported for synthesizing nanosized clusters of metals as well as semiconductors [1.4]. A variety of physical properties of nanosized metals and semiconductors have been reported in the literature. Due to the quantum

confinement phenomenon, the physical and chemical properties of these nanomaterials are very different from their bulk counterparts. The energy band diagram of a nanoparticles and the bulk counterpart is shown in Figure 1.2. It can be noted that the shallow traps move along with the intrinsic band as the crystalline size decreases. However, the shift of the deep traps lying close to the middle of the forbidden gap is negligible. Thus, the transition involving the deep traps should not change in their energy with decreasing or increasing crystalline sizes.

Nanocrystals of II-VI semiconductor compounds such as ZnS, CdS, CdSe, CdTe and IV-VI semiconductor such as PbS, PbSe, SnSe, SnS are the current topics of research over the last decades. Nanometer sized semiconductor particles of these compounds are currently being investigated in many laboratories over the world. During the past years, the investigations are focused on linear and nonlinear optical properties, unusual fluorescence behavior, electron transfer reactions and the structural characterization of such particles [l.5-1.10]. It is established that in many cases it is the surface of the particles rather than the particle size which determines these properties, a result which is easily understood if one keeps in mind that the number of surface atoms is comparable to the number of bulk atoms in these particles. It is, therefore, a major goal to characterize the surface states and to control them chemically.

1.1.2 II-VI Semiconductors

In II-VI compound semiconductors, CdS and ZnS are the prime attention of current researchers due to following properties: (a) direct band gap, (b) high absorption coefficient, (c) good conversion efficiency, (d) high thermal stability and (e) easy to syntheses. Due to the wide band gap CdS (2.41 eV) and ZnS (3.61 eV) are used as a window layer as well as n-type semiconducting material in heterojunction solar cells [1.11].

CdS has long been recognized to be the best promising window or buffer layer for thin film heterojunction solar cells and the highest conversion efficiencies have been achieved with chemical bath deposited CdS as buffer layer in CIGS, CdTe-based solar cells [1.12, 1.13]. CdS has hexagonal closed packed structure with lattice constants $a = b \neq c$, $\alpha = \beta = 90°$, $\gamma = 120°$). In the year 1956, Balkanski and Broser [1.14] have first reported the neutral energy transport in CdS using photo-diffusion techniques. Martil *et al*. [1.15] have studied the temperature dependence electrical transport properties of polycrystalline rf sputtered CdS thin films. The room temperature values of analyzed samples for resistivities and Hall mobilities range between 1-10^8 Ω cm and 2-8 cm^2/Vs. Recently; there has been growing interest in

nanomaterials with specific shapes owing to the expectation of novel properties. In the year 1998, Yu *et al.* [1.16] have reported a solvothermal synthetic route to the II-VI semiconductors of CdE (E=S, Se, Te) by a reaction of CdC_2O_4 with E in the temperature range of 120-180 °C in an autoclave. They have found that the morphology of the CdE semiconductors can be controlled by choosing different solvents. CdS crystallites synthesized in ethylenediamine (*en*) are uniform nanorods with diameters of 20-50 nm and lengths of 200-1300 nm. Absorption spectra are observed at 485 nm whereas photoluminescence spectra are observed a narrow band at 420-500 nm for CdS nanorods powder samples at room temperature. Li *et al*. [1.17] have reported the solvothermal reaction of sulfur, selenium, or tellurium with cadmium metal powder in different organic solvents in the temperature range 120-200 °C and investigated systematically to prepare cadmium chalcogenides, CdE (E=S, Se, Te). The results show that the character of the products, such as crystal size, shape, and structure, are strongly influenced by the solvent and temperature during the solvothermal process. One-dimensional nanorods of CdE, with 10-40 nm diameters and several micrometers in length, are obtained by choosing coordinating solvents such as ethylenediamine and 1, 6-diaminohexane as the reaction solvent. The CdS nanorods produce a Raman spectrum with two clearly discernible LO modes. The absorption band yielded an onset near 520 nm and absorption peak at 480 nm, which is the characteristic absorption band of CdS [1.17]. The PL spectrum shows an intense, sharp PL peak at 467 nm with two shoulder peaks at 452 and 518 nm. Yang *et al*. [1.18] have reported the formation process of CdS nanorods prepared by the reaction of thiourea and cadmium nitrate in ethylenediamine. As-synthesized CdS nanorods powder sample is investigated in detail by X-ray powder diffraction, transmission electron microscopy, selected-area electron diffraction, and IR techniques. The obtained CdS single-crystal nanorods show an abnormal electron diffraction that is explained by the double diffraction of the incident electron inside the sample. The result from electron diffraction confirmed that CdS nanorods grow along *c* axis.

Though CdS has important optoelectronic properties and are being used in various device applications, the toxic waste discharged by the use of CdS and its impact on environment have motivated researchers in photovoltaic technology to explore new buffer layers that are environmentally benign with better physical properties than CdS [1.19, 1.20]. Among the possible alternative buffer layers, ZnS is the most promising one. The advantages of ZnS over CdS are (i) non-toxic and environmentally safe to handle than CdS, (ii) wider energy band gap than CdS, which transmits even higher energy photons and increases the

light absorption in the absorber layer and (iii) provides better lattice matching with absorbers having energy band gaps in the range of 1.3–1.5 eV.

ZnS has zinc-blende crystal structure consists of an fcc lattice (i.e. $a = b = c$, $\alpha = \beta = \gamma = 90°$). Besides being used as window material for solar cells [1.21], ZnS also finds applications in fabrication of light emitting diodes [1.22], cathode ray tubes [1.23] and thin film electroluminescence [1.24]. Apart from above, there also have some attractions in the new mechano-optic applications, because ZnS doped with some metal cations is a promising material to emit intense light upon stress, a phenomenon known as triboluminescence [1.25]. One-dimensional (1D) ZnS nanomaterials, such as nanorods [1.26], nanowires [1.27], nanotubes [1.28] and nanoribbons [1.29] have attracted considerable attention in recent years due to their potential applications in optoelectronics, magnetics, optics, etc. [1.30]. Wu *et al*. [1.31] have adopted a micelle template assisted method to synthesize ZnS nanowires with diameters 40–80 nm and lengths up to tens of micron. The formation of ZnS nanowires probably is via the process of the directional aggregation and orientated growth of the ZnS nanoparticles. Wang *et al*. [1.32] have synthesized pure and uniform hexagonal-phase ZnS nanorods with length up to several nanometer and diameter of 20–25 nm with quantum confinement effect by solvothermal method. The nanorods are single crystals in nature and are very uniform along the entire length. PL peak is observed at 425 nm (with 323 nm of excitation wavelength), attributed to the electron–hole recombination from internal vacancies for Zn and S atoms. It is observed that there is a prominent blue shift of around 45 nm of the emission band compared with that of the bulk ZnS [1.33], which might be due to the quantum size effects of the ZnS nanorods. The absorption peak is noticed at 295 nm. Compared with the bulk ZnS (344 nm), the absorption peak for the nanorods is of blue shift. This further suggested that these nanorods have obvious quantum confinement effect [1.34, 1.35]. Panda *et al*. [1.36] have synthesized ZnS nanoparticles of diameters of 3–4 nm which are self-assembled to form dense nanospheres of sizes ~100 nm by a colloidal precipitation method using PVP as the stabilizing agent. Studies indicate that the ZnS nanoparticles maintained their individual properties inside the nanospheres. Optical absorption spectra of the samples demonstrate the effect of quantum confinement in the ZnS nanocrystals. Room temperature photoluminescence measurements show a sharp UV emission at ~370 nm, attributed to sulfur vacancies. Raman spectra of bulk cubic phase of ZnS show the TO and LO zone center phonons at 276 and 351 cm^{-1}, respectively, and for Wurtzite type ZnS the E2 modes at 72 and 286 cm^{-1} [1.37]. The Raman peak observes at 344 cm^{-1} can be assigned as the LO mode of cubic ZnS and that observed at 257 cm^{-1} can be attributed to the LO phonon–plasmon

coupled modes [1.38, 1.39]. Compared to the Raman spectra of bulk cubic ZnS, the first order LO phonon peak of ZnS samples in the present study is shifted to lower frequency and the peak is broadened, which may be attributed to phonon confinement effect [1.40].

1.1.3 IV-VI Semiconductors

During the last decade, a variety of binary semiconductors especially IV–VI groups of periodic table have been studied due to their small energy gap. The IV–VI semiconductors have been found to be quite useful in optoelectronic devices working in far IR region as thermoelectric transducers and solar cells. This group consists of direct as well as indirect semiconductors. The unique feature of the direct energy gap in these compounds is that it increases with increasing temperature and decreases with hydrostatic pressure [1.41]. Among the IV-VI compound Sn(S, Se, Te) and Pb(S, Se, Te) are widely used.

Tin monosulphide (SnS) has been found to be one of the promising IV-VI compound semiconductor materials due to their important properties and potential application in optoelectronic devices. SnS is first reported by the German mineralogist Herzenberg in 1932 [1.42]. SnS adopts a strongly distorted NaCl structure and each tin atom is coordinated by six sulfurs in a highly distorted octahedral geometry [1.43]. The crystal is made up of orthorhombic unit cells [with lattice constants $a \neq b \neq c$, $\alpha = \beta = \gamma = 90°$] composing of double layers of tightly bound Sn–S atoms with the bonding between layers of the van der Waals type [1.44]. SnS usually exhibits p-type conduction and the acceptor levels are created by double-ionized tin vacancies. An excess of tin changes the type of conductivity of SnS from p-to n-type [1.45]. SnS is reported to have a direct band gap of about 1.3-1.5 eV and an indirect band gap of 1-1.3 eV [1.46, 1.47] depending on the condition of preparation. This suggests that SnS has appropriate electrical and optical features to make various kinds of optoelectronics devices. Additionally, its constituent elements Sn and S are being abundant in nature and not posing any health and environmental hazards. It's narrow band gap (1.3 eV) is ideal for photoelectric energy conversion. Therefore, SnS can be potentially used as a p-type material in thin film solar cells [1.48-1.51] and as an electrode in lithium ion batteries [1.52, 1.53]. Up to now, various methods have been developed for the synthesis of nanoscale SnS with different size and shape. George *et al*. [1.54] have reported that SnS nanoparticles can be prepared by thermal decomposition of organotin sulfur-containing precursors $R_4Sn_4S_6$ [R = Me, Bu^n and Ph] in air. Schlecht and Kienle [1.55] have presented a one-pot synthesis of unprotected SnS nanoparticles through an activated tin metal and element sulfur in

diethyleneglycoldimethylether (diglyme) at 160 °C, in which all manipulations are carried out under dry and oxygen-free argon conditions. An average of 20x40 nm size SnS nanoparticles are obtained by this reaction process. Qian and co-workers [1.56] have prepared SnS nanocrystallites with different morphologies through hydrothermal or solvothermal routes, where the solvents may be deionized water, ethanol, benzene, ethylenediamine, polyol, 8-hydroxyquinoline and others. SnS nanocrystals are also studied by Raman and XPS spectroscopy, which suggest that as-prepared SnS are pure crystalline in nature. Tang and co-workers have described SnS and SnS_2 nanoflakes by a reflux-assisted polyol route [1.57] and a microwave-assisted polyol synthetic method [1.58], respectively.

As an important IV-VI group semiconductor, Lead sulfide (PbS) has also attracted considerable attention owing to its especially small direct band gap (0.41 eV at 300 K) and a larger excitation Bohr radius of 18 nm [1.59], and has been widely used in many fields such as Pb^{2+} ion-selective sensors [1.60], photography [1.61], IR detector [1.62], and solar absorber [1.63]. Recently, PbS nanocrystals have attracted enormous attention of the current researchers due to (a) strong quantum confinement arising from the large exciton Bohr radius; (b) size-tunable optical band gap (E_g) covering wide spectral range from near infrared to visible, originated from their small E_g in bulk and (c) flexibility and versatility associated with their synthesis process [1.64]. These unique features have accounted for extensive studies in PbS, PbSe and PbTe based optoelectronic applications. Zhou *et al.* [1.65] have prepared well-defined single-crystalline PbS nano- and microstructures including dendrites, multipods, truncated nanocubes and nanocubes by a simple solution route. Reactions are done for 12 h at 100 °C in the presence of cetyltrimethylammonium bromine (CTAB) surfactant. They have shown that the shape of the PbS nanostructures depend on the molar ratio of the precursors. They have also investigated the photoluminescence properties and observed that PbS nano- and microstructures displayed a very strong luminescence around 632 nm at room temperature with the excitation wavelength of 495 nm. Xiong *et al.* [1.66] have described a facile L-cysteine-assisted solvothermal method in a mixed solution made of ethylenediamine (en) and distilled water for the large-scale synthesis of various PbS 1D and 3D novel nanostructures. Reactions are done at different temperature ranging from 100-200 °C for 48 h. They observed that Raman spectrum of the PbS dendritic nanostructure has six bands located at around 90, 140, 178, 441, 603, and 969 cm^{-1}. They have also observed a sharp and strong emission peak centered at 433 nm with the excitation wavelength of 360 nm. Emission bands at 433 nm are usually related to the transition of electrons from the conduction band edge to holes, trapped at interstitial Pb^{2+} sites. Ye *et al.* [1.67] have synthesized in situ self-

assembly one-dimensional PbS nanocrystals via hydrothermal route using $Pb(NO_3)_2$ and thiourea as starting materials. The reaction temperature is maintained at 150 °C for 3 h. The 1D materials are nearly 85 nm in breadth and 1.5 μm in length. They have also observed two sharp emission peaks centered at 332.6 and 373.5 nm of PbS nanoparticles solution prepared in ethanol. The most important physical parameters of CdS, ZnS, SnS and PbS are summarized in Appendix I.

1.2 Organic Semiconductors

Over the last decades a significant amount of research activity has focused on semi-conducting conjugated polymers and their derivatives because of their potential optoelectronic device applications, combined with attractive material properties such as low weight and ease of processing [1.68]. Compared with inorganic materials, a great advantage of organic materials is their variety. In inorganic materials, repeating units consist either of the same atoms or a few different atoms at the most, so there is not much room to control one property of the material while keeping the rest unchanged. In organic molecules, there are an almost infinite number of combinations of atoms and therefore it is possible to design organic materials to have desirable properties. In addition, the molecular arrangement and its dimensionality can be also controlled. Conducting polymer is first discovered by Alan J. Heeger, Alan MacDiarmid and Hideki Shirakawa in 1977 [1.69]. The Nobel Prize in Chemistry is awarded to them in the year 2000 in recognition to this work on conjugated and conducting polymers, specifically recognizing that polyacetelyne could be made conducting. In 1990, Burroughes *et al.* [1.70] have shown that by applying a voltage through a thin film of an undoped conjugated polymer, light emission (electro-luminescence) could be induced. This discovery made it possible to produce polymer light emitting diodes (PLEDs) and today, the focus has shifted from doped, electrically conducting conjugated polymers to undoped, semiconducting ones. Light emitting diodes and color displays with conjugated polymers as active materials have started to gain commercial foothold and several other applications such as lasers [1.71], transistors [1.72] and solar cells [1.73] are being developed rapidly. Today, the main focus in the field is on aromatic polymers such as; poly(p-phenylenevinylene) (PPV) [1.74], poly(para-phenylene) (PPP) [1.75], polyfluorene (PF) [1.76], polyaniline (PA) [1.77], and polythiophene (PT) [1.78]. These types of polymers are relatively stable and many of their features can be tuned by the incorporation of different substituents.

Synthesis of PPP is first studied by Speight *et al*. [1.79] and by Noren and Stille [1.80] in 1971. In 1979, high conductivity of PPP is observed upon doping. [1.81]. Poly (para-phenylene) (PPP) has some important advantages than other conducting polymers. These are as follows [1.75, 1.82]: a) PPP is simplest rigid-rod like polymer composed of the phenylene rings connected between para (1, 4) positions. The simple structure has attracted lot of interest, b) It has high tensile strength, high compressive strength, high thermal stability, c) It shows high electric conductivity by doping, d) It has very wide conductivity range (from 10^{-18} S/cm in the pristine form to more than 10^{2} S/cm in the doped state), e) High quantum yield in electroluminescence (EL) and f) PPP has been reported to show blue luminescence. According to literature, PPP is studied as a thermally resistant polymer but now has applications also in various photo electronic devices. The use of PPP in different applications has been limited by the insolubility of pure PPP, which chemically synthesized, usually is obtained in powder form. Thus films of PPP and its derivatives have mainly been obtained by vacuum evaporation of pure oligomers. For PPP to be utilized in devices and advanced materials it should have a high relative molecular mass, homogeneous structure and good molecular packing.

In recent years, other polymers like polyfluorenes and their derivatives have also emerged as an attractive class of materials for device applications such as LEDs [1.83] and solid-state lasers [1.84, 1.85] due to their efficient electroluminescence (EL) and photoluminescence (PL), good charge-transport properties, and thermal stability [1.86]. These materials display extremely high photoluminescence (PL) efficiencies both in solution and in solid films, with emission wavelengths potentially over the whole visible spectral region [1.87–1.90]. These polymers are stable above their melting points, permitting melt processing which is not possible for many conjugated polymers. The optical and electrical properties of polyfluorene have also been modified through copolymerization of fluorine monomers with other molecular subunits [1.88]. Their photostability and thermal stability are also found to be better than those of PPVs [1.91, 1.92]. In addition, these polymers show different film morphologies upon thermal or solvent vapor treatment, which have interesting photophysical properties [1.93, 1.94]. In particular, poly(9,9-dioctylfluorene) (PFO) films show a liquid crystalline (LC) state at ~170 °C, and by slowly cooling the sample to room temperature one can obtain a crystalline film where the periodicity is governed by the alkyl side chain length [1.95, 1.96]. These phenomena enrich the device physics with additional properties such as increased carrier mobility, polarized EL, laser action at reduced excitation intensities, and spectral narrowing at different wavelengths. It has also been shown that

modifications of the side chains strongly influence the solid-state packing of the polymer and also the optical emission of the electroluminescent polymers [1.97, 1.98].

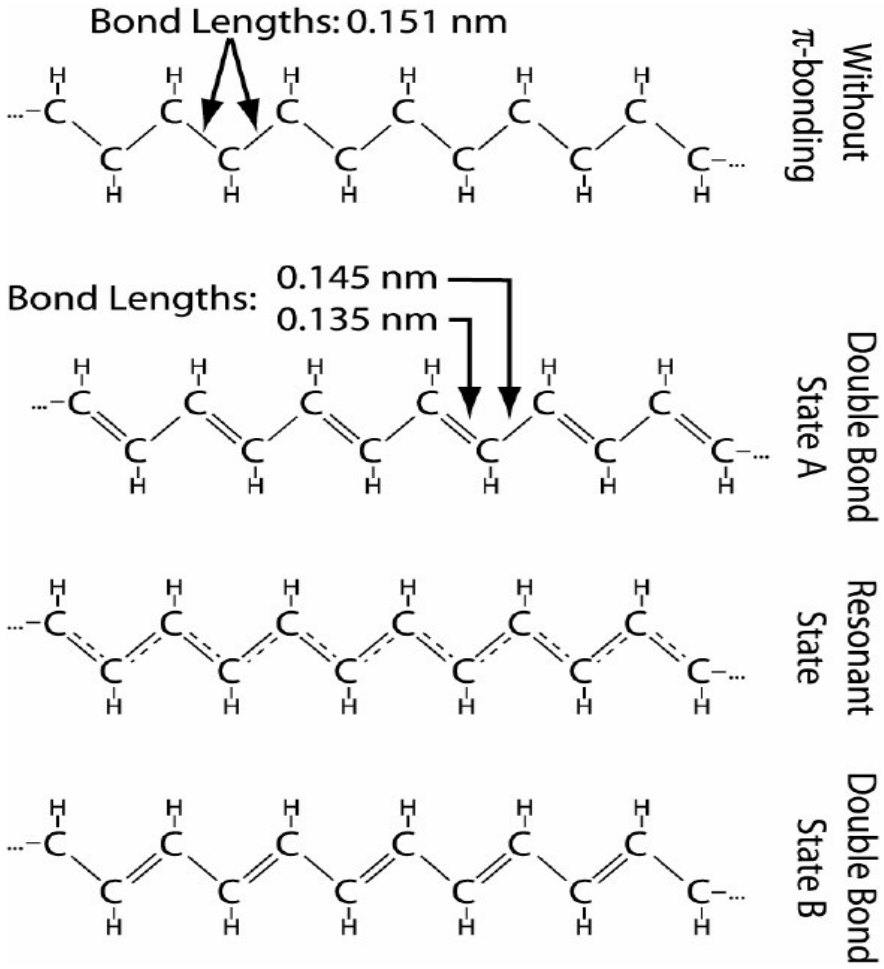

Figure 1.3: A schematic diagram of the simplest fully-conjugated polymer molecule, transpolyacetylene. Three possible configurations are shown for this molecule. In addition, the structure of the molecule in the absence of π-bonding is shown at the top, giving a comparison of bond lengths [1.99].

1.2.1 Structural Properties of Conjugated Polymers

The basic structure of a conducting or semiconducting organic material is shown in Figure 1.3. The essential feature is a continuous series of double bonds that runs the length of the molecule. Molecules with this structure are known as "*conjugated*". Each C atom in the backbone has one bond to each of its neighbors and one bond forming the double-bonded backbone. Because each C atom supplies one bond to this double bonding structure, one of the two adjacent bonds, on average, is a double bond, while the other is a single bond. It does

not matter, in principle, which is the double bond and which the single bond. Another way to look at the situation is that each C atom has a half-filled p state available for π bonding, thus the double bonds can be represented as a π -bonded molecular orbital running down the length of the carbon backbone. Each C atom also has one bond left over for attachment of functional groups, usually a H atom. This opportunity to add functional groups makes conjugated polymers highly adjustable. The most important feature of π-conjugated polymers is that unsaturated carbons lie on a chain, over which π electrons are delocalized one-dimensionally. The side chains provide the thermal stability, solubility, hydrophilicity, and many other properties to the polymer backbones, but the fundamental optical (and electrical) properties are determined by the π electrons.

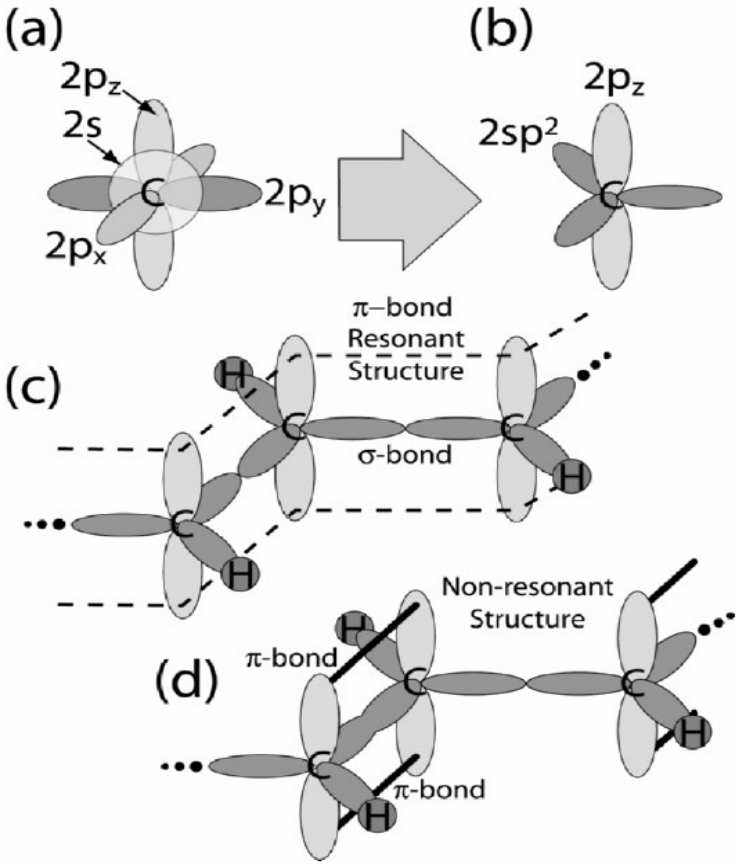

Figure 1.4: A schematic of the hybridization and bonding in poly-ene structures. (a) shows the valence atomic orbitals of C, (b) the hybrid molecular orbitals in poly-enes, (c) the resonant backbone structure of a poly-ene, and (d) the structure resulting from the choice of one of the two possible double bonding structures [1.99].

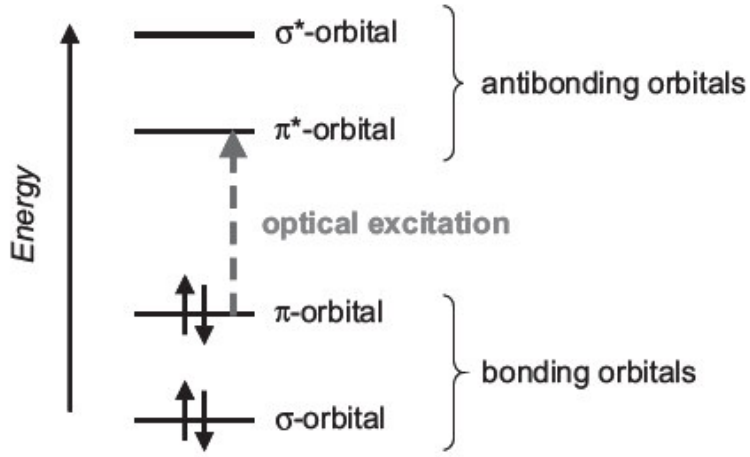

Figure 1.5: The energy levels of a p-conjugated molecule. The lowest electronic excitation is between the bonding π-orbital and the antibonding π*-orbital [1.100].

The carbon atom bonding is hybridized with $s+p_x+p_y$ atomic orbitals (Figure 1.4(b)) forming the sp^2 triangular planar molecular orbital structure and leaving a lone unhybridized p_z orbital projecting along the orthogonal z-axis. The sp^2 hybrid orbitals form conventional σ bonds (Figure 1.4(c)). (The bond axis lies along the bond direction in a σ bond.) These bonds have fully paired electrons in their bonding states and empty antibonding states, resulting in a very strong and stable covalently-bonded molecular backbone. The unhybridized, half-filled p_z orbitals form the π bonds (Figure 1.4(c) and (d)). In π bonds the bond axis is perpendicular to the σ bonds direction. Figure 1.5 shows the bonding and antibonding orbitals of the organic polymers.

1.2.2 Optical Properties of Conjugated Polymers

Organic materials have fascinating optical properties and have been extensively investigated in many research fields associated with light. Organic materials have received considerable research attention as model systems for understanding the interaction between light and materials because their molecular arrangement and dimensionality can be controlled as per wish. From the application viewpoint for fabricating light emitting devices and nonlinear optical devices, π-conjugated polymers are the most promising materials because of their good fluorescence yield, large optical nonlinearity, and ultrafast class relaxation time.

a) Absorption Studies

Absorption measurement is the most fundamental spectroscopy and is very helpful in understanding the characteristic features of π-conjugated polymers, including large electron–phonon interaction. In spin-coated films, the polymer forms an amorphous phase, and the broad width of the band results from significant inhomogeneous broadening. In π-conjugated polymers, ideally π electrons are delocalized over the whole polymer chain but structural disorders, such as bending or twisting around a bond between fluorene units, limit the delocalization of π electrons and increases the resonance energy of the polymer. Since actual polymers have a large distribution of delocalization lengths of π electrons, especially in amorphous films and in solution, a broad and featureless absorption spectrum [Figure 1.6(a)] is often observed.

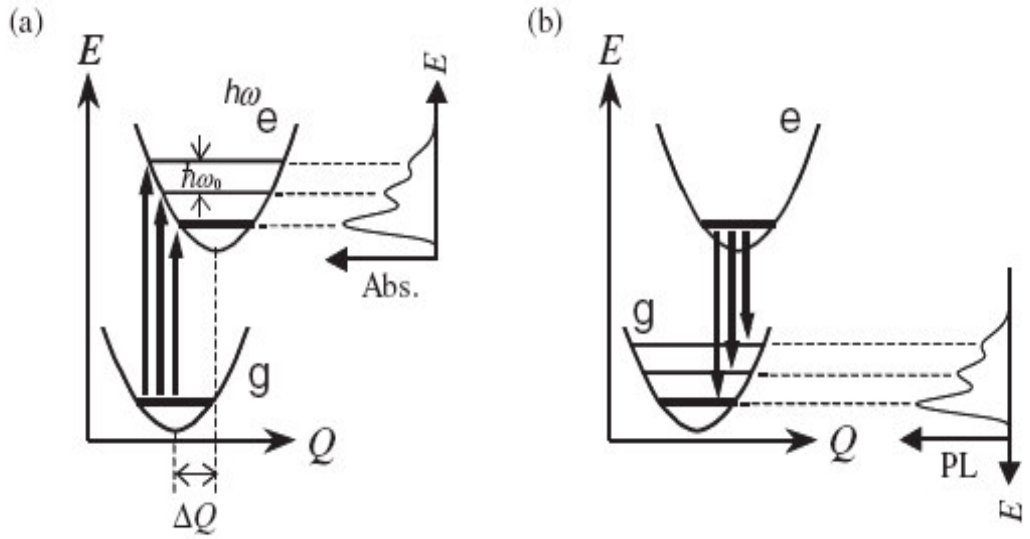

Figure 1.6: Schematic illustration of vibronic potential-energy curves for (a) absorption and (b) photoluminescence (PL) processes. In this Figure, e and g indicate electronic excited and ground states. $\hbar\omega_0$ is the phonon energy of the associated mode, and ΔQ is the difference between the potential minima of the g and e curves. If ΔQ is zero, i.e. the case of no electron–phonon interaction, the transitions to the higher vibrational levels are forbidden [1.101].

Some π-conjugated polymers have a tendency to align in a regular manner and to form ordered films, where structural disorders are much suppressed. This system has electron–phonon interaction, transitions from the zero vibrational level in the ground state to the excited vibrational levels in the excited state are allowed, and discrete transition bands

appear in the absorption spectrum. In Figure 1.6, the potential minimum of the excited state is slightly shifted from that of the ground state. The magnitude of this shift, ΔQ, represents the strength of electron–phonon interaction in the system. The transition to the zero vibrational level in the excited state is called '0–0 transition' and corresponds to purely an electronic transition. On the other hand, other transitions are called '0–1 transition', '0–2 transition', etc. After a photoexcitation corresponding to a 0–*n* transition, an electronic excited state is created and *n* phonons are emitted. In many π-conjugated polymers the associated phonon mode is a C=C stretching mode with phonon energy of 0.18 eV. Such a vibronic structure is always observed in their ordered films. Although π-conjugated polymers have many phonon modes, most of their phonon energies are much less than 0.18 eV and hence their contributions can be included in inhomogeneous broadening.

b) Photoluminescence Studies

Many π-conjugated polymers show photoluminescence (PL) in the visible spectral range. For instance, polyfluorene, poly(*p*-phenylenevinylene) (PPV), and polythiophene show blue, green, and red emissions, respectively. Some of their derivatives have good fluorescence efficiency and are expected to be used in fabricating light-emitting devices. In these materials, after excited states are created by photoexcitation, these immediately relax into the lowest excited state (Kasha's rule) and then emit light. Therefore, their PL straightforwardly reflects the nature of the lowest excited state. In the PL spectrum, vibronic structure also appears due to transitions from the lowest vibrational level in the excited state to vibrational levels in the ground state [Figure 1.6(b)]. The difference between the absorption and PL maxima is called the *Stokes shift*, which results from many relaxation mechanisms of the polymer chain occurring after the photoexcitation.

1.2.3 Electrical Transport of Conjugated Polymers

In the electronic structure of π-conjugated polymers, the linked π orbitals form the π band. Each orbital has two states, i.e. spin-up and -down states, but supplies only one electron. Thus, one may expect that the π band is a half-filled band and therefore π-conjugated polymers should show efficient conductivity like metals. However, in the actual polymers, intervals between carbon atoms are alternately modified to form bond alternation in order to reduce the total energy (see Figure 1.7). This alternation splits the π band into two

equal half bands, separated by a band gap; the lower half is fully filled and the upper one is completely empty. Although this bond alternation increases the elastic energy, the energy of electrons is lowered enough to compensate for the increase. Consequently, π-conjugated polymers show the electronic properties of semiconductors or insulators. It may be noted that, in the polymer backbone, purely single bonds do not appear although the bond alternation is depicted using a single line as well as a double line. The interatomic distances between carbon atoms are modified only slightly by the alternation. Several electron diffraction measurements have revealed that the bond lengths are modified by less than 5% from the mean length. Therefore, it is reasonable to consider that π electrons are delocalized over the whole polymer backbone.

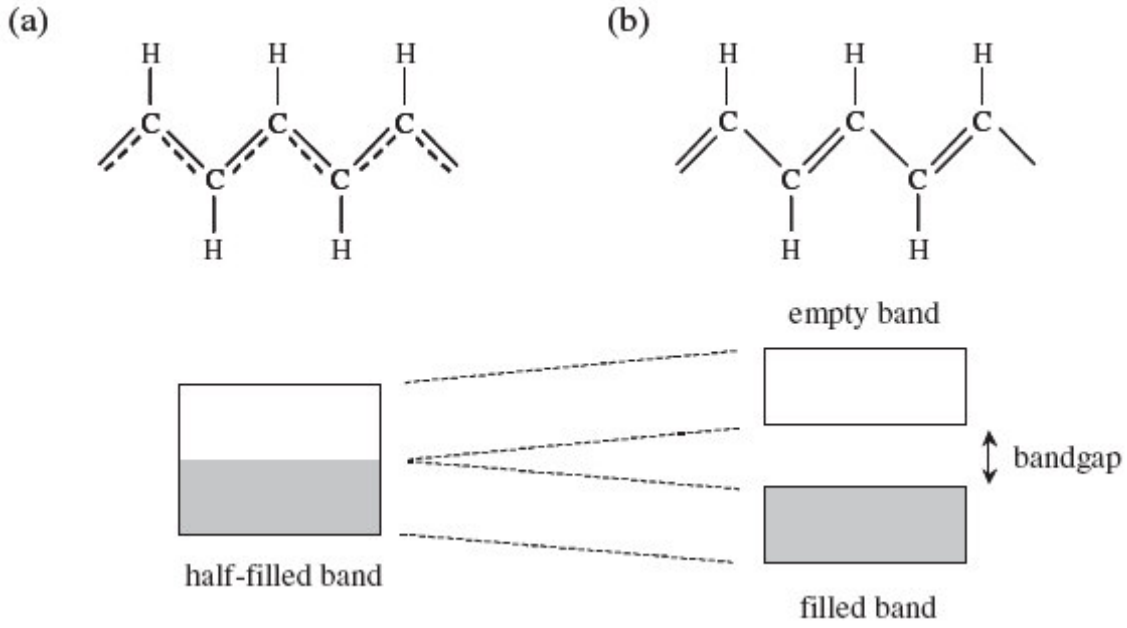

Figure 1.7: (a) In the case where carbon atoms are placed with the same intervals, the linked π orbitals form a half-filled band. In the above chemical structure, the solid lines are the σ bonds and dashed lines indicate the linked π orbitals. (The dotted lines are not π bonds because each carbon atom has only 4 bonding orbitals.) (b) In the case where the intervals between carbon atoms are alternately modulated, the half-filled band splits into a filled band and an empty band separated by a band gap [1.101].

1.2.4 Hybrid Organic Semiconductors

Basically most of the conjugated polymers behave like insulators. Conjugated polymers are made conductive generally by doping. The doped polymers often have limitations like poor stability of physical and chemical properties at different environments.

Poly (para-phenylene) (PPP) is different from most of conductive polymers due to its high thermal stability and resistance to oxidation and chemical degradation. These conjugated polymers can then be used for encapsulation of nanomaterials to form hybrid polymers. Since nanoparticles have high surface to volume ratio and are then very sensitive to their environments, their encapsulation with polymers results in the reduction of nonradiative contribution of surface states and enhances consequently the quantum efficiency. Doped II-VI (CdS, ZnS) and IV-VI (SnS, PbS) nanocrystals in conjugated polymers seems to be interesting to enhance the electroluminescence and electrical conducting properties of these materials.

1.3 Heterojunction Solar Cells

A *heterojunction* is a junction formed between two dissimilar semiconductors. For semiconductor-device applications, the difference in energy gap provides another degree of freedom that produces many interesting phenomena. The successful applications of heterojunctions in various devices are due to the capability to grow lattice-matched semiconductor materials on top of one another with virtually no interface traps. Heterojunctions between two different semiconductors have been extensively studied for various combinations of semiconductors. Their possible application ranges from photovoltaic cells to light emitting diodes. In general, heterostructures offer a wide range of design choices for novel semiconductor devices (e.g., diodes, transistors, and optoelectronic devices). The main advantages are related to the control of the charge carrier transport by controlling the energy barriers and potential variations (on a quantum level) and to the ability of heterostructures to confine the optical radiation (which is especially essential in optoelectronic devices). In many applications, devices incorporate more than one heterojunction, and in such cases these are referred to as a *heterostructure.* In an ideal heterojunction, the interface is atomically abrupt.

Photovoltaic effect in CdS based solar cell is first reported by Reynolds *et al*. [1.102] for a junction formed by an evaporated film of copper. Later investigation [1.103] reveals that the junction is actually one between CdS and Cu_2S. A great deal of effort has been expended to develop this photovoltaic junction and, although some variation exists, cells have generally been made by reacting CdS film prepared by physical vapor deposition with a cuprous ion solution. During the 1960s and early 1970s many cell designs have achieved performances of over 5% and some up to 9% [1.104, 1.105]. Photovoltaic effects of CdS-PbS heterojunction

are measured by Watanabe *et al*. [1.106] for visible and near-IR regions. It is shown that the heterojunctions have marked photovoltaic response at near-IR region. The response presents particular interest in possible application to infrared detector in such field as optical readers in electronic computers. Photovoltaic effects of p-CdTe/n-CdS [1.107, 1.108], p-SnS/n-CdS [1.50, 1.51, 1.109, 1.110], p-Culn($S_{0.5}Se_{0.5}$)$_2$/n-CdZnS:In [1.111] are also observed by various groups. Till date 16% efficiency has been recorded in case of CdS/CdTe based solar cells [1.108]. In case of CdS/SnS based solar cells, maximum 1.3% efficiency has been reported by Reddy *et al.* [1.50]. Schematic diagram of two different kind of heterojunction solar cells are given in Figure 1.8.

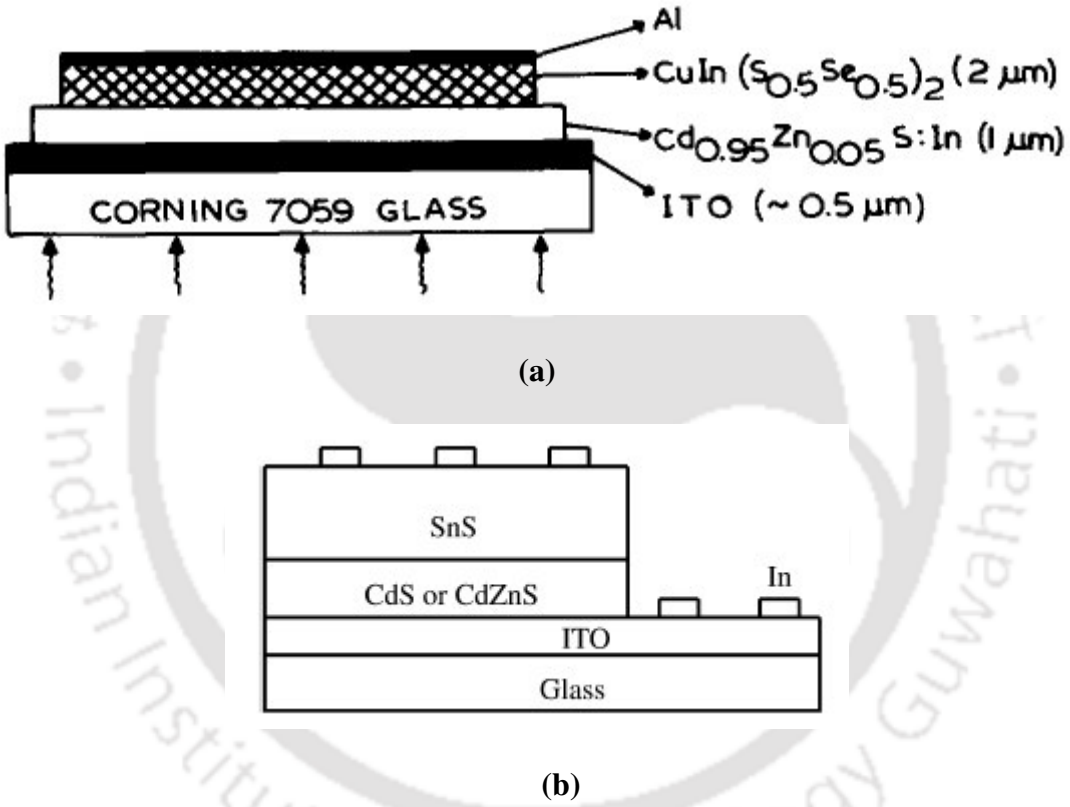

Figure 1.8: Schematic representation of the heterojunction solar cells structure: (a) p-Culn($S_{0.5}Se_{0.5}$)$_2$/n-CdZnS:In based solar cell (Image taken from Ref [1.111]) and (b) CdS or CdZnS/SnS based solar cells (Image taken from Ref [1.112])

1.4 Motivation of the Present Thesis Work

Nanocrystalline semiconductor structures like nanorods, nanotubes, nanobelts, nanowires and nanoparticles and semiconducting conjugated polymers have been an area of great research interest over the last decade. Due to the quantum size effect, the physical and

chemical properties of these nanomaterials are very different from their bulk counterparts. These materials find interesting applications as sensors and devices due to high surface to volume ratio. Among these, nanocrystals of II–VI and IV–VI group semiconductor compounds have attracted lot of interest due to their important optoelectronic properties. Whereas, semiconducting polymers usually have conjugated backbones that allow electrons to delocalize along the main chain. Many conjugated polymers are colored and show useful photophysical properties, such as photoconductivity, nonlinear optical properties, and electroluminescence. Since the discovery of electroluminescence (EL) from conjugated polymers in 1990, polymer light emitting diodes (PLEDs) have been considered promising candidates for the next generation of displays. PLEDs have attracted significant attention due to their ease of processing, good mechanical properties, and large area applications. PLEDs using blends of polymers have been extensively studied because they can synergistically combine certain features of the component polymers and thus show novel properties. By blending polymers, one can improve the overall device performance of LEDs and tune their emission color. Optical and electrical properties of the conjugated polymers can be enhanced by incorporation of semiconducting nanostructured materials.

Motivated by various optoelectronics properties of the II-VI, IV-VI and hybrid polymers, the present thesis deals with the structural, optical, thermal and electrical transport properties on CdS, ZnS, SnS and PbS nanostructured materials prepared by solvothermal process and PPP and PF conjugated polymers prepared by oxidative polymerization process and Suzuki coupling respectively and their blends with nanomaterials. Heterojunction solar cells based on p-SnS/n-CdS nanostructures have been prepared and studied for their different physical parameters. The important results obtained as a part of these studies are mentioned below.

As-synthesized CdS powder samples consist of nanorods and the typical diameter varying from 10-50 nm and length varying from 80-750 nm. In optical absorbance spectra, a peak is observed at 488 nm which is basically due to the band to band absorption of the CdS nanorods. CdS nanorods thin films also show a sharp emission peak at 520 nm. The Raman spectra consist of a single fundamental band at approximately 312 cm^{-1} for all the samples in powder form and can be assigned to the longitudinal optical phonon (LO) mode. Thermal stability studies on these as-synthesized powder samples have shown that CdS nanorods are stable up to 650 °C. The films show a good photosensitivity ($S= \sigma_L/ \sigma_d$) $\approx 10^5$ at 300 K (under ~ 10 mW/cm^2 light from halogen lamp), which is decreased to 5.76 at 453 K. CdS thin films have also shown persistent photocurrent (PPC). The observed PPC and its slow decay with

time in case of CdS nanostructured thin films have been explained by potential barrier fluctuation model.

ZnS powder samples consist of disc like nanoparticles with diameters varying from 50 nm to several micrometers and surface morphology and crystallinity of the ZnS powder samples are improved with reaction times. A broad emission peak is observed at 363 nm (3.42 eV) for all the samples along with two sharp peaks at 422 nm and 439 nm for excitation wavelength at 250 nm. The dark conductivity for these nanostructure thin films is of the same order as that of bulk samples. The thermal activation energy for the dark and photoconductivity is calculated as 1.68 eV and 1.5 eV respectively (the illumination intensity for 10 mW/cm^2).

SnS powder samples consist of nanoflakes with thickness varying from 50-80 nm and length varying from 200 nm to several micrometers. From TGA curves it is observed that as-synthesized SnS powder samples are stable up to 620 °C. The dark conductivity of the SnS thin films show thermally activated behavior in the temperature range from room temperature to 463 K. The activation energy from the slope of the ln σ vs 1000/T is found to be nearly 0.48 eV.

The average particle size of the PbS nanocubes is found to vary from 25–300 nm with an increase in size with increasing reaction times. PbS nanocubes show good photoluminescence properties. The emission spectrum shows a broad peak at around 310 nm along with two relatively narrow peaks at 358 nm and 384 nm and a shoulder at around 430 nm for 250 and 300 nm of excitation wavelengths. The Raman spectra of the as-prepared PbS powder sample indicates seven bands in the range of 50-1100 cm^{-1}, located at around 90, 140, 180, 310, 450, 620 and 976 cm^{-1}. The I-V characteristics of the PbS thin films using silver paste exhibits ohmic nature. The conductivity is nearly constant in the temperature range 300-450 K. This is due to its low band gap.

Both PPP and PF shows blue luminescence and are suitable for blue LEDs. In case of UV-Vis titration, a linear increase in absorption is observed with increase in CdS concentration. Although no shift in peak position has been observed. The thermal stability of PPP is enhanced by adding CdS nanoparticles. The virgin PPP films are found to be highly insulating ($\sigma \approx 10^{-13}\ \Omega^{-1}\ cm^{-1}$) near room temperature. When doped with CdS nanoparticles, conductivity is enhanced by several orders of magnitude near room temperature. The activation energy for polymer blend in the range 333 to 403 K is found to be 0.68 eV. Above 403 K, when conductivity is ~ $10^{-4}\ \Omega^{-1}\ cm^{-1}$, the activation energy is decreased to 0.08 eV. Structural and morphological properties of the PF and its nanostructured blends are studied

by XRD, TEM and SEM. The absorption peaks located in the range from 378 to 390 nm are due to π-π* transition of conjugated polyfluorene backbone. Onsets of absorption spectra of the PF incorporated with nanostructured materials is found to have shifted to 393 nm (corresponding band gap 3.16 eV) in dilute chloroform solution, whereas in thin film, absorption peaks are centered at 390 nm. In emission spectroscopy, two peaks are observed at 411 and 433 nm respectively for pure PF dilute chloroform solution for the excitation wavelength of 370 nm. In case of thin films, emission peaks are observed at 421 and 441 nm respectively. In comparison with dilute solutions, the emission spectra of polymers in film state are slightly red-shifted and can be attributed to the aggregation of polymer chains. For all the samples, I-V curves are straight lines passing through origin and suggest that evaporated Al forms an ohmic contact with polymer and its nanocomposites blends. Pure PF shows conductivity around 2.8×10^{-11} $\Omega^{-1}cm^{-1}$ at 300 K. After incorporation of nanostructured materials in PF matrix, the dark conductivity of their blends has increased slightly. No photoconductivity is observed in PF and its nanocomposites blends at room temperature under illumination of 10 mW/cm^2 of incident light.

p-SnS/n-CdS nanostructured based heterojunction solar cells are also prepared and their important physical parameters are obtained. Typical parameters for these solar cells under illumination of 100 mW/cm^2 are: Open circuit voltage (V_{OC}) = 100 mV, short circuit current (I_{sc}) = 240 μA, fill factor (FF) = 0.52, series resistance (R_s) = 166 Ω, shunt resistance (R_{sh}) = 2 kΩ and efficiency (η) of 0.32%. Spectral response curve indicates that around 75% of incident photons are absorbed in the wavelength range of 500-600 nm. It is observed that efficiency of the cells depends on the thickness of the CdS and SnS layers. As the thickness of SnS layers is increased efficiency increase. Efficiency of the solar cells can be improved by optimizing the different physical parameters like thickness of the window as well as absorber layer and reducing series resistance.

1.5 References

[1.1] Peter Y. Yu Manuel Cardona, *Fundamental of Semiconductors (Physics and Materials Properties)*, Springer, 2005.

[1.2] D. Bimberg, *Semiconductor Nanostructures*, Springer, 2008.

[1.3] N. Chestony, T. D. Harris, R. Hull and L. E. Brus, J. Chem. Phys. **90**, 3393 (1986).

[1.4] M. Mukherjee, A. Datta and D. Chakravorty, Appl. Phys. Lett. **64**, 28 (1994).

[1.5] A. Henglein, Pure Appl. Chem. **56**, 1215 (1984).

[1.6] L. E. Brus, IEEE J. Quantum Electr. **QE-22**, 1909 (1986).

[1.7] L. E. Brus, J. Phys. Chem. **86**, 2555 (1986).

[1.8] A. Henglein, Topics Current Chem. **143**, I 15 (1988).

[1.9] A. Henglein, Chem. Rev. **89**, 1861 (1989).

[1.10] Y. Wang and N. Herron, J. Phys. Chem. **95**, 525 (1991).

[1.11] S. S. Nair and M. A. Khadar, Sci. Technol. Adv. Mater. **9**, 035010 (2008).

[1.12] K. Ramanathan, M. Contreras, C. L. Perkin, S. Asher, F. S. Hasoon, J. Keane, D. Young, M. Romero, W. Metzger, R. Noufi, J. Ward and A. Duda, Prog. Photovolt. Res. Appl. **11**, 225 (2003).

[1.13] X. Wu, J. C. Keane, R. G. Dhere, C. Dehart, D. S. Albin, A. Duda, T. A. Gessert, S. Asher, D. H. Levi and P. Sheldon, in: Proceedings of the 17th European Photovoltaic Solar Energy Conference, Munich, Germany, 2001.

[1.14] M. Balkanski and I. Broser, Paper given at the International Conference on Semiconductors and Phosphors, Garmisch-Partenkirchen.

[1.15] I. Martil, G. Gonzalez-Diaz and F. Sanchez-Quesada, J. Vac. Sci. Technol. A **2**, 1491 (1984).

[1.16] S. H. Yu, Y. S. Wu, J. Yang, Z. H. Han, Y. Xie, Y. T. Qian and X. M. Liu, Chem. Mater. **10**, 2309 (1998).

[1.17] Y. Li, H. Liao, Y. Ding, Y. Fan, Y. Zhang and Y. Qian, Inorg. Chem. **38**, 1382 (1999).

[1.18] J. Yang, J. H. Zeng, S. H. Yu, L. Yang, G. Zhou and Y. Qian, Chem. Mater. **12**, 3259 (2000).

[1.19] M. Rusu, W. Eisele, R. Wiirz, A. Ennaoui, M. Ch. Lux-Steiner, T. P. Niesen and F. Karg, J. Phys. Chem. Solids **64**, 2037 (2003).

[1.20] G. Gordillo and E. Romero, Thin Solid Films **484**, 352 (2005).

[1.21] L. X. Shao, K. H. Chang and H. L. Hwang, Appl. Surf. Sci. **212-213**, 305 (2003).

[1.22] T. Yamamoto, S. Kishimoto and S. Iida, Phys. B **308–310**, 916 (2001).

[1.23] M. Bredol and J. Merikhi, J. Mater. Sci. **33**, 471 (1998).

[1.24] Y. Kavanagh, M. J. Alam and D. C. Cameron, Thin Solid Films **447-448**, 85 (2004).

[1.25] (a) A. J. Walton, Adv. Phys. **26**, 887 (1997); (b) O. Agyeman, C. N. Xu, M. Suzuki and X. G. Zhang, J. Mater. Res. **17**, 959 (2002); (c) C. N. Xu, T. Watanabe, M. Akiyama and X. G. Zhang, Appl. Phys. Lett. **74**, 1236 (1999).

[1.26] Q. T. Zhao, L. S. Hou and R. Huang, Inorg. Chem. Commun. **6**, 971 (2003).

[1.27] Y. Jiang, X. M. Meng, J. Liu, Z. R. Hong, C. S. Lee and S. T. Lee, Adv. Mater. **15**, 1195 (2003).

[1.28] R. T. Lv, C. B. Cao, Y. J. Guo and H. S. Zhu, J. Mater. Sci. **39**, 1575 (2004).

[1.29] Y. Jiang, X. M. Meng, J. Liu, Z. Y. Xie, C. S. Lee and S. T. Lee, Adv. Mater. **15**, 323 (2003).

[1.30] Z. Pan, Z. Dai and Z. Wang, Science **291**, 1947 (2001).

[1.31] Q. Wu, N. Zheng, Y. Ding and Y. Li, Inorg. Chem. Commun. **5**, 671 (2002).

[1.32] H. Wang, Z. Chen, Q. Cheng and L. Yuan, J. Alloys Compd. **478**, 872 (2009).

[1.33] P. Yang, M. K. Lü, F. Q. Meng, C. F. Song and D. Xu, Opt. Mater. **27**, 103 (2004).

[1.34] L. Brus, J. Phys. Chem. **90**, 2555 (1986).

[1.35] P. E. Lippens and M. Lannoo, Phys. Rev. B **39**, 10935 (1989).

[1.36] S. K. Panda, A. Datta and S. Chaudhuri, Chem. Phys. Lett. **440**, 235 (2007).

[1.37] O. Brafman and S. S. Mitra, Phys. Rev. **171**, 931 (1968).

[1.38] G. O. Smith, Phys. Rev. Lett. **68**, 2366 (1992).

[1.39] S. Kumar, M. Abdul Khadar, S. K. Dhara, T. R. Ravindran and K. G. M. Nair, Nucl. Instr. Meth. Phys. Res. B **251**, 435 (2006).

[1.40] A. Bruchhausen, A. Fainstein, B. Jusserand and R. Andre, Phys. Rev. B **73**, 85305 (2006).

[1.41] B. G. Yacobi, *Semiconductor Materials An Introduction to Basic Principles*, KLUWER ACADEMIC PUBLISHERS, pp. 147 (2003).

[1.42] R. Herzenberge, Rev. Miner. **4**, 33 (1932).

[1.43] T. Jiang and G. A. Ozin, J. Mater. Chem. **8**, 1099 (1998).

[1.44] A. Ghazali, Z. Zainal, M. Z. Hussein and A. Kassim, Sol. Energy Mater. Sol. Cells **55**, 237 (1998).

[1.45] M. Ristov, G. Sinadinovski, I. Grozdanov and M. Mitreski, Thin Solid Films **173**, 53 (1989).

[1.46] R. H. Bube, *Photoconductivity of Solids* (Wiley, New York) pp. 233, 1960.

[1.47] H. Zhu, D. Yang and H. Zhang, Mater. Lett. **60**, 2686 (2006).

[1.48] H. Noguchi, A. Setiyadi, H. Tanamura, T. Nagatomo and O. Omoto, Sol. Energy Mater. Sol. Cells **35**, 325 (1994).

[1.49] M. Ristov, G. Sinadinovski, M. Mitreski and M. Ristova, Sol. Energy Mater. Sol. Cells **69**, 17 (2001).

[1.50] K. T. R. Reddy, N. K. Reddy and R. W. Miles, Sol. Energy Mater. Sol. Cells **90**, 3041 (2006).

[1.51] B. Ghosh, M. Das, P. Banerjee and S. Das, Sol. Energy Mater. Sol. Cells **92**, 1099 (2008).

[1.52] X. L. Gou, J. Chen and P. W. Shen, Mater. Chem. Phys. **93**, 557 (2005).

[1.53] Y. Li, J. P. Tu, X. H. Huang, H. M. Wu and Y. F. Yuan, Electrochem. Commun. **9**, 49 (2007).

[1.54] A. A. George, C. S. Merces, C. B. Ana, M. Geraldo, M. L. Rochel and T. C. Maria, Phys. Chem. Chem. Phys. **2**, 5708 (2002).

[1.55] S. Schlecht and L. Kienle, Inorg. Chem. **40**, 5719 (2001).

[1.56] (a) H. L. Su, X. Yie, Y. J. Xiong, P. Gao and Y. T. Qian, J. Solid State Chem. **161**, 190 (2001); (b) L. Qing, Y. Ding, H. Wu, X. M. Liu and Y. T. Qian, Mater. Res. Bull. **37**, 925 (2002); (c) C. H. An, K. B. Tang, G. Z. Shen, C. R. Wang, Q. Yang, B. Hai and Y. T. Qian, J. Cryst. Growth **244**, 333 (2002); (d) C. K. An, B. Tang, Y. Jin, Q. C. Liu, X. Y. Chen and Y. T. Qian, J. Cryst. Growth **252**, 581 (2003); (e) H. M. Hu, B. J. Yang, J. H. Zeng and Y. T. Qian, Mater. Chem. Phys. **86**, 233 (2004).

[1.57] G. Z. Shen, D. Chen, K. B. Tang, L. Y. Huang, Y. T. Qian and G. E. Zhou, Inorg. Chem. Commun. **6**, 178 (2003).

[1.58] D. Chen, G. Z. Shen, K. B. Tang, S. J. Lei, H. G. Zheng and Y. T. Qian, J. Cryst. Growth **260**, 469 (2004).

[1.59] J. L. Machol, F. W. Wise, R. C. Patel and D. B. Tanner, Phys. Rev. B **48**, 2819 (1993).

[1.60] H. Hirata and K. Higashiyama, Bull. Chem. Soc. Jpn. **44**, 2420 (1971).

[1.61] P. K. Nair, O. Gomezdaza and M. T. S. Nair, Adv. Mater. Opt. Electron. **1**, 139 (1992).

[1.62] P. Gadenne, Y. Yagil and G. Deutscher, J. Appl. Phys. **66**, 3019 (1989).

[1.63] T. K. Chaudhuri and S. Chatterjes, Proc. Int. Conf. Thermoelectr. **11**, 40 (1992).

[1.64] J. Zhang and X. Jiang, Appl. Phys. Lett. **92**, 141108 (2008).

[1.65] G. Zhou, M. Lu, Z. Xiu, S. Wang, H. Zhang, Y. Zhou and S. Wang, J. Phys. Chem. B **110**, 6543 (2006).

[1.66] S. Xiong, B. Xi, D. Xu, C. Wang, X. Feng, H. Zhou, and Y. Qian, J. Phys. Chem. C **111**, 16761 (2007).

[1.67] S. Ye, Y. Ye, Y. Ni and Z. Wu, J. Cryst. Growth **284**, 172 (2005).

[1.68] F. P. Wenzl, G. Mauthner, M. Collon, E. J. W. List, C. Suess, A. Haase, G. Jakopic, D. Somitsch, P. Knoll, M. Bouguettaya, J. R. Reynolds and G. Leising, Thin Solid Films **433**, 287 (2003).

[1.69] C. K. Chiang, C. R. Fincher, Y. W. Park, A. J. Heeger, H. Shirakawa, E. J. Louis, S. C. Gau and A. G. MacDiarmid, Phys. Rev. Lett. **39**, 1098 (1977).

[1.70] J. H. Burroughes, D. D. C. Bradley, A. R. Brown, R. N. Marks, K. Mackay and R. H. Friend, Nature **347**, 539 (1990).

[1.71] N. Tessler, G. J. Denton and R. H. Friend, Nature **382**, 695 (1996).

[1.72] C. D. Dimitrakopoulos and P. R. L Malenfant, Adv. Mater. **14**, 99 (2002).

[1.73] N. S. Sariciftci, D. Braun, C. Zhang, V. I. Srdanov, A. J. Heeger and G. Stucky, Appl. Phys. Lett. **62**, 585 (1993).

[1.74] G. E. Wnek, J. C. W. Chien, F. E. Karasz and C. P. Lillya, Polymer **20**, 1441 (1979).

[1.75] L. Türker, J. Molecular Structure (Theochem) **588**, 121 (2002).

[1.76] M. Fukuda, K. Sawada and K. Yoshino. Jpn. J. Appl. Phys. Lett. **28**, 1433 (1989).

[1.77] J. J. Langer, Synth. Met. **20**, 35 (1987).

[1.78] G. Tourillon and F. Garnier, J. Electroanal. Chem. Interfacial Electrochem. **135**, 173 (1982).

[1.79] J. G. Speight, P. Kovacic and F. W. Koch, J. Macromol. Sci. Rev. Macromol. Chem. C **5**, 295 (1971).

[1.80] G. K. Noren and J. K. Stille, J. Polym. Sci., Part D, Macromol. Rev. **5**, 385 (1971).

[1.81] D. M. Ivory, G. G. Miller, J. M. Sowa, L. W. Shacklette, R. R. Chance and R. H. Baughman, J. Chem. Phys. **71**, 1506 (1979).

[1.82] C. Seoul, W. J. Song, G. W. Kang and C. Lee, Synth. Met. **130**, 9 (2002).

[1.83] A. W. Grice, D. D. C. Bradley, M. T. Bernius, M. Inbasekaran, W. W. Wu and E. P. Woo, Appl. Phys. Lett. **73**, 629 (1998).

[1.84] G. Heliotis, D. D. C. Bradley, G. A. Turnbull and D. W. Samuel, Appl. Phys. Lett. **81**, 415 (2002).

[1.85] M. N. Shkunov, R. Österbacka, A. Fuji, K. Yoshino and Z. V. Vardeny, Appl. Phys. Lett. **74**, 1648 (1999).

[1.86] M. Redecker, D. D. C. Bradley, M. Inbasekaran and E. P. Woo, Appl. Phys. Lett. **73**, 1565 (1998).

[1.87] M. Leclerc, J Polym Sci Part A: Polym Chem, **39**, 2867 (2001).

[1.88] M. T. Bernius, M. Inbasekaran, J. O'Brien and W. Wu, Adv. Mater. **12**, 1737 (2000).

[1.89] U. Scherf and E. J. W. List, Adv. Mater. **14**, 477 (2002).

[1.90] M. T. Bernius, M. Inbasekaran, E. Woo, W. Wu and L. Wujkowski, J Mater Sci: Mater Electron **11**, 111 (2000).

[1.91] Q. Peng, M. Xie, Y. Huang, Z. Lu and D. Xiao, J Polym Sci Part A: Polym. Chem. **42**, 2985 (2004).

[1.92] M. Kreyenschmidt, G. Klaerner, T. Fuhrer, J. Ashenhurst, S. Karg, W. D. Chen, V. Y. Lee, J. C. Scott and R. D. Miller, Macromolecules **31**, 1099 (1998).

[1.93] A. J. Cadby, P. A. Lane, H. Mellor, S. J. Martin, M. Grell, C. Giebeler and D. D. C. Bradley, Phys. Rev. B **62**, 15604 (2000).

[1.94] M. Ariu, D. G. Lidzey and D. D. C. Bradley, Synth. Met. **111–112**, 607 (2000).

[1.95] S. Kawana, M. Durrell, J. Lu, J. E. Macdonald, M. Grell, D. D. C. Bradley, P. C. Jukes, R. A. L. Jones and S. L. Bennett, Polymer **43**, 1907 (2002).

[1.96] D. D. C. Bradley, M. Grell, A. Grice, A. R. Tajbakhsh, D. F. O'Brien and A. Bleyer, Opt. Mater. **9**, 1 (1998).

[1.97] Y. K. Nakazawa, S. A Carter, H. G. Nothofer, U. Scherf, V. Y. Lee, R. D. Miller and J. C. Scott, Appl. Phys. Lett. **80**, 3832 (2002).

[1.98] U. Scherf and E. J. W. List, Adv. Mater. **14**, 477 (2002).

[1.99] Angus Rockett, *The Materials Science of Semiconductors*, Springer, (2008).

[1.100] W. Brutting, *Physics of Organic Semiconductors*, WILEY (2005).

[1.101] Jai Singh, *Optical Properties of Condense Matter and Applications*, WILEY (2006).

[1.102] D. C. Reynolds, B. M. Leies, L. L. Antes and R. E. Marburger, Phys. Rev. **96**, 533 (1954).

[1.103] W. R. Cook, L. Shiozawa and F. Augustine, J. Appl. Phys. **41**, 3058 (1970).

[1.104] NSF/RANN Tech. Rep. AER72-03478 AO4 PR 75/4, March, 1976.

[1.105] R. B. Hall and J. D. Meakin, Thin Solid Films **63**, 203 (1979).

[1.106] S. Watanabe and Y. Mita. J. electrochem. Soc. **116**, 989 (1969).

[1.107] K. W. Mitchell, A. L. Fahrenbruch and R. H. Bube, J. Appl. Phys. **48**, 4365 (1977).

[1.108] J. Britt and C. Ferekides, Appt. Phys. Lett. **62**, 2851 (1993).

[1.109] H. Noguchi, A. Setiyadi, H. Tanamura, T. Nagatomo and O. Omoto, Sol. Energy Mater. Solar Cells **35**, 325 (1994).

[1.110] D. Avellaneda, M. T. S. Nair and P. K. Nair, Thin Solid Films **517**, 2500 (2009).

[1.111] K. Subbaramaiah and V. Sundara Raja, Sol. Energy Mater. Sol Cells **32**, 1 (1994).

[1.112] M. Gunasekaran and M. Ichimura, Sol. Energy Mater. Sol. Cells **91**, 774 (2007).

CHAPTER-2

Experimental Details

CHAPTER 2: Experimental Details

2.1 Introduction

In the course of the present investigations, several experimental techniques have been used for processing and characterizing the powder and thin film samples. This Chapter describes the details of syntheses and characterization techniques used on nanostructured semiconductors, conjugated polymers and their blends.

2.2 Sample Preparations

2.2.1 Synthesis of Nanostructured Semiconductors

Nanostructured semiconducting materials are prepared by various chemical routes like Solvothermal, Hydrothermal, Aqueous solution and Polyol route. Among them Solvothermal process has various advantages.

a) This is a simple and inexpensive low temperature process.

b) During the solvothermal process, the stability of the complex precursor is expected to decrease.

c) Large scale integration may be possible by solvothermal process.

d) In this process most of the precursor materials are dissolved in a solvent easily.

We have used solvothermal process to synthesize II-VI (CdS, ZnS) and IV-VI (SnS, PbS) nanostructures due to simplicity and a good control of growth during synthesis. Details of the synthesis process are given below.

Solvothermal Synthesis Process

A solvothermal process can be defined as "*a chemical reaction in a closed system in the presence of a solvent, where the temperature is kept higher than that of the boiling point of the solvent*". Consequently a solvothermal process involves high pressures. The selected temperature depends on the required reactions for obtaining the target-material through the involved process.

The interest for non-oxide materials has led to the development of solvothermal reactions either for preparing novel materials or for setting-up new processes leading to nanostructured materials [2.1, 2.2]. Chemical reactions into a solvent under high pressure and

mild temperature conditions appear promising for developing Materials Chemistry and Materials Sciences (in particular for nanotechnologies). During the last 20 years solvothermal reactions have been mainly used from preparing micro- or nanoparticles with different morphologies. These reactions are mainly characterized by different *chemical parameters* (nature of the reagents and of the solvent) and *thermodynamical parameters* (in particular temperature, pressure and reaction time).

a) Chemical Parameters

Two different parameters can be taken into account: *the nature of the reagents and the nature of the solvent.* The chemical composition of the reagents must be appropriate to that of the target-materials. In addition, the concentration of the reagents seems to play a role on the control of the shape of nanocrystallites resulting of a solvothermal process. Wang *et al*. [2.3] through the solvothermal preparation of CdSe and CeTe nanocrystals have claimed the control of the crystallites-shape (dot, rod) with the concentration of the reagents. The interactions between reagents and solvent play an important role in the solvothermal reactions.

The selection of the solvent plays a key role through the control of the chemical mechanisms leading to the target-material. The reaction mechanisms induced, during the solvothermal reactions, are dependent on the physico-chemical properties of the solvent. Compare to non polar solvent as benzene, ethylenediamine is a polarizing solvent which increases the solubility of the reagents. In addition its complexing properties can play an important role in the reaction mechanisms. The physico-chemical properties of the selected solvent can also play an important role for orienting the structural form of the final material.

b) The Thermodynamical Parameters

These parameters are: *temperature, pressure and the reaction time*. The solvothermal reactions are mainly developed in mild temperature conditions ($T < 400$ °C). As temperature and pressure improve the solubility in major cases, any increase in values of these parameters induces an enhancement of the precursor's concentration into the solvent and then favours the growth process (in particular in the preparation of micro- or nanocrystallites).

The brief analysis of the main factors governing solvothermal reactions underlines that the nature of the selected solvent plays a key-role, in particular for controlling the chemical mechanisms involved in the solvothermal reactions.

In this thesis work nanostructured semiconductors like nanorods, disc-like nanoparticles, nanoflowers, nanoflakes, nanocubes are synthesized by solvothermal process. A teflon-lined stainless steel closed cylindrical chamber with 110 mL capacity is used for the synthesis of nanocomposites. Appropriate amount of metal source and thiourea (NH_2CSNH_2) [stoichiometric ratio 1:3] are taken in the teflon-lined chamber, which is then filled with ethylenediamine up to 80% of its volume. After 10 min of stirring, the closed chamber is placed inside a box furnace at a preset temperature of 180 to 200 °C for different reaction times (1-5 h). The precipitates are filtered off and washed several times in distilled water and ethanol. The final products are dried in vacuum desiccators at room temperature for several hours to get the powder samples. We have used cadmium nitrate [$Cd(NO_3)_2.4H_2O$] as a source of Cd for CdS nanorods formation; zinc acetate [$(CH_3COO)_2$ Zn;$2H_2O$] as a Zn source for ZnS nanoparticles formation; stannous chloride ($SnCl_2.2H_2O$) as a Sn source for SnS nano-flakes formation and lead acetate [$(CH_3COO)_2$ Pb;$3H_2O$] as a Pb source for PbS nanocubes formation separately with thiourea (NH_2CSNH_2) (a S source) as precursors and ethylenediamine (en) as a solvent. All the chemicals are of analytical grade and are used without any further purification.

2.2.2 Synthesis of Conjugated Polymers

Poly **p**ara-**p**henylene (PPP) and **p**oly**f**luorene (PF) are prepared by oxidative polymerization and Suzuki coupling methods respectively. Details of the syntheses process are given in (Chapter 5, section 5.2).

2.3 Thin Film Preparation Techniques

The thin film preparation of sulfide compounds is also a tedious job, because the solubility of these compounds is very low. For this reason, spin coating and drop casting techniques are not suitable for preparation of thin film of these materials. Also no physical deposition techniques like thermal evaporation, sputtering, laser ablation could be used to prepare these nanostructured thin films because the nanostructured would be destroyed due to high temperature. So we need a method of preparation of thin films in which the nanostructure nature is preserved in the thin films. Among the various techniques to prepare the nanostructured thin films are sol-gel route [2.4], use of self-assembled monolayers [2.5], the Langmuir-Bloggett technique [2.6], a simple dip coating method [2.7], gas-aerosol

reactive electrostatic deposition [2.8], spray pyrolysis [2.9], and spin coating [2.10]. Some of the methods are very time consuming whereas others result in a textured film. In this thesis work, thin films of the nanostructured semiconducting materials (CdS, ZnS, SnS and PbS) and conjugated polymers (PPP and PF) and their blends are prepared by doctor blade and drop casting techniques respectively on Corning 1739 and ITO coated glass substrates. Both these preparation processes are explained below. Prior to preparation of the thin films, glass substrates are ultrasonically cleaned followed by rinsing with distilled water, acetone and iso-propanol.

The doctor-blade technique [2.11-2.13] is a simple procedure involving flattening a paste containing colloidal particles onto a substrate using a squeegee, resulting in smooth thin films. The thickness of the films can be easily controlled by concentration of the paste. To study the structural (XRD and SEM), optical (UV-Vis and PL) and electrical transport properties of these materials, thin films of CdS, ZnS, SnS and PbS nanostructures are prepared using doctor's blade technique. For preparation of thin films, Sulfide compounds (5 mg) are added into a mortar, and then 0.5 mg of ethyl cellulose (binder) and 1 mL of terpineol (solvent) are mixed with sulfides by grinding until a uniform concentrated gel is formed. A drop of the paste is added to the Corning 1739 and ITO coated glass substrates and flattened with a sharp knife followed by drying at 60 °C for about 10-12 h.

Drop casting technique is used to prepare thin films of neat and nanostructured alloyed conjugated polymers. Here polymers like PPP and PF and their blends are first dissolved in tetrahydrofuron (THF) or chloroform solvents and ultasonicated for at least 3 h until the polymers are totally dissolved in the solvents. Then the solution is drop-casted on the Corning 1739 and ITO coated glass substrates.

2.4 Characterizations and Models Used

Nanostructured semiconductor and conjugated polymers exist in many structural forms and therefore require a large range of experimental techniques for their physical and chemical analyses. In the following section, we briefly review the various techniques used for the physical and chemical characterization of the nanostructures synthesized during the course of study.

2.4.1 Structural Characterizations

a) X-ray Diffraction (XRD)

X-ray powder diffraction (XRD) is one of the most powerful techniques for qualitative and quantitative analysis of compounds. The technique provides information that cannot be obtained any other way. The information obtained includes types and nature of crystalline phases present, structural make-up of phases, degree of crystallinity, and amount of amorphous content, micro strain and orientation of crystalline. Room temperature x-ray diffraction measurements are carried out by Bruker D8 Advance using CuK_α radiation (λ = 1.54056 Å) with scanning rate of 0.05 °/s for 2θ range from 20-90° for all the samples. In the present investigation, all the XRD data are collected with the setting of 30 mA current and 40 kV voltages for X-ray generator. The data are collected in a usual θ-θ scan with an angular speed 1-2 °/min and a step size of 0.03-0.05°. Diffraction measurements of the powder and thin film samples are taken in powder mode and thin film mode respectively.

The grain size (D) values are calculated from the peak broadening using the Scherrer's formula [2.14].

$$D = \frac{0.9\lambda}{\beta \cos\theta} \quad \ldots\ldots\ldots\ldots\ldots\ldots\ldots\ldots\ldots\ldots\ldots\ldots \quad (2.1)$$

where λ is the wavelength of the X-ray used (1.54056 Å), β is the full-width at half-maximum (FWHM) of the peak which has maximum intensity and θ is the Bragg's angle.

The dislocation density (δ) defined as the length of dislocation lines per unit volume, has been estimated using the equation

$$\delta = \frac{1}{D^2} \quad \ldots\ldots\ldots\ldots\ldots\ldots\ldots\ldots\ldots\ldots\ldots\ldots \quad (2.2)$$

δ is the measure of the number density of defects in a crystal.

The number of crystallites per unit area (N) and the strain (ε) of the films are determined with the use of the following formulae:

$$N = \frac{t}{D^3} \quad \ldots\ldots\ldots\ldots\ldots\ldots\ldots\ldots\ldots\ldots\ldots\ldots \quad (2.3)$$

$$\varepsilon = \frac{\beta \cos\theta}{4} \quad \ldots\ldots\ldots\ldots\ldots\ldots\ldots\ldots\ldots\ldots\ldots\ldots \quad (2.4)$$

b) Transmission Electron Microscopy (TEM)

Transmission electron microscope (TEM, JEOL JEM 2100) has been used to study the microstructure of the powders. For TEM observation, the sample in the form of powder has been dispersed in ethanol solvent followed by ultrasonication at least 1 h. A drop of the colloidal solution is placed on a carbon coated copper TEM grid (Mesh 400) and allowed to dry in a clean environment. The grid with the dried powder particles has been used for the TEM observation. Here, electron beams are accelerated with voltages of 200 kV and 100 μA of currents for TEM observations. In case of HRTEM, spot size is varied from 20-200 nm and images are taken at a magnification of $6x10^5$ to 10^6. During the observations of SAED patterns field-limiting aperture is inserted. For IFFT measurements, first we take FFT of a HRTEM image. Two bright spots appeared after masking with Gatan software which is installed in the TEM instrument.

c) Scanning Electron Microscopy (SEM)

Morphological and compositional analysis of the powders as well as thin films are observed by scanning electron microscopy (SEM, LEO 1430 VP) and EDAX which is usually attached in SEM instrument.

The electrons are accelerated in a potential difference typically of the order of 10-20 keV and focused on a spot volume of the specimen, resulting in the transfer of energy to the spot. In the present work, a very thin layer of powder has been spread on carbon coated tape and then gold coated to yield an electrically conducting surface for SEM and EDAX observations. EDAX is done by Oxford INCA software which is installed in SEM instrument.

2.4.2 Optical Characterizations

a) UV-Visible Transmittance and Absorbance

UV-Vis-NIR spectrophotometer (Shimadsu UV 3101PC) is used to determine the absorption or transmission of UV/VIS light (200 to 3000 nm) by a sample (powders or thin films). It can also be used to measure concentrations of absorbing materials based on developed calibration curves of the material. For measurements of transmittance and absorbance, powder samples are ultrasonically dispersed in ethanol for 3 h and then placed in a quartz cuvette. For absorbance and transmittance measurements of thin films, samples are placed in a sample holder and then scan for the wavelength range of 200-3000 nm. Step size

of the data reading is 1 nm. Band gap of the semiconductors are calculated from the onset of the UV-Vis absorption spectra.

b) Photoluminescence

Photoluminescence (PL) is a process in which a substance absorbs photons (electromagnetic radiation) and then re-radiates photons of lower energy. Quantum mechanically, this can be described as an excitation to a higher energy state and then a return to a lower energy state accompanied by the emission of a photon. This is one of many forms of luminescence (light emission) and is distinguished by photoexcitation (excitation by photons), hence the prefix *photo-*. The time period between absorption and emission is typically extremely short, of the order of 10 nanoseconds. PL is carried out by Aminco Bowman Series 2 Luminescence Spectrometer in case of our powder and thin film samples. For PL measurements of the powder samples, powders are ultrasonically dispersed in ethanol for 3 h and then placed in a quartz cuvette. Optical filters (450 nm, 500 nm) are used at the emission site to cut the higher order harmonics of the excitation wavelength. Photoluminescence excitation (PLE) is also measured with a fixed emission wavelength (e.g. 520 nm for CdS nanorods thin films). Step size of the data reading is 1 nm.

c) Raman Spectroscopy

In this thesis work, Raman spectroscopy of all the as-synthesized powder samples are observed by Lab RAM HR instrument excited by 488 nm of Ar ion laser with 2 mW incident power. The spot size of the incident laser is around 5 μm and the laser exposure times are varying from 20-120 sec. Data is recorded in the range of 50-1500 cm^{-1}. Peak positions of the CdS, ZnS, SnS and PbS nanostructured powder samples are assigned by the reported data.

2.4.3 Thermal Characterization

a) Thermo Gravimetric Analysis (TGA)

Thermal stability studies are carried out by Thermo gravimetric analysis (TGA, METTLER TOLEDO, TGA/SDTA851^e). Thermo-gravimetry is a technique which measures the mass change of a sample as a function of temperature in the scanning mode or as a function of time in the isothermal mode. Thermal events do not bring about a change in the mass of the sample, such as melting crystallization and glass transition, but thermal changes

accompanying mass change, such as decomposition, sublimation, reduction, desorption, absorption and vaporization, can be measured by TG. Thermal stability of the nanostructured compound semiconductors (CdS, ZnS, SnS and PbS) and the conjugated polymers (PPP and PF) are studied by TG instrument under inert atmosphere of Ar at the temperature range of room to 900 °C with heating rate of 10 °C/min.

b) Determination of Kinetic Parameters

Kinetic parameters of thermal degradation can be measured by different kinetic models like Ozawa method [2.15], Kissinger method [2.16], Coats-Redfern model [2.17], Freeman-Carroll method [2.18], Avrami method [2.19] etc. Among these, Coats-Redfern and Freeman-Carroll methods are simple and requires only one heating rate whereas other methods are required at least four heating rates. Due to this simple process we have chosen Coats-Redfern and Freeman-Carroll methods which are explained below:

i) Coats-Redfern Model [2.17]

Coats-Redfern model is used to obtain the kinetic parameters such as thermal activation energy (E), Arrhenius parameter (A) and change of entropy (ΔS) of the nanostructured compound semiconductors.

Any kind of degradation is commonly describe by the equation

$$\frac{d\alpha}{dt} = A\exp(-\frac{E}{RT})g(\alpha) \quad \text{..... (2.5)}$$

By integrating the reaction kinetic equation (2.5) and rearranging it, the following Coats-Redfern equation can be obtained as:

$$\ln[\frac{g(\alpha)}{T^2}] = \ln[\frac{AR}{\Phi E}(1-\frac{2RT}{E})] - \frac{E}{RT} \quad \text{..... (2.6)}$$

where g(α) is the kinetic model function, α is the fraction decomposed at any temperature, and Φ is the heating rate.

In this thesis work all TG data are analyzed using the nine mechanistic equations (Table 2.1) proposed by Satava [2.20]. Results of the analysis are used to derive the best fit curves with the highest correlation coefficients. We observe that the best fits are obtained for g(α) = [-ln (1-α)] = kt, where k is the Boltzmann constant and t is the time. This relation corresponds to random nucleation with one nucleus on each particle.

The slope of the plot of $\ln[\frac{g(\alpha)}{T^2}]$ against 1/T is a straight line, from which the thermal activation energy (E) is calculated. The pre-exponential factor Arrhenius parameter (A) is also calculated from intercept of curve on Y-axis which is equal to $\ln[\frac{AR}{\Phi E}]$.

The entropy of activation (ΔS) of the thermal decomposition is also calculated for each nanocomposite using the relationship,

$$A = (kT_S / h)\, e^{\Delta S/R} \quad \ldots\ldots\ldots\ldots\ldots\ldots\ldots\ldots\ldots\ldots\ldots\ldots \; (2.7)$$

where A is the Arrhenius parameter, k is the Boltzmann constant, T_S is the peak temperature, h is the Plank's constant and R is the gas constant.

Table 2.1: Kinetic Equations: Nine mechanistic equations proposed by Satava

Function	Equation	Rate-controlling process
D_1	$\alpha^2 = kt$	One-dimensional diffusion
D_2	$(1-\alpha)\ln(1-\alpha) + \alpha = kt$	Two-dimensional diffusion, cylindrical symmetry
D_3	$[1-(1-\alpha)^{½}]^2 = kt$	Three-dimensional diffusion, spherical symmetry; Jander equation
D_4	$(1-¼\,\alpha) - (1-\alpha)^{2/3} = kt$	Three-dimensional diffusion, spherical symmetry; Ginstling-Brounshtein equation
F_1	$-\ln(1-\alpha) = kt$	Random nucleation, one nucleus on each particle
A_2	$\sqrt{-\ln(1-\alpha)} = kt$	Random nucleation; Avrami equation I
A_3	$\sqrt[3]{-\ln(1-\alpha)} = kt$	Random nucleation; Avrami equation II
R_2	$1-(1-\alpha)^{1/2} = kt$	Phase boundary reaction, cylindrical symmetry
R_3	$1-(1-\alpha)^{1/3} = kt$	Phase boundary reaction, spherical symmetry

ii) Freeman and Carroll Method [2.18]

This method is known as the difference-differential method. From one thermal analysis curve (e.g. a TG curve), first determining mass-loss conversion and rate, reciprocal of temperature at some points on the TG curve and then their differences between two adjacent points, kinetic parameters can be obtained schematically according to following equation:

$$-\frac{E}{2.3R}\left[\frac{\Delta(\frac{1}{T})}{\Delta \log C}\right]=\frac{\Delta \log(\frac{dC}{dt})}{\Delta \log C}-n \quad \ldots\ldots\ldots\ldots\ldots\ldots\ldots\ldots\ldots (2.8)$$

where C is the concentration of reacting species, $\frac{dC}{dt}$ the mass-loss rate at time t, T the temperature (K), *n* the order of reaction, E the thermal activation energy (kJmol^{-1}) and *R* the gas constant (8.314 Jmol^{-1}K^{-1}). When the mass-loss rate obviously changed, the selected temperature interval should be decreased.

2.4.4 Electrical Characterization

Electrical transport studies on the thin films of CdS, ZnS, SnS and PbS nanostructured, PPP and PF conjugated polymers and their blends are carried out by two probes method with variable temperature (room temperature to 473 K) placed in high vacuum metallic chamber. The evaporated Al or Ni contacts in coplanar as well as sandwich geometry are used for electrical measurements. The length and separation of the electrodes are about 7 mm and 2 mm respectively in coplanar geometry, where as a dot of 3 mm diameter is used as one of the electrode (front contact) for sandwich geometry where ITO back contact acts as other electrode.

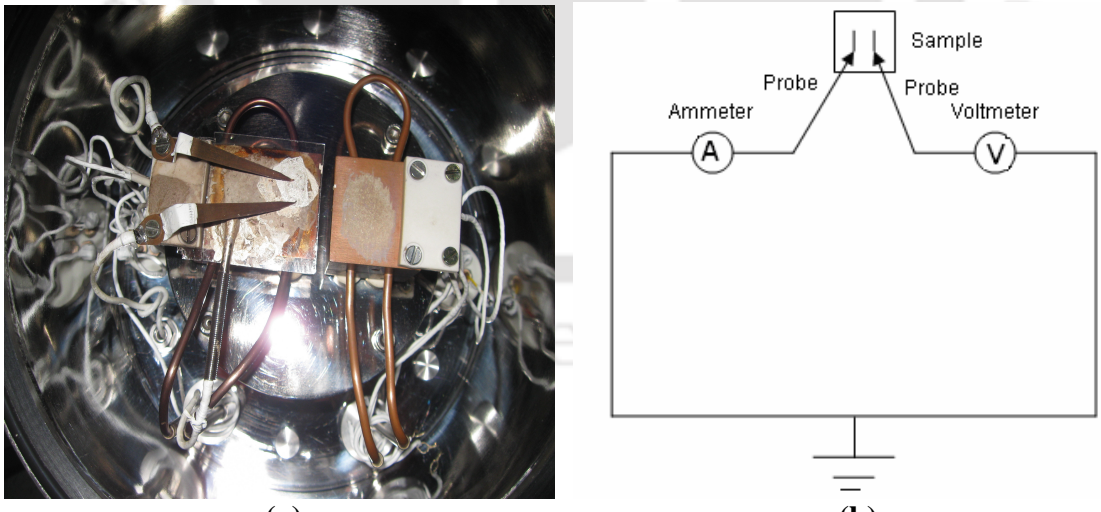

(a) **(b)**

Figure 2.1: (a) Top view of the transport measurement unit and (b) Schematic diagram of the two probes method.

Persistent photocurrents (PPC), rise and decay of photocurrents and intensity variation of photocurrents are also measured by transport measurement unit (Figure 2.1). During PPC measurements, samples are kept at different stable temperatures (like 30, 50, 70 °C etc.) and then light is shone for 3 min. The rise of photocurrent is measured at a time interval of 10 sec immediately after switching on the light. Measurements are also done for decay of photocurrent at an interval of 10 sec after switching off the light. During intensity variation of photocurrent measurements, combinations of ND filters are used to reduce the light intensity. Measurements are done for increasing intensity of light.

Current and voltage are measured by Keithley 6430 Sub-Femtometer. Temperature of the samples is measured by PT100 thermocouple connected with Keithley 2000 Multimeter. ScientiFic Power Supply (PSD3003) is used for heating the filaments and Ablab Regulated DC Power Supply (L1282) is used as a voltage source.

Monochromator is used to study the spectral response and I-V characteristics of the p-SnS/n-CdS based heterojunction solar cells. During this thesis work, red (wavelength = 632.8 nm and power =30 mW) and green (wavelength = 543 nm and power = 2 mW) HeNe Lasers are also used for various optical and electrical transport measurements.

Thermally activated dark and photoconductivity is explained by Arrhenius equation which is given below [2.21]: The Arrhenius equation is a simple, but remarkably accurate, formula for the temperature dependence of the rate constant. The equation is first proposed by the Dutch chemist J. H. van't Hoff in 1884; five years later in 1889, the Swedish chemist Svante Arrhenius provides a physical justification and interpretation for it. Nowadays it is best seen as an empirical relationship. It can be used to model the temperature-variance of diffusion coefficients, population of crystal vacancies, creep rates, and many other thermally-induced processes/reactions. Equation is as the form of

$$\sigma = \sigma_0 \exp(-\frac{E_a}{kT}) \quad \ldots\ldots\ldots\ldots\ldots\ldots\ldots\ldots (2.9)$$

where σ_0 is the pre-exponential factor, E_a is the activation energy, k is Boltzmann constant and T is the absolute temperature. Dark and photoconductivity are measured in the temperature range of 300-463 K. Electrical activation energy for dark and photoconductivity is measured from the slope of the curves drawn from σ vs 1000/T.

2.5 References

[2.1] G. Demazeau, J. Mater. Chem. **9**, 15 (1999).

[2.2] S. H. Yu, J. Ceram. Soc. Jpn. **109**, 565 (2001).

[2.3] Q. Wang, D. Pan, S. Jiang, X. Ji, L. An and B. Jiang, J. Cryst. Growth **286**, 83 (2006).

[2.4] L. Spanhel and M. A. Anderson, J. Am. Chem. Soc. **112**, 2278 (1990).

[2.5] V. L. Colvin, A. N. Goldstein and A. P. Alivisatos, J. Am. Chem. Soc. **114**, 5221 (1992).

[2.6] B. O. Dabbousi, C. B. Murray, M. F. Rubner and M. G. Bawendi, Chem. Mater. **6**, 216 (1994).

[2.7] A. Chemseddine and M. L. Fearheiley, Thin Solid Films **247**, 3 (1994).

[2.8] O. V. Salata, P. J. Dobson, P. J. Hull and J. L. Hutchison, Thin Solid Films **251**, 1 (1994).

[2.9] R. R. Chamberlin and J. S. Skarman, J. Electrochem. Soc. **113**, 86 (1966).

[2.10] D. Kulik, H. Htoon, C. K. Shih and Y. Li, J. Appl. Phys. **95**, 1056 (2004).

[2.11] H. Jia, Y. Hu, Y. Tang and L. Zhang, Electrochem. Commun. **8**, 1381 (2006).

[2.12] L. C. Pathak, Ceramics International **30**, 417 (2004).

[2.13] S. J. Ahn, K. H. Kim and K. H. Yoon, Curr. Appl Phys. **8**, 766 (2008).

[2.14] K. Ravichandran and P. Philominathan, Appl. Sur. Sci. **255**, 5736 (2009).

[2.15] T. Ozawa, Bull. Chem. Soc. Jpn. **38**, 1881 (1965).

[2.16] H. E. Kissinger, Anal. Chem. **29**, 1702 (1957).

[2.17] W. Coats and J. P. Redfern, Nature **201**, 68 (1964).

[2.18] T. Hatakeyama and Z. Liu, *Handbook of Thermal Analysis*, John Wiley & Sons (1998).

[2.19] Z. Zhang, Chin. J. Polym. Sci. **11**, 125 (1993).

[2.20] V. Satava, Thermochim. Acta **2**, 423 (1971).

[2.21] http://en.wikipedia.org/wiki/Arrhenius_equation.

CHAPTER-3

Synthesis and Studies of II-VI Nanostructured Semiconductors

CHAPTER 3: Synthesis and Studies of II-VI Nano-structured Semiconductors

3.1 Introduction

The synthesis of binary metal (group II) chalcogenides semiconductors has received much attention during the last few decades due to their important nonlinear optical properties, luminescent properties, quantum confinement effect and other important physical and chemical properties. Considerable progress has been made in the synthesis of group II-VI semiconductor micro-crystallites and nano-crystallites. These materials form defects and interdiffuse at high temperature (above 500 °C); so low temperature synthesis process is required to prepare defects free II-VI crystalline materials [3.1]. Among the II-VI semiconductor, nanocrystals like Cd(S, Se, Te) and Zn(S, Se, Te) have attracted more interest due to their potential applications in photovoltaic devices, photoresistors, non-linear optical materials, light emitting diodes, emissive flat screens, electroluminescent devices, antireflection coating in solar cell technology and optical sensors [3.2-3.12].

The advantages of using CdS and ZnS are due to their favorable properties such as: (a) direct wide band gap (E_g = 2.41 eV for CdS and 3.61 eV for ZnS), (b) high absorption coefficient ($\alpha > 10^4$ cm^{-1}), (c) good conversion efficiency, (d) high thermal stability and (e) easy to syntheses. Due to their wide band gap, CdS and ZnS are also used as a window layer as well as n-type semiconducting material in heterojunction solar cells [3.13]. The significant changes in optical, mechanical, thermal and other properties are observed when the particle size is close to or less than the excitonic Bohr radius. In CdS, such quantum size effects are observed for crystallites dimensions below 50 Å which is approximately the Bohr exciton diameter in CdS.

Because of the increasing interest in nanostructures of materials in device applications, it is necessary to extensively study the various physical properties of these structures in detail. In this thesis work, CdS and ZnS nanostructures have been prepared by solvothermal process for three different reaction times and their different structural, optical, thermal and electrical properties have been studied. CdS and ZnS nanostructures have shown high thermal stability and good optical properties, good photo and dark conductivity. CdS thin films have also shown persistent photocurrent (PPC). The observed PPC and its slow

decay with time in case of CdS nanostructured thin films have been explained by potential barrier fluctuation model.

3.2 Experimental Details

3.2.1 Syntheses of II-VI Nanostructures

i) CdS Nanorods

CdS nanorods are synthesized by solvothermal process using cadmium nitrate ($Cd(NO_3)_2.4H_2O$) and thiourea (NH_2CSNH_2) in ethylenediamine (*en*) solvent at a temperature of 200 °C for three different reaction times 1 h, 3 h and 5 h respectively. Details of the synthesis process are given in (Chapter 2, section 2.2). The formation of CdS nanorods takes place as per the following reactions [3.14]:

$$Cd(NO_3)_2.4H_2O \leftrightarrow Cd^{2+} + NO_3^- + H_2O$$
$$NH_2CSNH_2 + 2OH^- \Leftrightarrow CH_2N_2 + H_2O + S^{2-}$$
$$Cd^{2+} + n(en) \Leftrightarrow Cd(en)_n^{2+}$$
$$Cd(en)_n^{2+} + S^{2-} \rightarrow CdS(en)_n \leftrightarrow CdS + n(en) \quad \ldots\ldots\ldots (1)$$

First, Cd^{2+} ion coordinates with *en* molecule to form $Cd(en)_3^{2+}$. Thiourea decomposes to produce S^{2-} at low temperature in the base environment. Then, the reaction between $Cd(en)_3^{2+}$ and S^{2-} produces CdS powder with its surface-adsorbed *en* molecule. Meanwhile, the conformation of the *en* molecule coordinated with Cd^{2+} changes from the gauche to the trans conformation. However, the interaction between the *en* molecules and Cd^{2+} on the surface of CdS is weak when the *en* molecule is in the trans conformation. Therefore, this structure is destroyed at high temperatures. This dissociation of the *en* molecules from the surface of CdS results in the evolution process of the morphology. In fact, the *en* molecule in the trans conformation act as an intermediate.

ii) ZnS Nanostructures

ZnS nanostructures are synthesized by solvothermal process using zinc acetate [$(CH_3COO)_2\ Zn;2H_2O$] and thiourea (NH_2CSNH_2) in *en* solvent at a temperature of 180 °C

for three different reaction times 1 h, 3 h and 5 h respectively. Details of the synthesis process are given in (Chapter 2, section 2.2). A possible growth mechanism for the formation of the ZnS nanostructures has been presented below. In this synthesis, firstly, *en* as a strongly bidentating solvent, is ready to form relatively stable Zn^{2+} complexes. Next, the thiourea employed as the sulfur source is inclined to decompose at such a high temperature (180 °C) and generate S^{2-} ions slowly and homogeneously. The S^{2-} ions react with the Zn^{2+} ions that has chelated with ethylenediamine in a reversible and effective pathway to produce ZnS, which precipitates. Following reactions take place during the synthesis process [3.15]:

$$(CH_3COO)_2Zn;2H_2O \rightarrow Zn^{2+} + (CH_3COO)^- + H_2O$$
$$(NH_2)_2CS + 2OH^- \Leftrightarrow CH_2N_2 + H_2O + S^{2-}$$
$$Zn^{2+} + 2en \Leftrightarrow Zn(en)_2 + S^{2-} \Leftrightarrow ZnS \downarrow + 2en \quad \text{..... (2)}$$

Here for both CdS and ZnS compounds, three different reaction times have been chosen to study the evolution of nanostructures and how their optical, thermal and electrical properties change with the increase of reaction times.

3.2.2 Characterizations and Studies

The various structural, optical, thermal and electrical properties of as-prepared CdS and ZnS powder samples are studied using different characterization tools. The crystallinity of the samples is examined using X-ray diffraction (XRD). Surface morphology of the powder samples are observed by scanning electron microscopy (SEM) and transmission electron microscopy (TEM). Compositional analysis is carried out by energy dispersive analysis of X-ray (EDAX) attached with SEM instrument. Raman spectroscopy studies on these powder samples are carried out by Raman instrument with 488 nm Ar ion laser of 2 mW incident power. Thermal stability of these powder samples is investigated by TGA at inert atmosphere of Ar.

For measurement of optical and electrical transport, thin films of CdS and ZnS nanostructures are prepared using doctor's blade technique (Chapter 2, section 2.3). The films are found to be of nearly uniform thickness as seen by cross-sectional SEM measurement. The thicknesses of different films prepared by this technique ranges from 1.5-2 μm for CdS and 8-9 μm for ZnS. UV-Vis-NIR transmission and absorbance as well as photoluminescence

studies on the CdS and ZnS thin films prepared on Corning 1739 glass substrate are also investigated.

Electrical transport measurements are done on CdS thin films prepared on Corning 1739 glass substrate (in coplanar geometry) and ZnS thin films prepared on ITO coated glass substrates (in sandwich geometry). Silver paste is used as a front electrode (with electrode width = 2 mm and length = 6 mm). The samples are mounted inside a metallic chamber with a transparent window. All the measurements are made in vacuum. A 100 W halogen lamp with 10 mW/cm^2 intensity is used for illumination. Transport measurements are done while heating as well as cooling the samples and no difference in log σ vs 10^3/T is observed during the two cycles.

3.3 Results and Discussions

3.3.1 CdS Nanorods

a) Structural Properties

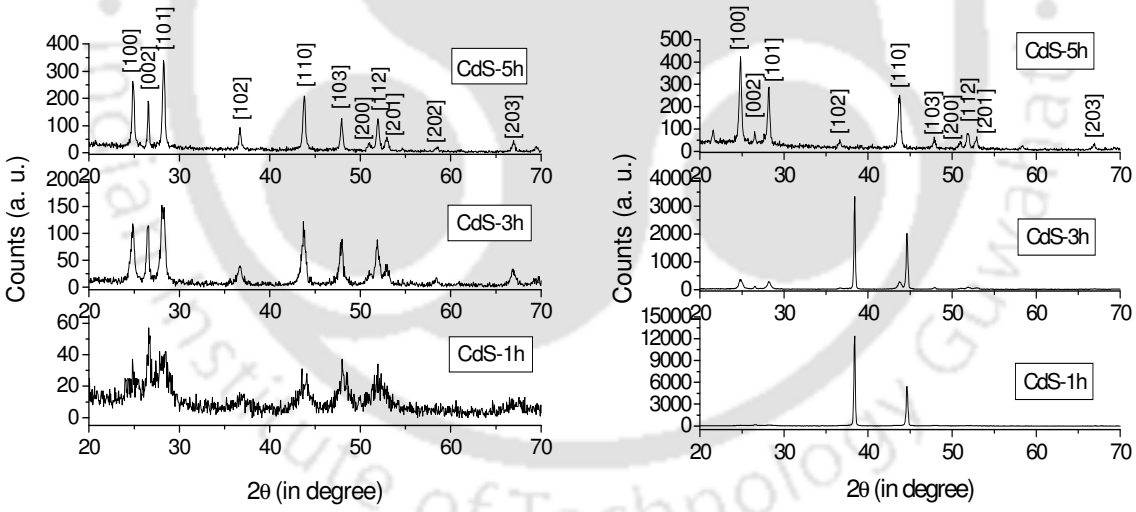

(a) **(b)**

Figure 3.1: XRD patterns of the CdS nanorods (a) powder samples and (b) thin films prepared for three different reaction times.

Figure 3.1 show the XRD patterns of the CdS nanorods powder samples as well as thin films. No differences in peak positions for powder and thin films have been observed. XRD studies suggest that the CdS nanorods have hexagonal closed pack (Wurzite) structure

with lattice parameters *a*= 4.14 Å and *c*= 6.719 Å, which is very close to the reported data (JCPDS Card File, No. 41-1049). Broad peaks are observed in case of CdS powder samples prepared for 1 h reaction time which could be due to the very small particle size. As the reaction time is increased XRD patterns become sharper which suggests that the particle sizes of the CdS powder samples increased with the increase of reaction times. Very sharp diffraction peaks are observed for 5 h reaction times which indicate that CdS has very high crystallinity. Average grain size (D), dislocation density (δ), number of crystallites per unit area (N) and the strain (ε) of the CdS prepared for three different reaction times are obtained from XRD which are summarized in Table 3.1.

Table 3.1: Physical parameters of the CdS nanostructured obtained from XRD data

Sample	Grain size (D) (nm)	Dislocation density (δ) (lines/m^2)	Number of crystallites per unit area (N)	Strain (ε)
CdS-1h	15	4.44×10^{15}	1.48×10^{18}	4.43×10^{-3}
CdS-3h	24	1.74×10^{15}	3.62×10^{17}	1.57×10^{-3}
CdS-5h	39	6.57×10^{14}	3.37×10^{16}	1.60×10^{-3}

Figure 3.2 show the TEM images of the CdS powder samples prepared for three different reaction times. TEM images (Figure 3.2a) of the CdS powder samples prepared for 1 h reaction time suggest that these nanorods are irregular in shape, with typical diameter and length varies from 10-20 nm and 80-100 nm respectively. HRTEM image of the 1 h sample suggests the low quality growth with high dislocations of the atoms. SAED pattern of the sample prepared for 1 h reaction time consists of several diffused diffraction rings, which also indicates that sample is poorly crystallized. These results are consistent with those obtained from XRD pattern. TEM images of the 3 h (Figure 3.2b) and 5 h (Figure 3.2c) samples suggest that these materials are uniform throughout their lengths. Typical diameter and length of the nanorods varies from 40-50 nm and 450-750 nm respectively. The high quality growths of these nanorods are also confirmed by HRTEM images and its inverse first Fourier transforms (IFFT). IFFT image further confirms that CdS nanorods are totally defects free consisting of well oriented single crystalline materials with the lattice spacing of 3.23 Å corresponding to [200] plane. The SAED patterns of the 3 h and 5 h powder samples also confirm the single crystalline structures. From TEM studies, the aspect ratio of these CdS nanorods is calculated to be in the range of 11-15. The CdS nanorods thus have very high surface to volume ratio, making these ideal for sensor applications.

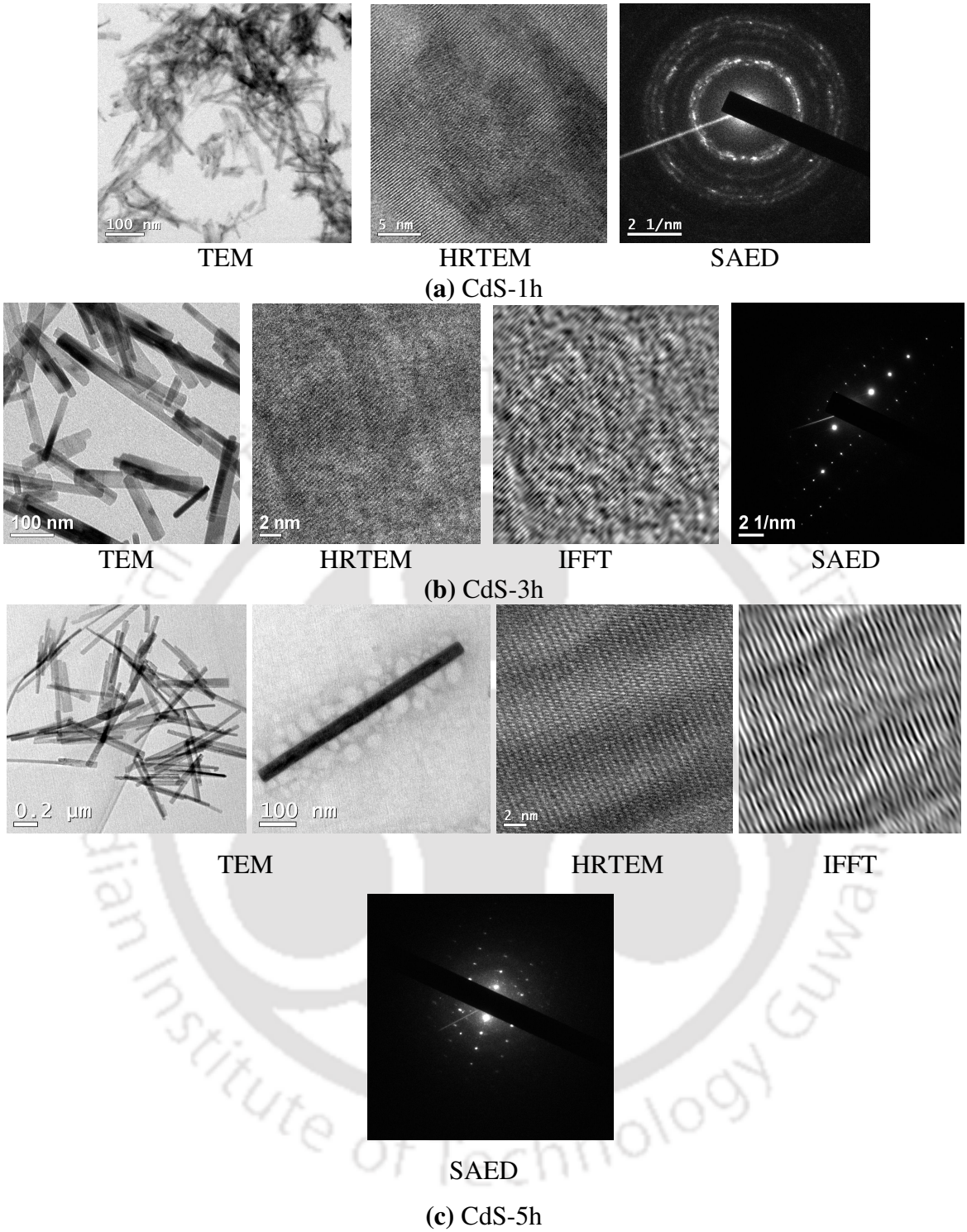

Figure 3.2: TEM, HRTEM, IFFT and SAED patterns of the CdS nanorods powder samples prepared for three different reaction times.

The SEM images of CdS powders and thin film are given as Figure 3.3a and 3.3b respectively. The CdS nanorods are found to be chemically pure and there is slight sulfur deficiency as obtained by EDAX (Figure 3.4). The stoichiometric ratios of these powder

samples prepared for three different reaction times are summarized in Table 3.2. Due to the slight sulfur deficiency, CdS become n-type in nature for excess electrons from Cd sites. From the image for thin film, it is clear that CdS nanorods are nicely grounded on the ethyl cellulose binder and no pin holes are observed throughout the films. The structural studies confirm that the nanorods are not destroyed while preparing thin films.

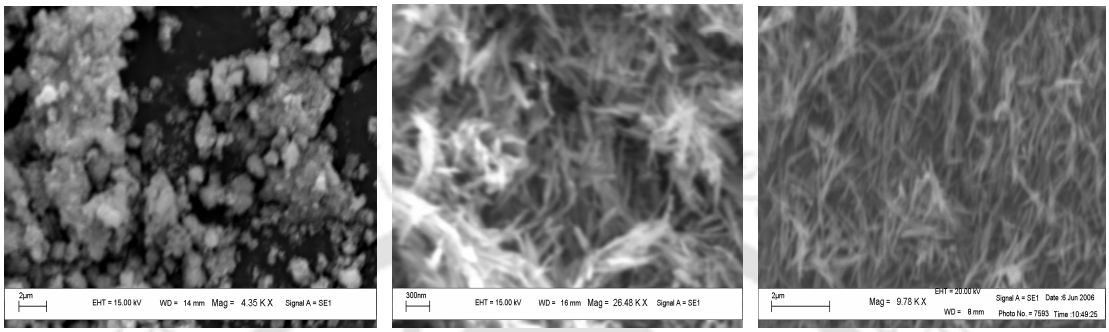

CdS-1h CdS-3h CdS-5h

(a)

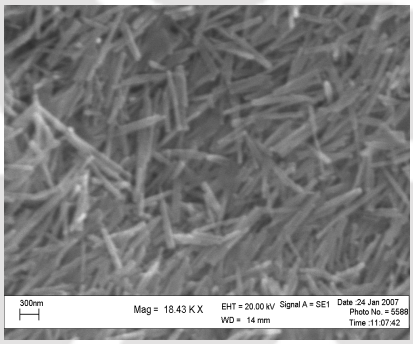

CdS-5h thin film

(b)

Figure 3.3: SEM images of the CdS nanorods (a) powder samples and (b) thin film.

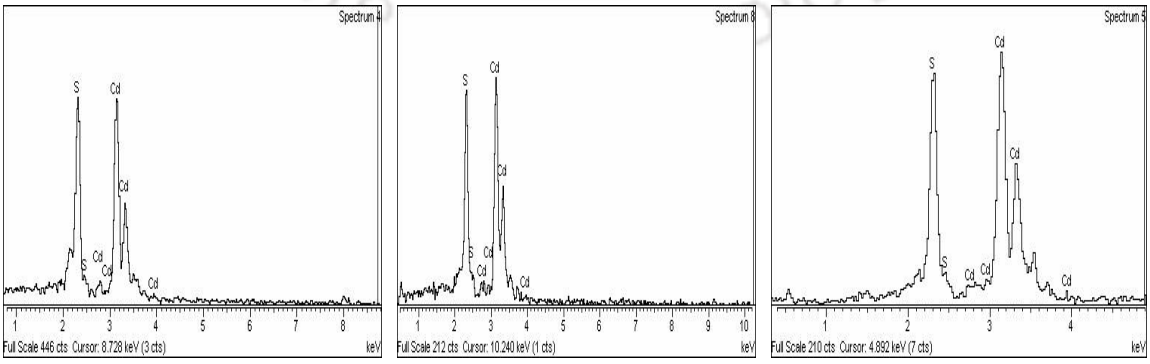

CdS-1h CdS-3h CdS-5h

Figure 3.4: EDAX patterns of the CdS nanorods powder samples.

Table 3.2: Stoichiometric ratios of CdS nanorods powder samples

Sample	Cd	S
CdS-1h	52.50	47.50
CdS-3h	52.46	47.54
CdS-5h	52.51	47.49

b) Optical Properties

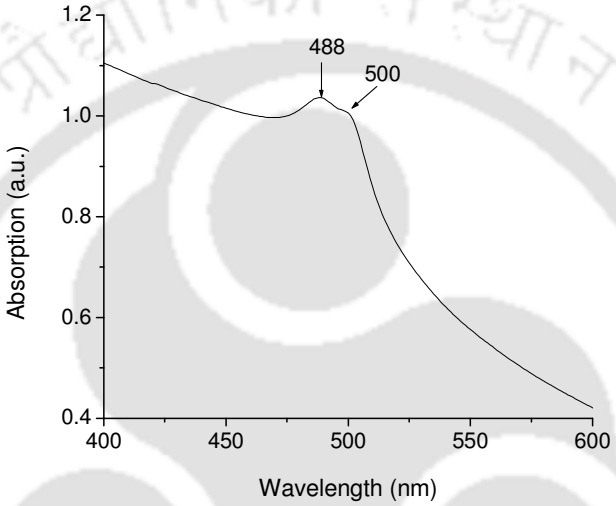

Figure 3.5: Optical absorption spectra of the CdS nanorods solution prepared for 5 h reaction time in ethanol solvent.

For optical absorption studies, CdS nanorods powder samples are ultrasonically dispersed in spectroscopic grade ethanol. The room temperature UV-Vis absorption spectrum for 5 h (Figure 3.5) sample shows a sharp rise at 500 nm with a small peak at 488 nm indicating the band gap in the range of 2.42-2.54 eV. Compared with the characteristics absorption (≥500 nm) of bulk CdS, a blue-shift to 488 nm is indicative of size quantization effect. In earlier studies, Yu *et al*. [3.1] and Li *et al*. [3.16] have observed an absorption peak at 485 nm and 480 nm respectively for CdS nanorods powder samples synthesized in *en* solvent which supports that our results are consistent with the reported ones.

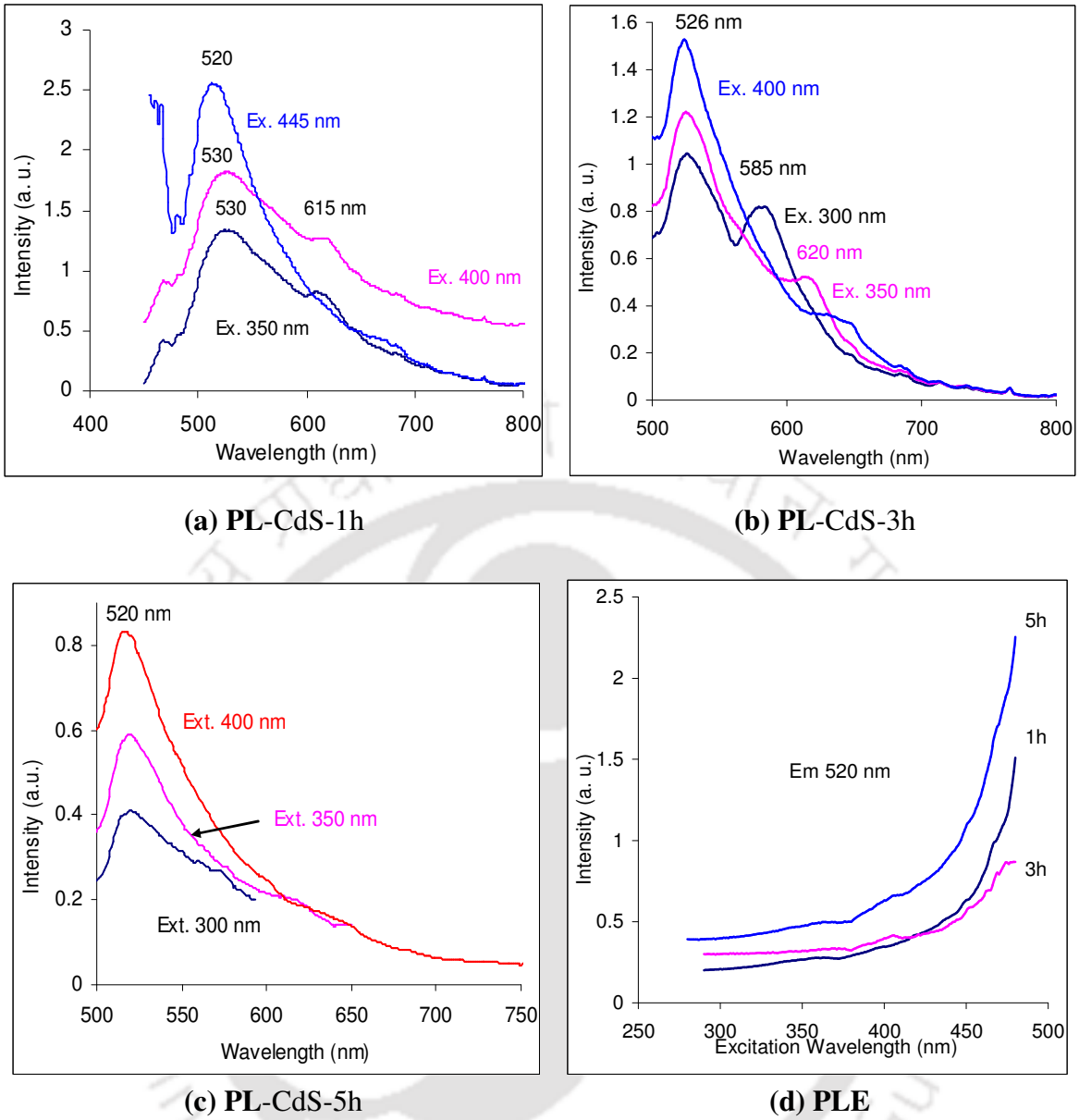

(a) PL-CdS-1h **(b) PL-CdS-3h**

(c) PL-CdS-5h **(d) PLE**

Figure 3.6: PL and PLE spectra (fixed at 520 nm of emission wavelength) of the CdS nanorods thin films prepared for three different reaction times.

Photoluminescence (PL) studies are done on the CdS nanorods thin films for three different excitation wavelengths at room temperature. A sharp emission peak is observed at 520 nm for excitation wavelengths of 445, 400 and 350 nm. In addition to this sharp peak, a broad emission peak at 530 nm and a small peak at 615 nm are also observed for 400 and 350 nm of excitation wavelengths for 1 h sample (Figure 3.6a). In case of 3 h sample a sharp emission peak is observed at 526 nm for all three different excitations (300, 350 and 400 nm) and a small peak at 585 nm and 620 nm is also observed for excitation wavelength 300 nm and 350 nm respectively (Figure 3.6b). Only one sharp peak at 520 nm is observed for 5 h

sample for all three excitation wavelengths (300, 350 and 400 nm) (Figure 3.6c). Figure 3.6d shows the photoluminescence excitation (PLE) spectra of the CdS nanorods prepared for three different reaction times. From PLE spectra (emission wavelength fixed at 520 nm) it is clear that CdS nanorod thin films have good emission spectra for excitation wavelength range 300-450 nm. In previous studies, Liu *et al*. [3.17] have reported that there are two emission bands for CdS nanoclusters. One is the green emission peak at 552 nm; other is the broad red emission at 744 nm. Xu *et al*. [3.18] have also observed two luminescence peaks at 680 nm and 760 nm (IR), which are attributed to the formation of the sulfur vacancies (V_s) and Cd-S composite vacancies ($V_{Cd\text{-}S}$), respectively. Moore *et al*. [3.19] have observed that Q-CdS shows the band edge PL peak centered at 450 nm. In our studies, a PL peak centered at around 520 nm (corresponding optical band gap is 2.38 eV) is observed for all these three samples for three different excitation wavelengths. It is also observed that the position of the second peak shifts to lower energy with lower excitation energy. Therefore, it is suggested that the PL spectra exhibit two bands: the first band around 2.38 eV is due to exciton recombination mostly in delocalized states in nanocrystals (the band-edge emission) and the second band around (2.13 eV for 300 nm, 1.99 eV for 350 nm and 1.9 eV for 400 nm excitations respectively) due to recombination via surface-localized states (the trap-state emission).

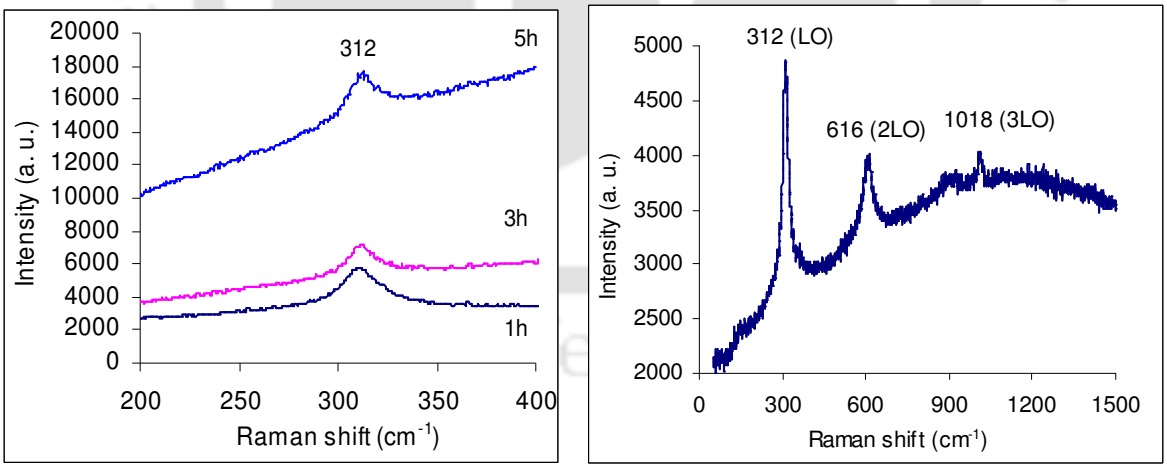

(a) **(b)**

Figure 3.7: Raman spectra of the CdS nanorods powder samples (a) prepared for three different reaction times in the range of 200-400 cm^{-1} and (b) prepared for 1h in the range of 50-1500 cm^{-1}.

Figure 3.7 show the Raman spectra of the CdS nanorods powder samples prepared for three different reaction times at excitation wavelength of 488 nm of Ar ion laser. The Raman spectra consist of a single fundamental band at approximately 312 cm^{-1} for all the samples (Figure 3.7a) and can be assigned to the longitudinal optical phonon (LO) [3.20]. The spectra also display a broad luminescence that is more pronounced in samples with increasing diameter of nanorods. Raman spectrum of the samples prepared for 1 h (Figure 3.7b) is dominated by overtones of the longitudinal optical phonon. There are three clearly discernible LO modes at 312, 616 and 1018 cm^{-1} respectively, in the range of 50-1500 cm^{-1}. Similar Raman scattering phenomenon has been observed for ordered macro porous CdS and for the CdS nanowires deposited in anodic aluminum oxide nanotemplate [3.20].

c) Thermal Stability Studies

Thermal stability studies of these CdS nanostructured powder samples are performed by thermo gravimetric analysis (TGA), simultaneous differential thermal analysis (SDTA) and derivative thermo gravimetry (DTG). These results are presented in Figure 3.8. From Figure 3.8a, it is observed that for 1 h sample, the weight is gradually decreased with increase of temperature which could be due to the poor crystallinity of the CdS nanorods, which is also consistent with the XRD and SEM results. No weight loss of material up to 650 °C for samples prepared for 3 h and 5 h reaction time suggests that these synthesized CdS nanocomposites are fully dried and stable up to 650 °C. For all these three samples about 24% and 34% weight loss is observed from 650-786 °C and 786-950 °C respectively. The reason for these weight losses are not very clear as melting point of the bulk CdS is 1475 °C. The observed weight loss in these samples could be due to the large number of broken bonds owing to very high surface to volume ratio, which may rearrange them at comparatively lower temperature and also due to the evaporation of sulfur from the broken CdS bonds.

The SDTA of these CdS powder samples are also investigated. It is observed that the particle size of the nanostructured materials influences the SDTA results [3.21]. The smaller the particle size, the larger is the exothermic peak area of the SDTA curve because the decomposition of a sample with a large particle size is slower than that of a sample with a large specific surface area [3.22]. The observed peak areas of the SDTA curves of the CdS nanocomposites (Figure 3.8b) are also very broad, which indicate that the size of the particles is very small.

Kinetic information like thermal activation energy (E), Arrhenius parameter (A) and entropy of activation (ΔS) of the CdS nanorods powder samples prepared for three different reaction times are also obtained by Coats-Redfern and Freeman-Carroll methods (Figure 3.9, Chapter 2, subsection 2.4.3) and the results are summarized in Table 3.3. For Coats-Redfern model, the best fits are obtained for $g(\alpha) = [-\ln (1-\alpha)] = kt$, where k is the Boltzmann's constant and t is the time. This relation corresponds to random nucleation with one nucleus on each particle. It is observed that in both kinetic methods, thermal activation energy increases with the increase of reaction time which suggest that thermal stability of these powder samples also increases with the increase of reaction times.

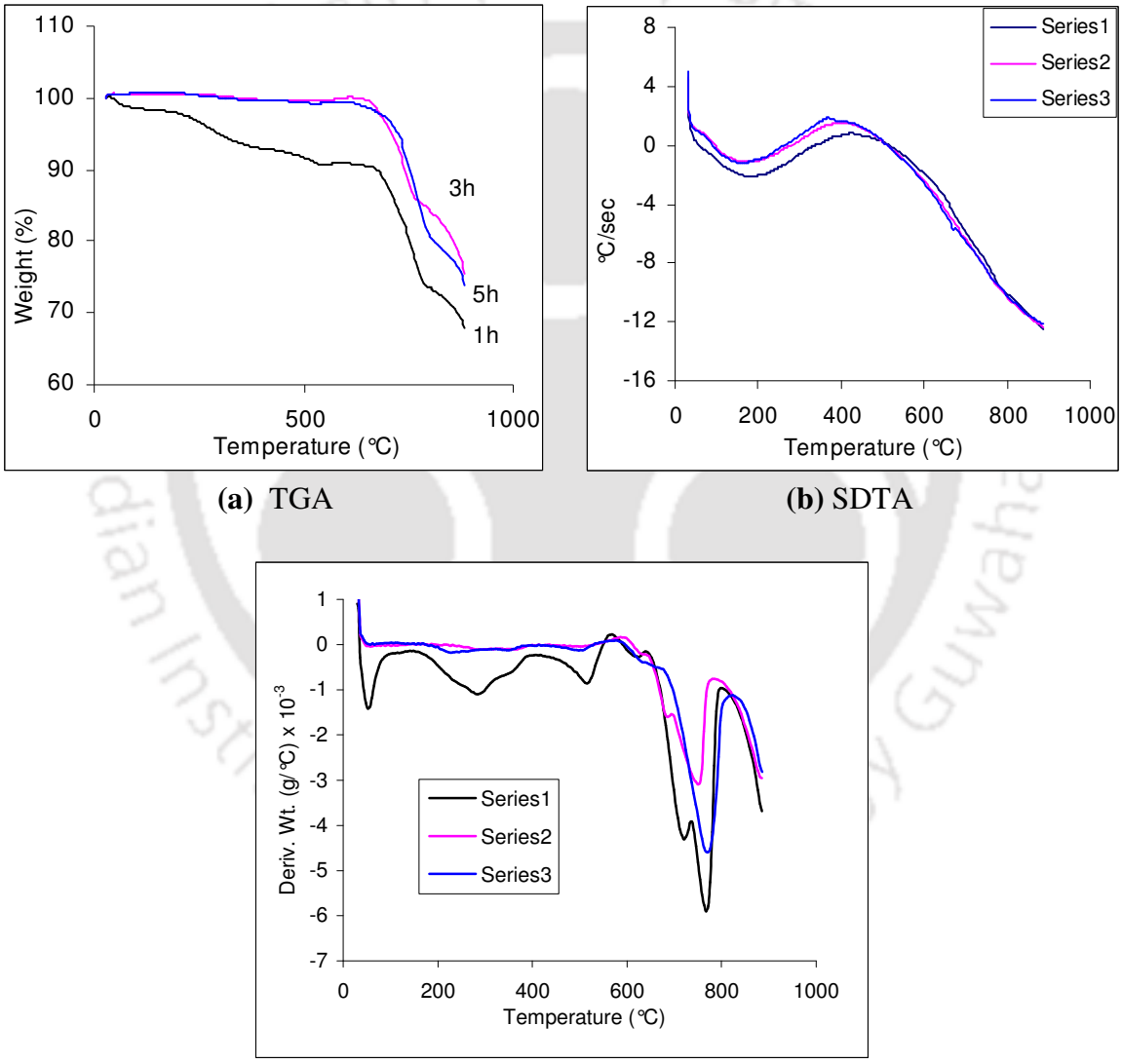

(a) TGA **(b)** SDTA

(c) DTG

Figure 3.8: (a) TGA, (b) SDTA and (c) DTG curves of CdS nanorods powder samples prepared for three different reaction times. Here Series1, Series2 and Series3 represent the CdS 1 h, 3 h and 5 h samples respectively.

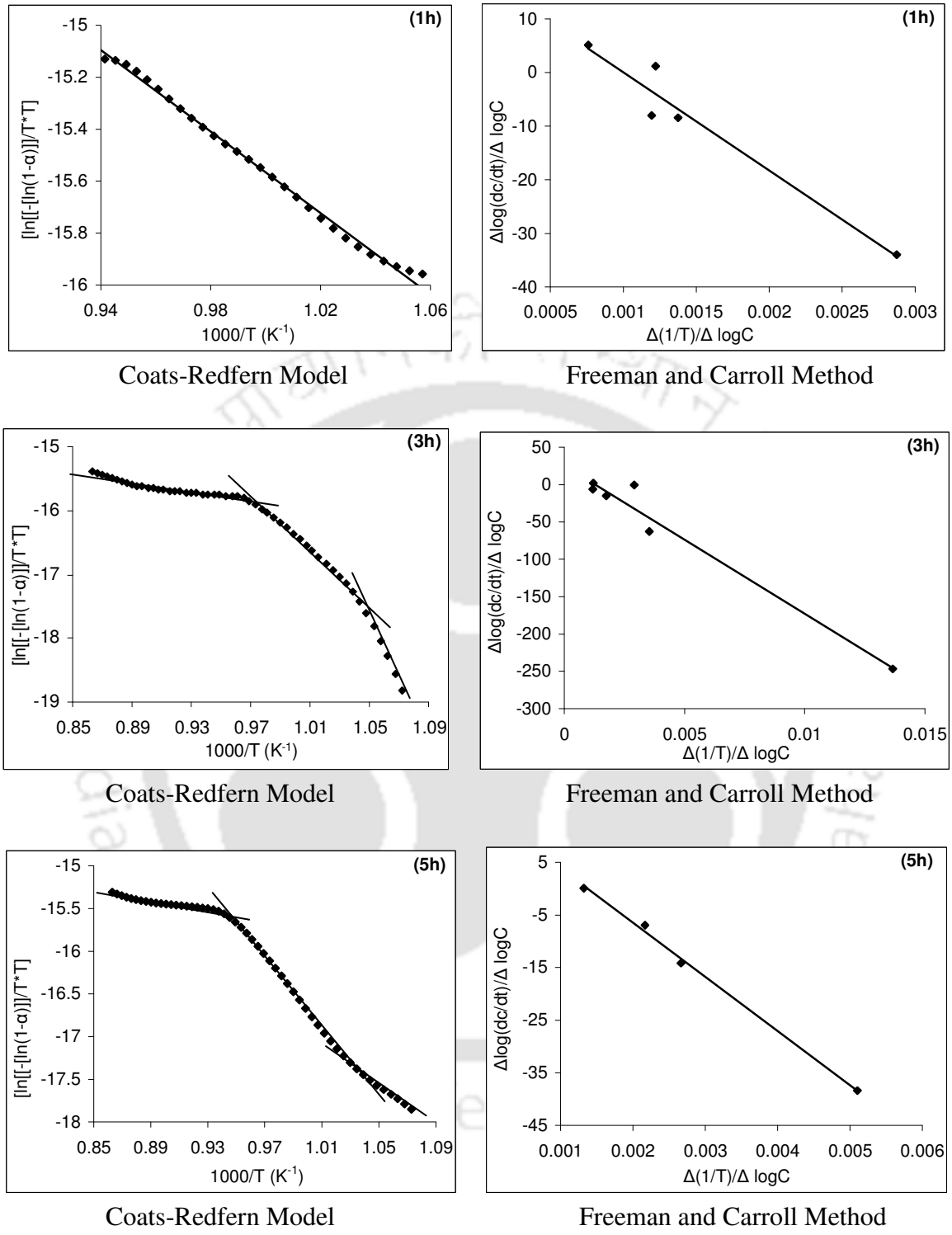

Figure 3.9: Determination of kinetic parameters of CdS nanorods powder samples obtained by Coats-Redfern and Freeman and Carroll Methods.

Table 3.3: Kinetic parameters of the CdS nanorods powder samples obtained by different kinetic models

Sample	Methods			
	Coats-Redfern			Freeman and Carroll
	Activation energy E (kJ/mol)	Arrhenius parameters A (s^{-1})	Entropy ΔS (J/degree/mol)	Activation energy E (kJ/mol)
CdS-1h	63	2613	-187	196
CdS-3h	155	8279	-177	351
CdS-5h	201	2874	-167	380

d) Electrical Transport Studies

Electrical transport studies on the CdS nanorods thin films in the temperature range (303-463 K) show the thermally activated behavior for both dark and photoconductivity (σ_d and σ_L respectively). From Figure 3.10 it is observed that both dark and photoconductivity of the CdS nanorods prepared for three different reaction times are thermally activated with single activation energy in the entire temperature range. The activation energy (E_a) for photoconductivity is 0.16, 0.05 and 0.19 eV for 1 h, 3 h and 5 h respectively for illumination intensity of 10 mW/cm^2. The activation energy (E_a) for dark conductivity is 0.39, 0.26 and 0.83 eV for 1 h, 3 h and 5 h respectively. At room temperature, the dark conductivity is about ~10^{-11}, 10^{-9} and 10^{-4} Ω^{-1} cm^{-1} whereas the photoconductivity is ~10^{-6}, 10^{-4} and 10^{0} Ω^{-1} cm^{-1} for 1 h, 3 h and 5 h samples respectively. Both dark and photoconductivity of the CdS nanorods thin films are increased (~7 order of magnitude) with the increase of reaction times as crystallinity is increased. Dark and photoconductivity of bulk CdS thin films [3.23] are reported of the order of 10^{-5} and 10^{-2} Ω^{-1} cm^{-1} respectively. It is observed that both dark and photoconductivity of the CdS nanorods prepared for 5 h reaction time are higher than the bulk CdS.

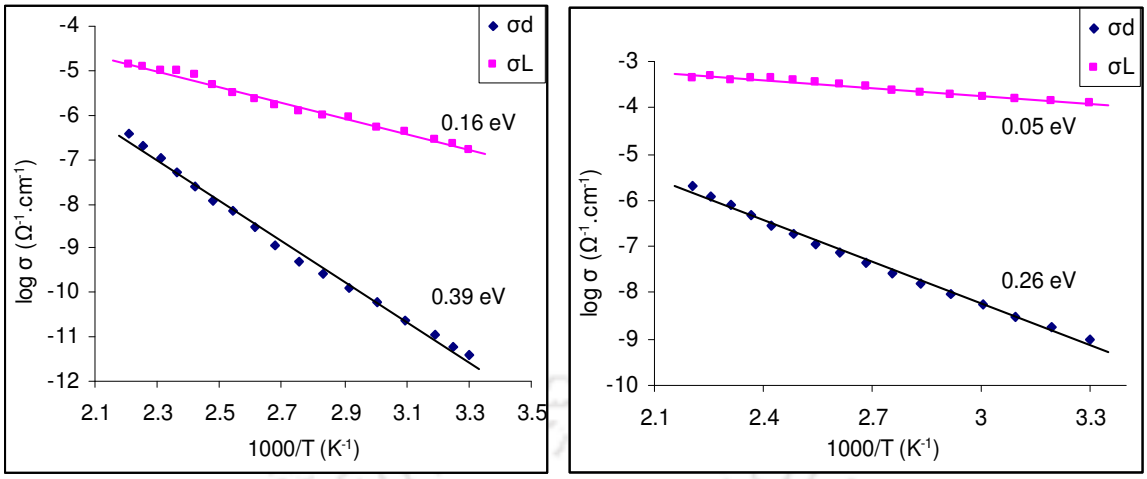

(a) CdS-1h **(b)** CdS-3h

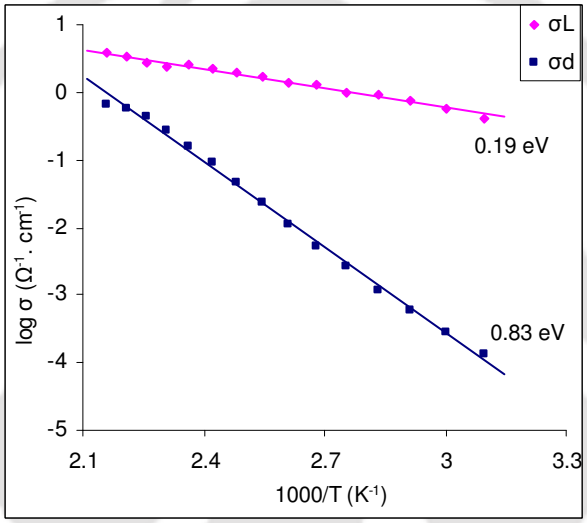

(c) CdS-5h

Figure 3.10: Dark and photoconductivity of the CdS nanorods thin films prepared for three different reaction times.

The photosensitivity ($S=\sigma_L/\sigma_{d,}$) varies from $4x10^4$ at 300 K to 36 at 463 K for 1 h sample, 10^5 at 300 K to 134 at 463 K for 3 h sample and 10^3 at 300 K to 5.76 at 463 K for 5 h sample respectively for the given intensity of light (10 mW/cm^2). The values of S at various temperatures for CdS nanorods thin film prepared for three reaction times are summarized in Table 3.4.

Table 3.4: Photosensitivity of the CdS nanorods thin films at various temperatures (light intensity=10 mW/cm^2). The exponent γ for intensity dependence of photocurrent is also given.

CdS-1h

Temp. (K)	σ_L (Ω^{-1} cm^{-1})	σ_d (Ω^{-1} cm^{-1})	σ_L/σ_d	γ
323	1.03×10^{-6}	9.37×10^{-11}	1.1×10^{4}	0.66
343	2.12×10^{-6}	3.02×10^{-10}	7.02×10^{4}	0.74
363	3.00×10^{-6}	1.20×10^{-9}	2.5×10^{3}	0.89
383	5.72×10^{-6}	7.40×10^{-9}	7.69×10^{2}	0.84

CdS-3h

Temp. (K)	σ_L (Ω^{-1} cm^{-1})	σ_d (Ω^{-1} cm^{-1})	σ_L/σ_d	γ
323	1.63×10^{-4}	4.29×10^{-9}	3.8×10^{4}	0.87
343	1.87×10^{-4}	1.16×10^{-8}	1.62×10^{4}	0.87
363	2.45×10^{-4}	2.81×10^{-8}	8.72×10^{3}	0.72
383	3.06×10^{-4}	7.33×10^{-8}	4.17×10^{3}	0.75

CdS-5h

Temp. (K)	σ_L (Ω^{-1} cm^{-1})	σ_d (Ω^{-1} cm^{-1})	σ_L/σ_d	γ
323	4.20×10^{-1}	1.33×10^{-4}	$3.16\times10^{+3}$	0.48
343	7.35×10^{-1}	5.88×10^{-4}	$1.25\times10^{+3}$	0.58
363	1.02×10^{0}	2.61×10^{-3}	$3.91\times10^{+2}$	0.59
383	1.39×10^{0}	1.13×10^{-2}	$1.23\times10^{+2}$	0.62

Further photoconductivity σ_{ph} ($=\sigma_L - \sigma_d$) follows a power law ($\sigma_{ph} = F^{\gamma}$) dependence on intensity of light with γ varying from 0.66 to 0.89 for 1 h sample, 0.72 to 0.87 for 3 h sample and 0.48 to 0.62 for 5 h sample in temperature range of measurements (Figure 3.11). Here σ_{ph} is obtained after subtracting dark current from the total measured current in presence of light.

The value of exponent γ indicates that monomolecular recombination take place in case of 1 h and 3 h samples and bimolecular recombination take place in case of 5 h sample.

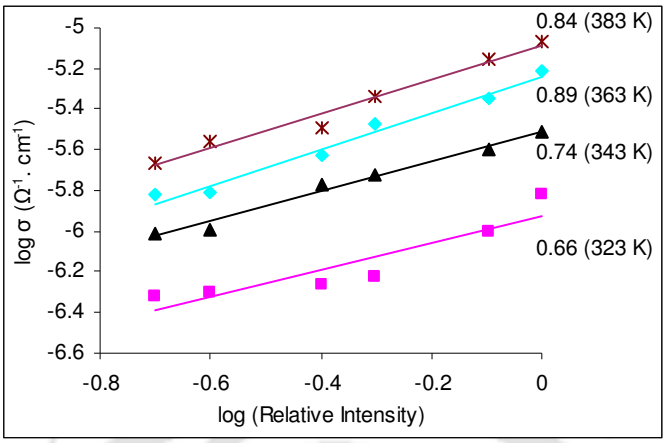

(a) CdS-1h

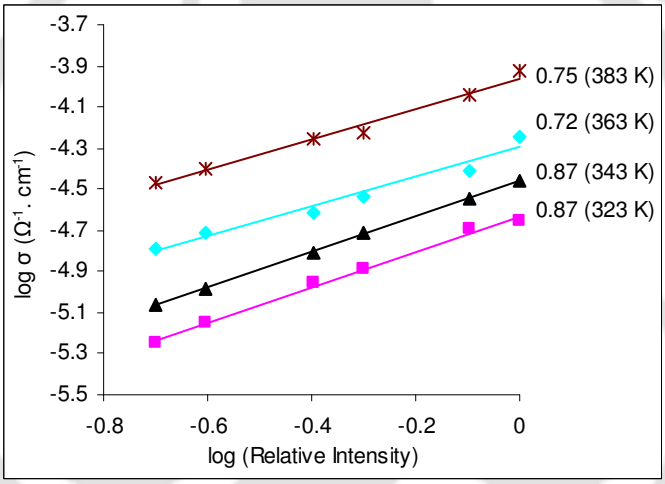

(b) CdS-3h

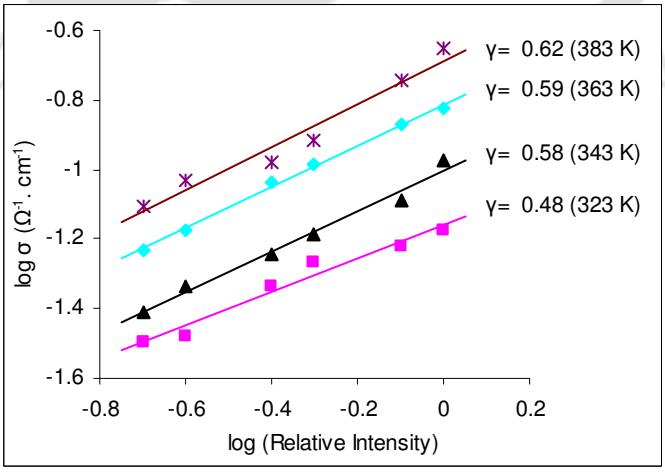

(c) CdS-5h

Figure 3.11: Intensity variation of photoconductivity of CdS nanorods prepared for three different reaction times.

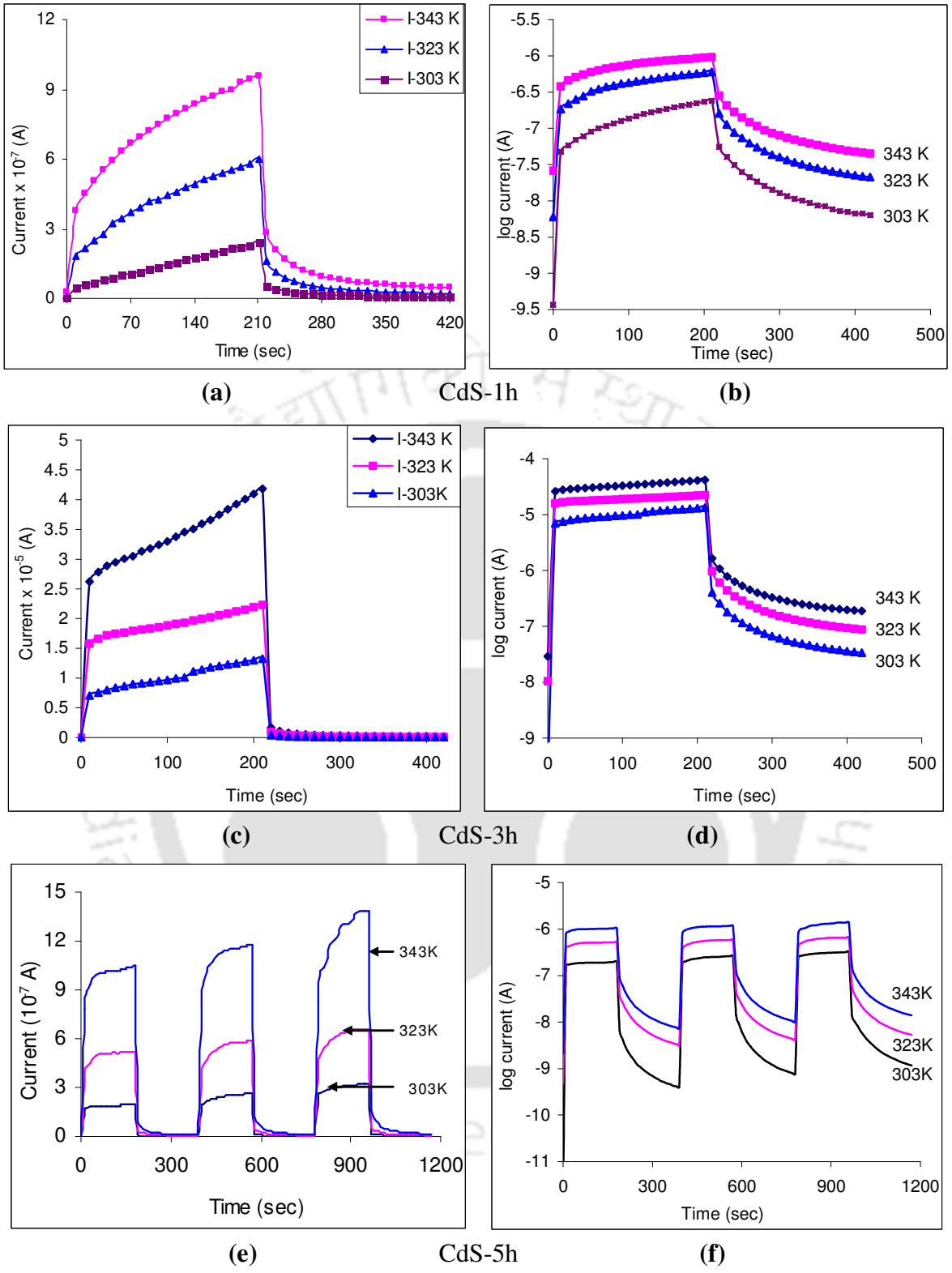

Figure 3.12: (a, c, e) Rise and decay of photocurrents of CdS nanorods thin films at 343, 323 and 303 K respectively; (b, d, f) re-plot of (a, c, e) in logarithmic scale for clarity of the decay behavior.

Figure 3.12 show the rise and decay of photocurrent of the CdS nanorods thin films with time at different temperatures (303, 323, 343 and 363 K). It is clear from Figure 3.12 that, photocurrent rises with time at all temperatures. After switching off the light, the current does not fall to dark value instantaneously but decreases slowly and stays at a higher value. The decay of photocurrent seems to involve two process; fast process in the beginning followed by a slow decay at a later time. There is always a persistent photocurrent at all temperatures which do not go to zero even for a long time after the light pulse is cut off. During each subsequent light exposure, the photocurrent is larger than earlier and the PPC is larger than the previous value.

The slow rise and decay of the photocurrent is not uncommon for semiconductor and other disordered materials and has been ascribed to the presence of traps [3.24, 3.25] in the energy gap as well as due to the local potential fluctuation [3.26] arising from structural and charge inhomogeneities causing the band bending and potential barrier [3.27, 3.28], which control the trapping and recombination processes. Shallow traps are responsible for the faster process where as the deep traps and potential fluctuations cause slow increase and decrease of photoconductivity. Joshi has reported a slow rise of the photocurrent for CdS detectors and observed that the rise of photocurrent has three components having different time constants, corresponding to transitions involving conduction band and the shallow states associated with it, for a trap with negligible delay and a trap dominated process with a larger delays contribution [3.29]. The excess conductivity after turning the light off and its slow decay has also been reported for a variety of materials including polycrystalline CdS, ZnCdSe and CdSSe alloys [3.30-3.32], AlGaAs, a-InSe alloys [3.33, 3.34], amorphous silicon superlattices [3.35], microcrystalline silicon films [3.36] and porous silicon layers [3.37]. All these films show a slow decay, often a non exponential decay of photocurrent (PC) with a large time constant. The non exponential decay is either a sum of several exponentially decaying terms, or of a stretched exponential type. The former is due to the parallel relaxation process caused by a distribution of trapping centers having different depths and cross sections, each relaxing independently with a different time constant, whereas the later is due to a non uniform distribution of trapping and recombination centers with decreasing probability of recombination as the time passes.

In case of a set of discrete traps levels with different cross section associated with it decay of current $I_f(t)$ is given by the equation:

$$I_f(t) = \sum_{i=1}^{n} A_{fi}.\exp(-t/\tau_{di}) \qquad (3)$$

where I_f is the steady-state photocurrent and A_f, τ_d are the amplitude and time-constant for the decay process respectively, n is the number of the exponential components involved. In the present case of CdS nanorods thin film, the decay of photocurrent could be well fitted to two exponential components, a fast component in the beginning and a slow one afterwards with very different values of decay time constants. It seems to follow the relation

$$I_f(t) = I_1 e^{-\frac{t}{\tau_1}} + I_2 e^{-\frac{t}{\tau_2}} \qquad (4)$$

where I_1, I_2 are the pre-exponential factors and τ_1, τ_2 are decay time constants for fast and slow parts respectively. The values of τ_1 and τ_2 are obtained by fitting the observed behavior from equation (4). The fast decay in the beginning is about 30 times faster than the slow counterpart. The values of τ_1, τ_2 at different temperatures are listed in Table 3.5. We also tried to fit the stretched exponential time dependence to the decay of PPC, but the fitting has not been good at all. This suggests that in our case, there are at least two discrete levels responsible for the slow decay of PPC. There could be one more, very fast decay corresponding to the band to band recombination, which is instantaneous and could not be measured.

Several models have been proposed to understand the origin of PPC in semiconductors. The PPC is believed to be either due to the presence of random local potential fluctuations arising due to the compositional inhomogeneities causing the photo generated electron hole pair to spatially separate before these recombine or due to the presence of deep lying traps (DX centers) which capture the electrons and reemit slowly resulting in the excess conductivity even after the light pulse is cut off.

Our results are well explained by existing models. We observe a large PPC in our case even after a few hundred seconds of cutting off the light and after each successive exposure of light, both PC as well PPC increases, whereas the relaxation times (τ_1 and τ_2) remain essentially unchanged. The large value of PPC, even after 200 sec of cutting the light, suggests the presence of random local potential fluctuations or deep lying traps to be the cause of the PPC. The presence of deep lying traps are not expected to be responsible for the observed PPC in our case as in that case, the relaxations times are expected to be thermally activated and decrease with increase in temperature, the activation energy being

corresponding to the barrier potential. On the other hand, in our case, we observed a slight increase in relaxation times (both τ_1 and τ_2) which could be explained in terms of local potential fluctuations as discussed later.

Table 3.5: PPC and its decay time constants for the CdS nanorods thin films. τ_1 and τ_2 correspond to initial fast and later slow decay respectively

CdS-1h

Temp (K)	I_{dark} (A)	PC after 180 sec of light illumination (A)	PPC after 200 sec of light off (A)	τ_1 (sec)	τ_2 (sec)
303	3.70×10^{-10}	2.13×10^{-7}	6.66×10^{-9}	4.4±0.3	86±6
323	5.97×10^{-9}	5.56×10^{-7}	2.19×10^{-8}	4.9±0.3	101±7
343	2.60×10^{-8}	9.00×10^{-7}	4.64×10^{-8}	5.2±0.3	113±8

CdS-3h

Temp (K)	I_{dark} (A)	PC after 180 sec of light illumination (A)	PPC after 200 sec of light off (A)	τ_1 (sec)	τ_2 (sec)
303	1.49×10^{-10}	1.25×10^{-5}	3.49×10^{-8}	2.3±0.08	68±6
323	1.04×10^{-8}	2.12×10^{-5}	9.04×10^{-8}	2.5±0.09	74±6.5
343	2.93×10^{-8}	3.92×10^{-5}	1.92×10^{-7}	2.4±0.09	86±8

CdS-5h

Temp (K)	I_{dark} (A)	PC after 180 sec of light illumination (A)	PPC after 200 sec of light off (A)	τ_1 (sec)	τ_2 (sec)
303	1.52×10^{-12}	2.0×10^{-7}	4.18×10^{-10}	2.3±0.1	89±0.2
323	4.85×10^{-10}	5.2×10^{-7}	3.37×10^{-9}	2.9±0.1	105±0.2
343	2.09×10^{-9}	1.05×10^{-6}	7.62×10^{-9}	3.2±0.1	110±0.2

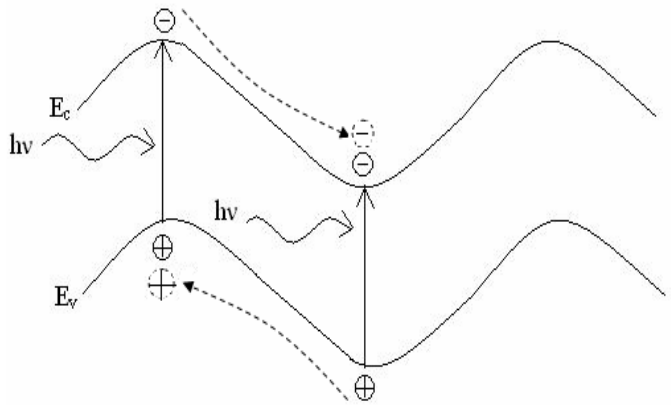

Figure 3.13: Barrier model to explain the persistent photocurrent (PPC) behavior in CdS nanorods thin films.

In our case, the films have no compositional fluctuation unlike the case of ZnCdSe [3.31], CdSSe [3.32]. The SEM results show homogeneous films, with uniformly distributed grains without any pin hole, the EDS data reveals films to have uniform composition. The cause of potential fluctuations thus could be band bending at the grain boundaries which result in the separation of charges before these recombine. Figure 3.13 shows a schematic model to understand the results. When the light is shone, the photogenerated carriers are generated uniformly in the films. Some of these photogenerated carriers recombine instantaneously, whereas some others separate due to band bending as shown in Figure 3.13. Thus the electrons and holes accumulate at spatially different regions in the corresponding local potential minima, which could be grain boundaries regions and a large PPC with slow decay is observed. Local photocurrent measurements on polycrystalline CdS films [3.38] also suggest two parallel photoconduction routes, where first is excited in the crystallites and takes place via grains and the other is excited in the grain boundaries and takes place along the network of these boundaries. The local photocurrents both in the crystallites as well as at the grain boundaries exhibit PPC much after the light is turned of in this case also.

A small increase in τ with increase in temperature could also be well explained in terms of the local potential fluctuation as shown in Figure 3.13. With increase, in temperature, the carriers are expected to diffuse faster to the local potential minima and thus show a larger PPC and also an increase in τ. The model could also qualitatively explain the slow increase in PC with time and for each successive illumination, corresponding to more accumulation of carriers at these sites with exposure.

3.3.2 ZnS Nanostructures

a) Structural Properties

Figure 3.14 show the XRD patterns of the ZnS powder samples as well as thin films prepared for three different reaction times. Broad diffraction peaks are observed for ZnS powder samples prepared for 1 h and 3 h respectively, which suggest that particle sizes could be very small. XRD pattern of the ZnS powder samples prepared for 5 h is very sharp, indicating very high crystallinity. These XRD patterns suggest that crystallinity of these nanostructured materials increases with the increase of reaction times. The three diffraction peaks corresponding to the (111), (220), (311) planes of the ZnS prepared for 5 h indicate a zinc-blende crystal structure (JCPDS 05-0566, a = 0.5406 nm). The extra peaks observed for the samples prepared for 1 h and 3 h is due to the residual sulfur with monoclinic structure S_8 [3.39] from the reagent thiourea. The calculated lattice constant of a = 0.5391 nm based on the (111) plane at 2θ = 28.657 is consistent with standard literature value. Average grain size (D), dislocation density (δ), number of crystallites per unit area (N) and the strain (ε) of the ZnS nanostructured prepared for 5 h reaction times are obtained from XRD which are summarized in Table 3.6. For 1 h and 3 h samples average grain size, dislocation density, number of crystallites and the strain are not obtained due to the lack of sharp peaks and the extra peaks originated from residual sulfur.

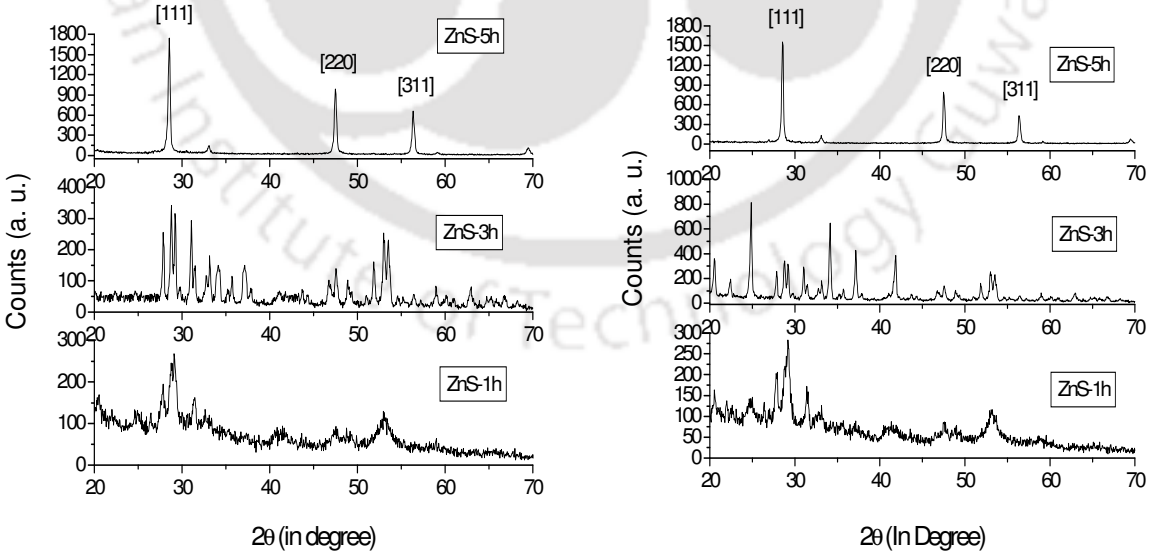

Figure 3.14: XRD patterns of the ZnS powders and thin films prepared for three different reaction times.

Table 3.6: Physical parameters of ZnS nanostructured obtained from XRD data

Sample	Grain size (D) (nm)	Dislocation density (δ) (lines/m^2)	Number of crystallites per unit area (N)	Strain (ε)
ZnS-5h	35	8.65 x 10^{14}	2.04 x 10^{17}	1.03 x 10^{-3}

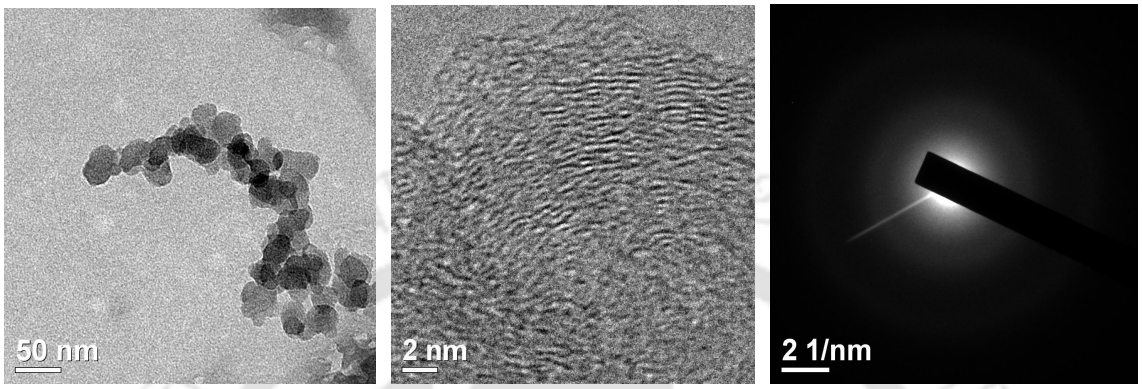

TEM HRTEM SAED

(a) ZnS-1h

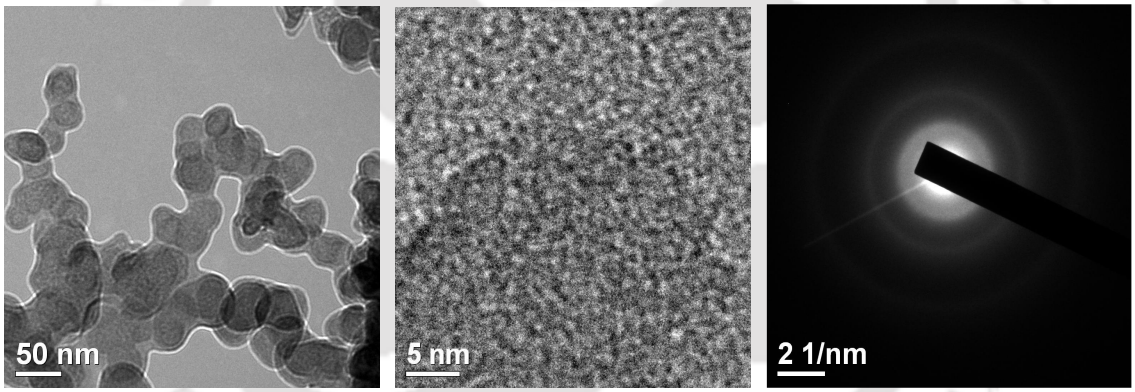

TEM HRTEM SAED

(b) ZnS-3h

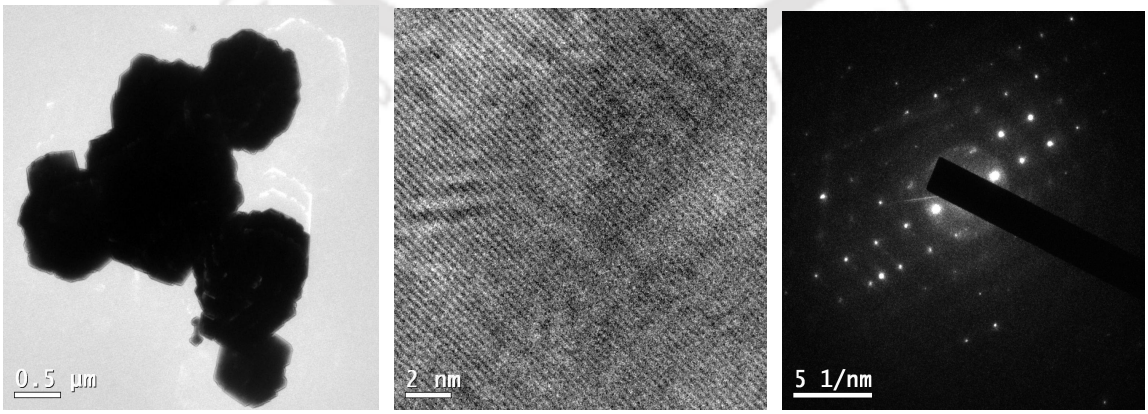

TEM HRTEM SAED

(c) ZnS-5h

Figure 3.15: TEM, HRTEM and SAED patterns of ZnS powder samples prepared for three reaction times.

TEM images (Figure 3.15) show that disk like ZnS nanoparticles are produced during the solvothermal synthesis for all reaction times. Diameter of the ZnS samples prepared for 1 h is less than 50 nm. For 3 h reaction time sizes vary from 50 to 80 nm and for 5 h reaction time sizes vary from 100 nm to several micrometers. SAED patterns of the ZnS powder samples prepared for 1 h and 3 h reveal the amorphous nature whereas ZnS prepared for 5 h is single crystalline in nature. SAED pattern suggest that the crystallinity of this material increases with the increase of reaction times which also support the XRD results. Interplanar spacing of the ZnS powder samples prepared for 5 h is obtained from HRTEM image (Figure 3.15c) as 0.3 nm, which corresponds to plane (111).

SEM images of the ZnS powder samples prepared for three different reaction times are presented in Figure 3.16. Chemical purity and stoichiometric ratios of these ZnS nanostructures are obtained by EDAX. Stoichiometric ratios of the as-synthesized ZnS nanostructures are close to 1:1 and slightly sulfur deficient. These observations are summarized in Table 3.7.

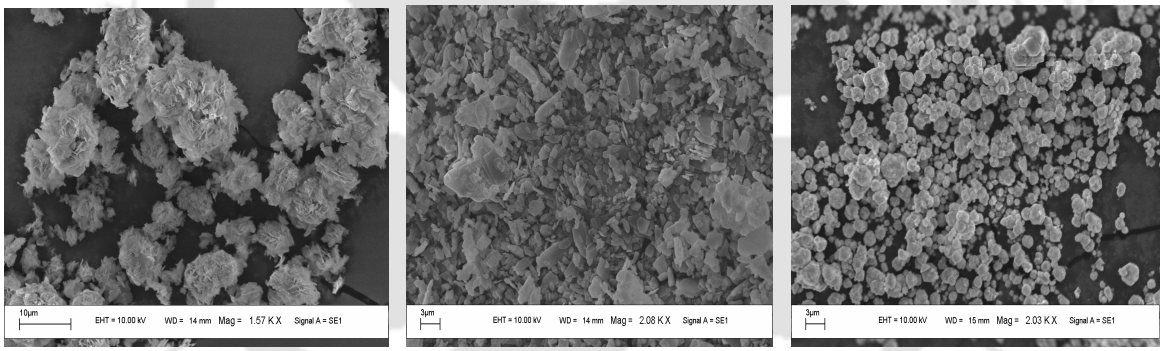

ZnS-1h ZnS-3h ZnS-5h

Figure 3.16: SEM images of the ZnS powder samples prepared for three reaction times.

Table 3.7: The stoichiometric ratio of the as-synthesized ZnS powder samples

Sample	Zn	S
ZnS-1h	51.50	48.50
ZnS-3h	50.72	49.28
ZnS-5h	50.76	49.24

b) Optical Properties

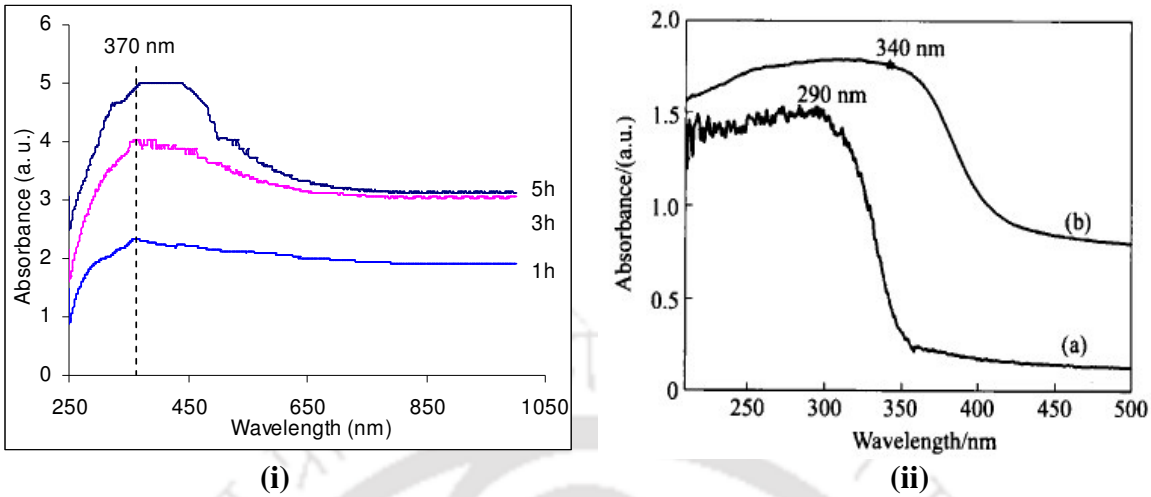

(i) **(ii)**

Figure 3.17: (i) UV-Vis absorption spectra of the ZnS nanostructured thin films prepared for three different reaction times and (ii) UV-vis absorption spectrum of (a) ZnS superstructures; (b) Bulk ZnS powder obtained by Jun-ping et al. [3.40]

Compared to bulk ZnS (340 nm) [3.40], a broad absorption band around 370 nm (corresponding band gap 3.35 eV) is observed for all the ZnS nanostructured thin films prepared for three different reaction times (Figure 3.17). This broad absorption band arises could be due to the surface states of the ZnS nanoparticles because the absorption is lying below the absorption edge of the particles, i.e., the absorption energy is lower than the band gap of the particles.

Photoluminescence (PL) spectra (Figure 3.18) of the ZnS nanostructured thin films are recorded for two different excitation wavelengths (250 nm and 300 nm respectively) at room temperature. A broad emission peak is observed at 363 nm (3.42 eV) for all the samples and two sharp peaks are also observed at 422 nm and 439 nm for excitation wavelength at 250 nm. The broad emission peak at 363 nm for 250 nm of excitation wavelength is slightly blue shifted to 355 nm (3.49 eV) in case of 300 nm of excitation wavelength. The PL studies on bulk ZnS show an emission peak at 350 nm and 395 nm [3.41]. The former peak is assigned to excess Zn^{2+} and S^{2-} whereas the later peak is due to excess Zn in ZnS. In the present studies we do not observe any peak at 395 nm, the peak at 355 and 363 nm could be due to Zn^{2+}, S^{2-} and are slightly red shifted compared to bulk material. The additional peaks observed at 422 and 439 nm could be due to interstitial and vacancy states of sulfur in ZnS as observed for colloidal ZnS nanocrystals [3.42].

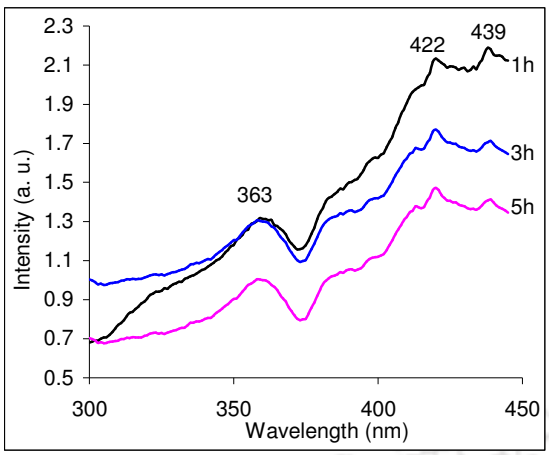

(a) At 250 nm of excitation wavelength

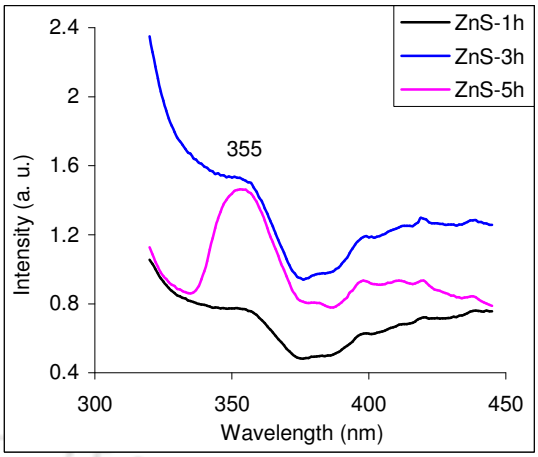

(b) At 300 nm of excitation wavelength

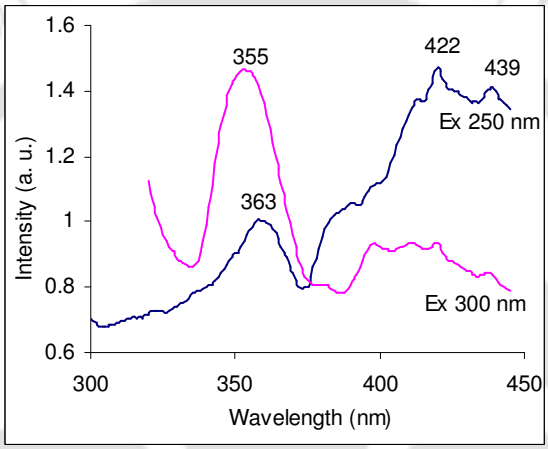

(c)

Figure 3.18: Photoluminescence spectra of the nanostructured ZnS thin films (a) for all samples at 250 nm, (b) at 300 nm of excitation wavelengths and (c) prepared for 5 h at 250 nm and 300 nm of excitation wavelengths.

Figure 3.19 shows the representative Raman spectra of ZnS nanostructured powder samples prepared for 3 h reaction time in the range of 100–400 cm^{-1}. The Raman spectra exhibit strong sharp peaks at 224 and 290 cm^{-1} and few small peaks at 118, 137, 159, 180 and 323 cm^{-1}. Raman spectra of bulk cubic phase of ZnS shows the TO and LO zone center phonons at 276 and 351 cm^{-1} respectively [3.43]. The peaks at 290 cm^{-1} can be assigned to transverse optic (TO) phonons of ZnS nanostructured [3.44]. The Raman peak observed at 323 cm^{-1} can be assigned as the LO mode of cubic ZnS. According to the result of phonon combinations corresponding to different critical points, the other peaks found at 137, 180 and 224 cm^{-1} are respectively assigned to $2TA_L$ (TA, transverse acoustic), $2TA_x$ and $[TO\text{-}TA]_x$ [3.45, 3.15], being in accordance with the second-order Raman spectra [3.46].

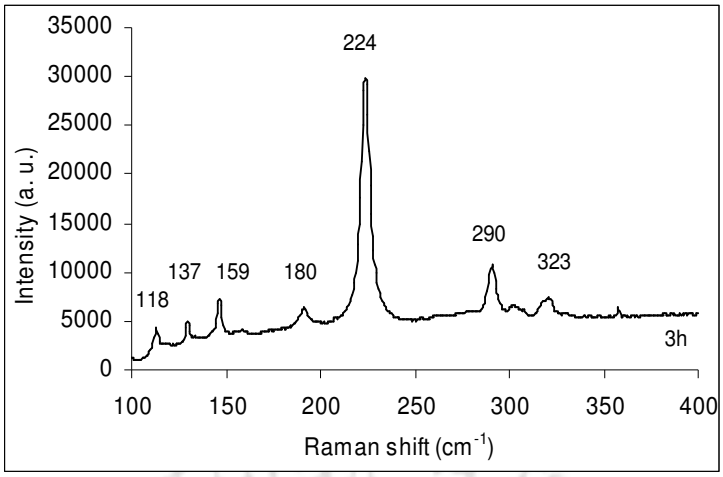

Figure 3.19: Raman spectra of the ZnS nanostructured powder samples prepared for 3 h reaction time.

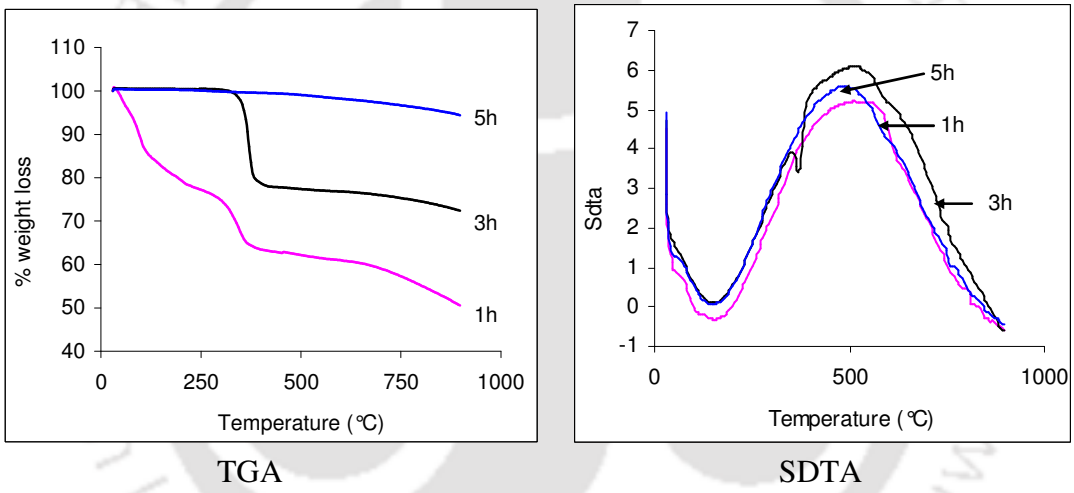

TGA SDTA

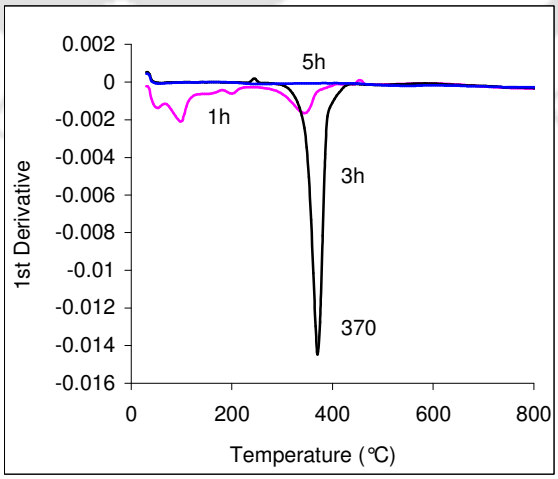

DTG

Figure 3.20: TGA, SDTA and DTG curves of the ZnS powder samples prepared for three different reaction times.

c) Thermal Stability Studies

In order to study the stability of ZnS nanoparticles at temperature range 25-900 °C, TG–DTG measurement on the samples are carried out. From Figure 3.20 the TG–DTG show that weight is gradually decreased with the increase of temperature for 1 h sample which could be due to the very low crystallinity of the sample and 50% weight loss is observed after 900 °C. In case of 2 h sample it is observed that the samples are stable up to 400 °C and then gradually decreased with temperature and 25% weight loss is observed after 900 °C. As-synthesized ZnS powder samples prepared for 5 h is almost stable up to 900 °C and only 6% weight loss is observed through out this temperature range. From these TG-DTG results it is clear that the crystallinity is increased with increase of reaction times which is also consistent with the XRD, SEM and TEM results.

d) Electrical Transport Studies

The I-V characteristics (Figure 3.21a) of the ZnS nanostructured thin films are measured to study the metal-semiconductor junctions. It is observed that I-V curve is nearly a straight line and goes through the origin, which suggests that metal-semiconductor junctions are ohmic in nature.

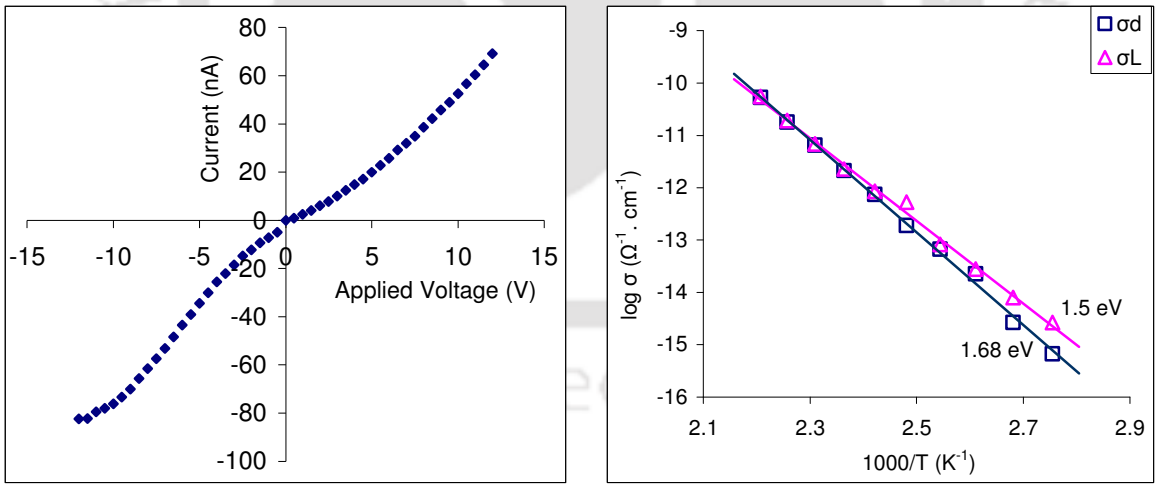

(a) **(b)**

Figure 3.21: (a) I-V characteristic and (b) dark (σ_d) and photoconductivity (σ_L) studies on ZnS nanostructures prepared for 5 h.

Dark (σ_d) and photoconductivity (σ_L) of these nanostructured ZnS thin films prepared for three different reaction times are also measured. ZnS thin films prepared for 5 h show a

thermally activated behavior in the temperature range of 303-453 K with single activation energy in the entire temperature range. In Figure 3.21b we present the dark and photoconductivity of the ZnS thin films prepared for 5 h reaction time. The dark conductivity is of the same order as for bulk samples [3.47]. The thermal activation energy for the dark and photoconductivity is calculated as 1.68 and 1.5 eV respectively for illumination intensity of 10 mW/cm^2. The dark activation energy is nearly half of the band gap energy (close to the Fermi level), which suggests that ZnS prepared for 5 h is intrinsic in nature. We don't get any dark and photoconductivity for ZnS 1 h and 3 h samples which could be due to the high resistivity of these samples.

3.4 Conclusions

CdS and ZnS nanostructures are successfully synthesized by solvothermal process with three different reaction times and the crystallinity of these samples increased with increase of reaction times. CdS and ZnS nanostructured thin films are also prepared successfully by doctor blade technique and films are stable up to 473 K. CdS and ZnS nanostructures also show good optical and high thermal stability. From photoluminescence study of the CdS and ZnS thin films few sharp peaks are observed. These are explained by optical transitions involving Cd^{2+}, Zn^{2+} and S^{2-} states and interstitial and vacancy states of sulfur in CdS and ZnS nanostructured. CdS and ZnS films also show thermally activated conductivity and good photosensitivity. The observed PPC and its slow decay with time in case of CdS nanostructured thin films are believed to be due to the presence of potential fluctuations in the films. I-V characteristics of these films confirm the ohmic behaviour of the metal-semiconductor junctions.

3.5 References

[3.1] S. H. Yu, Y. S. Wu, J. Yang, Z. H. Han, Y. Xie, Y. T. Qian and X. M. Liu, Chem. Mater. **10**, 2309 (1998).

[3.2] L. E. Brus, J. Chem. Phys. **80**, 4464 (1984).

[3.3] L. P. Deshmukh, S. G. Holikatli and P. P. Hankare, J. Phys. D: Appl. Phys. **27**, 1786 (1994).

[3.4] P. K. Khanna and V. V. V. S. Subbarao, Mater. Lett. **58**, 2801 (2004).

[3.5] L. E. Brus, Appl. Phys. A **53**, 465 (1991).

[3.6] M. L. Steigerwald and L. E. Brus, Annu. Rev. Mater. Sci. **19**, 471 (1998).

[3.7] V. L. Colvin, M. C. Schlamp and A. P. Alivisatos, Nature **370**, 354 (1994).

[3.8] X. C. Wu and Y. R. Tao, J. Cryst. Growth **242**, 309 (2002).

[3.9] S. H. Deulkar, C. H. Bhosale and M. Sharon, J. Phys. Chem. Solids **65**, 1879 (2004).

[3.10] M. Leskela, J. Alloys Compd. **275–277**, 702 (1998).

[3.11] J. Vidal, O. de Melo, O. Vigil, N. Lopez, G. Contreras-Puente and O. Zelaya-Angel, Thin Solid Films **419**, 118 (2002).

[3.12] T. L Chu, S. S. Chu, J. Brittand, C. Ferekides and C. Q. Wu, in: Proceedings of the 22nd IEEE Photovoltaic Specialists Conference, USA, pp. 1136 (1991).

[3.13] A. Morales-Acevedo, Sol. Energy Mater. Sol. Cells **90**, 2213 (2006).

[3.14] J. Yang, J. H. Zeng, S. H. Yu, L. Yang, G. Zhou, and Y. Qian, Chem. Mater. **12**, 3259 (2000).

[3.15] C. Cheng, G. Xu, H. Zhang, J. Cao, P. Jiao and X. Wang, Mater. Lett. **60**, 3561 (2006).

[3.16] Y. Li, H. Liao, Y. Ding, Y. Fan, Y. Zhang and Y. Qian, Inorg. Chem. **38**, 1382 (1999).

[3.17] B. Liu, G. Q. Xu, L. M. Gan, C. H. Chew, W. S. Li and Z. X. Shen, J. Appl. Phys. **89**, 1059 (2001).

[3.18] G. Q. Xu, B. Liu, S. J. Xu, C. H. Chew, S. J. Chua and L. M. Gana, J. Phys. Chem. Solids **61**, 829 (2000).

[3.19] D. E. Moore and K. Patel, Langmuir **17**, 2541 (2001).

[3.20] J. S. Suh and J. S. Lee, Chem. Phys. Lett. **281**, 384 (1997).

[3.21] G. S. Paul, P. Gogoi and P. Agarwal, J. Non-Cryst. Solids **354**, 2195 (2008).

[3.22] T. Hatakeyama and Z. Liu, *Handbook of Thermal Analysis*, John Wiley & Sons, England (1998).

[3.23] G. Y. Chung, H. D. Kim, B. T. Ahn and H. B. Im, Thin Solid Films **232**, 28 (1993).

[3.24] D. V. Lang and R. A. Logan, Phys. Rev. Lett. **39**, 635 (1977).

[3.25] D. V. Lang, R. A. Logan and M. Joros, Phys. Rev. B **19**, 1015 (1979).

[3.26] M. K. Sheinkman and A. Ya. Shik, Fiz. Tekh. Poluprovodn. **10**, 209 (1976) [Sov. Phys. Semicond. **10**, 128 (1976)].

[3.27] H. J. Queisser and D. E. Theodorou, Phys. Rev. B **33**, 4027 (1986).

[3.28] H. J. Queisser, Phys. Rev. Lett. **54**, 234 (1985).

[3.29] N. V. Joshi and A. Serfaty, J. Phys. Chem. Solids **52**, 927 (1991).

[3.30] J. W. Orton, B. J. Goldsmith, J. A. Chapman and M. J. Powell, J. Appl. Phys. **53**, 1602 (1982).

[3.31] J. Y. Lin and H. X. Jiang, Phys. Rev. B **41**, 5178 (1990).

[3.32] A. S. Dissanayake, S. X. Huang and H. X. Jiang, Phys. Rev. B **44**, 13343 (1991).

[3.33] H. X. Jiang and J. Y. Lin, Phys. Rev. Lett. **64**, 2547 (1990).

[3.34] A. S. Maan, D. R. Goyal and A. Kumar, J. Non-Cryst. Solids **110**, 53 (1989).

[3.35] S. C. Agarwal and S. Guha, J. Non-Cryst. Solids **77-78**, 1097 (1985).

[3.36] I. Balberg, Y. Dover, R. Naides, J. P. Conde and V. Chu, Phys. Rev. B **69**, 035203 (2004).

[3.37] Md. N. Islam, P. S. Dobal, H. D. Bist and S. Kumar, Solid State Commun. **107**, 43 (1998).

[3.38] D. Azulay, O. Millo, S. Silbert, I. Balberg and N. Naghavi, Appl. Phys. Lett. **86**, 212102 (2005).

[3.39] X. Liu, J. Cui, L. Zhang, W. Yu, F. Guo and Y. Qian, Mater. Lett. **60**, 2465 (2006).

[3.40] L. Jun-ping, X. Yao, Z. Ning**,** W. Wei, W. Dong and S. Yu-han, Trans. Nonferrous Met. Soc. China **16**, s365 (2006).

[3.41] I. Uchida, J. Phys. Soc. Jpn. **19**, 670 (1964).

[3.42] D. Denzler, M. Olschewski and K. Sattler, J. Appl. Phys. **84**, 2841 (1998).

[3.43] O. Brafman and S. S. Mitra, Phys. Rev. **171**, 931 (1968).

[3.44] J. Schneider and R. D. Kirby, Phys. Rev. B **6**, 1290 (1972).

[3.45] J. Serrano, A. Cantarero, M. Cardona, N. Garro, R. Lauck, R. E. Tallman, T. M. Ritter and B. A. Weinstein, Phys. Rev. B **69**, 014301 (2004).

[3.46] D. L. Rousseau, R. P. Bauman and S. P. S. Porto, J. Raman Spectrosc. **10**, 253 (1981).

[3.47] E. Birringuier, Phil. Mag. B **75**, 209 (1997).

CHAPTER-4

Synthesis and Studies of IV-VI Nanostructured Semiconductors

CHAPTER 4: Synthesis and Studies of IV-VI Nanostructured Semiconductors

4.1 Introduction

Among the IV-VI compound semiconductors, tin sulfide (SnS) and lead sulfide (PbS) compounds have recently attracted considerable attention because of their physical properties, which are suitable for optoelectronic device fabrication. The SnS materials have a great potential for photovoltaic applications as absorber material, due to its band gap of nearly 1.3 eV [4.1]. Intrinsic SnS compound is a p-type semiconductor [4.2] with an electrical resistivity of 32.9 Ω cm, and an absorption coefficient (α) greater than 10^4 cm^{-1} [4.3]. The carrier density is of the order of ~10^{15} cm^{-3}, and the Hall mobility of 139 cm^2/Vs [4.3]. Its electrical properties can be modified by doping it with elements like Ag, Al, N, and Cl [4.4–4.6]. Thin films of SnS have shown a conversion efficiency in photovoltaic devices similar to the one found for silicon films (theoretically up to 25%) [4.7, 4.8]. In addition, by using tin sulfide compounds in photovoltaic structures would decrease the production costs of solar cells, because the materials involved are cheap, nonstrategic, and abundant in nature. On the other hand, PbS exhibits properties which are unusual and unique among semiconductors. For example, it possesses a high dielectric constant (ε_0~170), high mobility, and a positive temperature coefficient of the fundamental band gap E_0 [4.9]. Because of its narrow band gap energy (E_0=0.41 eV at 300 K and 0.286 eV at 4.2 K) [4.9], PbS is useful for long-wavelength detectors, diode lasers and as a photovoltaic materials in inorganic and hybrid solar cells [4.10-4.12].

Because of the increasing interest in nanostructures of materials in device applications, it is necessary to extensively study the various physical properties of these structures in detail. Though, there are a few reports in literature, the reported data indicates that the physical characteristics like optical, thermal and electrical properties of these materials have not been studied extensively in relation to their photovoltaic application. In this thesis work I have prepared SnS and PbS nanostructures by solvothermal process for three different reaction times and studied their different structural, optical, thermal and electrical properties. SnS and PbS nanostructures have shown high thermal stability and good dark conductivity.

4.2 Experimental Details

4.2.1 Syntheses of IV-VI Nanostructures

a) SnS Nanostructures

SnS nanocomposites (nanoflowers and nanoflakes) are synthesized by solvothermal process by using stannous chloride ($SnCl_2.2H_2O$) and thiourea (NH_2CSNH_2) as precursors and ethylenediamine (*en*) as a solvent annealed at 200 °C for three different reaction times 1 h, 3 h and 5 h respectively. The SnS nanostructures are formed according to the following chemical reaction.

$$SnCl_2.2H_2O \rightarrow Sn^{2+} + Cl^{-} + H_2O$$
$$Sn^{2+} + n(en) \Leftrightarrow [Sn(en)_n]^{2+}$$
$$NH_2CSNH_2 + H_2O \rightarrow 2NH_3 + H_2S + CO_2$$
$$H_2S \rightarrow S^{2-} + 2H^{+}$$
$$[Sn(en)_n]^{2+} + S^{2-} \rightarrow SnS + n(en)$$

The formation of flake-like SnS is mainly caused by the intrinsic anisotropic nature of SnS. It consists of double layers of Sn and S perpendicular to *c*-axis. The weak Van der Waal forces between these layers provide the possibility of formation of this type of morphology [4.13, 4.14]. Ethylenediamine is known to be a very good complexing agent [4.15–4.17]. So when *en* is used as the solvent, the Sn ions which are produced from stannous chloride ($SnCl_2.2H_2O$) can be immediately captured by *en* molecules to form tin complex ions [4.18], and these could be linked by hydrogen bond and assembled into rod-like structures. After a certain time of reaction at elevated temperature and pressure, the stability of the complex decreases and S^{2-} immediately reacts with the aforesaid complexes to form SnS. The growth of SnS particles tends to be one-dimensional and the growth direction perpendicular to [010] with position-restrained effect of *en*. Finally, SnS grows crystals with certain width and length that results to be flake-like crystals, which may be caused by the different growth speed anisotropy of the crystal planes.

b) PbS Nanocubes

PbS nanocubes are synthesized by solvothermal process using lead acetate [$(CH_3COO)_2 Pb;3H_2O$] and thiourea (NH_2CSNH_2) precursors in ethylenediamine (*en*) solvent

annealed at 180 °C for three different reaction times 1 h, 2 h and 4 h respectively. It is well known that thiourea reacts with water at certain temperature to produce H_2S, and PbS forms through the reaction between H_2S and Pb^{2+}. The reaction process may be expressed as follows:

$$[(CH_3COO)_2 Pb; 3H_2O] \rightarrow Pb^{2+} + (CH_3COO)^- + H_2O$$
$$NH_2CSNH_2 + H_2O \rightarrow 2NH_3 + H_2S + CO_2$$
$$Pb^{2+} + H_2S \rightarrow PbS + 2H^+$$

The PbS nanoparticles could be produced through the above process and then PbS microcrystals would form through the aggregation growth process of PbS nanoparticles as the reaction time is increased [4.19].

Here for both SnS and PbS compounds, three different reaction times have been chosen to study the evolution of nanostructures and how their optical, thermal and electrical properties change with the increase of reaction times.

4.2.2 Characterizations and Studies

The various structural, optical, thermal and electrical properties are studied using different characterization tools. As-prepared SnS and PbS powder samples are studied by X-ray diffraction (XRD). Surface morphology of the powder samples are observed by scanning electron microscopy (SEM) and transmission electron microscopy (TEM). Compositional analysis is carried out by EDAX attached with SEM instrument. Optical properties of these as-synthesized powder samples are observed by UV-Vis-NIR transmittance, absorbance, photoluminescence (PL) and Raman studies. Thermal stability of these as-synthesized powder samples are also investigated by Thermo gravimetric analysis (TGA) at inert atmosphere of Ar. The details of characterizations are described in (Chapter 2, section 2.4).

For measurement of optical and electrical transport, thin films of SnS and PbS nanostructures are prepared using doctor's blade technique (Chapter 2, section 2.3). The films are found to be of nearly uniform thickness as seen by cross-sectional SEM measurement. The thicknesses of different films prepared by this technique ranges from 5-6 μm for SnS and 8-9 μm for PbS. UV-Vis-NIR transmission and absorbance as well as photoluminescence studies on the SnS and PbS thin films prepared on Corning 1739 glass substrate are also investigated.

Electrical transport measurements are done on SnS thin films prepared on Corning 1739 glass substrate (coplanar geometry) and PbS thin films prepared on ITO coated glass substrates (sandwich geometry). For PbS thin films sandwich geometry is chosen due to high resistivity and low carrier concentrations. Silver paste is used as a front electrode (with electrode width = 2 mm and length = 6 mm). The samples are mounted inside a metallic chamber with a transparent window. All the measurements are made in vacuum. A 100W halogen lamp with 10 mW/cm^2 intensity is used for illumination. Transport measurements are done while heating as well as cooling the samples and no difference in log σ vs 10^3/T is observed during the two cycles.

4.3 Results and Discussions

4.3.1 SnS Nanostructures

a) Structural Properties

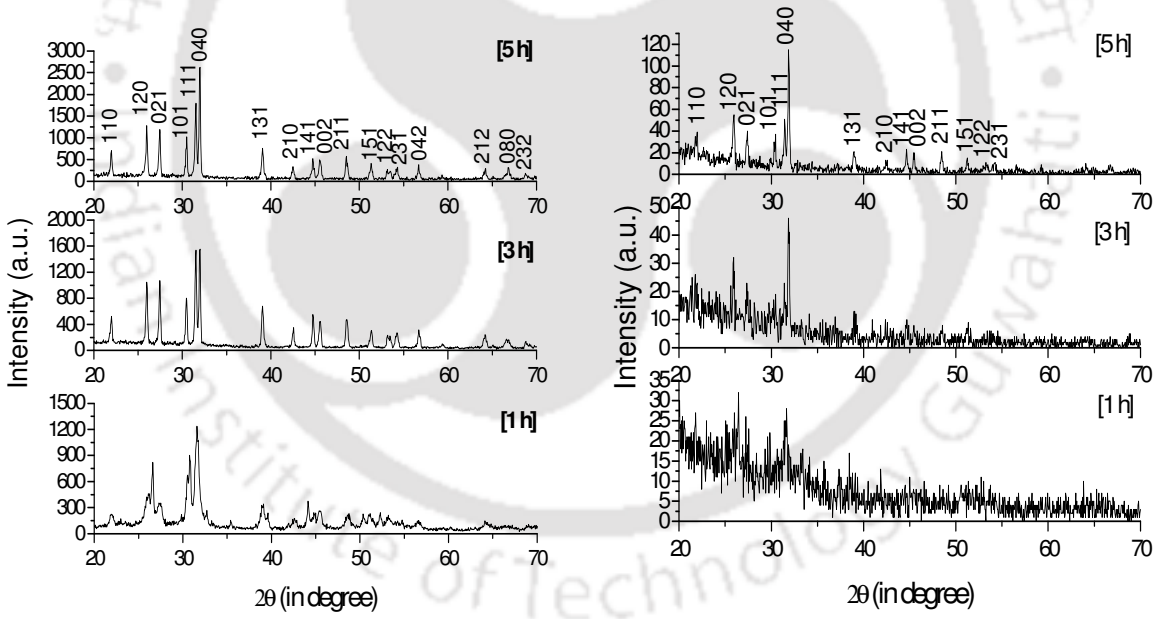

(a) **(b)**

Figure 4.1: XRD patterns of the SnS (a) as-prepared powder samples and (b) thin films prepared for three different reaction times.

Figure 4.1 show the XRD pattern of the SnS powder and thin film samples prepared for three different reaction times. The peaks in the XRD pattern of the SnS powder samples as well as thin films can be indexed to orthorhombic structure with lattice constants: *a* =

3.989 Å, b = 4.33 Å and c = 11.18 Å, which is in good agreement with the values from the standard card (JCPDS Cards No. 39-0354). From the XRD pattern, it is observed that diffraction peaks are becoming sharper with the increase of reaction time. This is an indication of increase of crystallite size with increase of reaction time. Though for the short reaction time the crystal growth has started however it's not getting a good size and shape to give some sharp peak in the XRD pattern. As reaction time is increasing, more number of atoms is coming together, resulting in the increase of crystallite size. Accordingly the peaks become sharper, well separated and its intensity also looks higher. Average grain size (D), dislocation density (δ), number of crystallites per unit area (N) and the strain (ε) of the SnS nanostructured prepared for all reaction times are obtained from XRD and are summarized in Table 4.1.

Table 4.1: Physical parameters of SnS nanostructured obtained from XRD data

Sample	**Grain size (D) (nm)**	**Dislocation density (δ) (lines/m^2)**	**Number of crystallites per unit area (N)**	**Strain (ε)**
SnS-1h	13	5.92×10^{15}	2.28×10^{18}	2.97×10^{-3}
SnS-3h	47	4.53×10^{14}	4.82×10^{16}	7.47×10^{-4}
SnS-5h	44	5.17×10^{14}	5.87×10^{16}	7.97×10^{-4}

Transmission Electron Microscopy (TEM), High Resolution Transmission Electron Microscopy (HRTEM) and Selected Area Electron Diffraction (SAED) patterns of the as-synthesized nanostructured SnS powder samples are presented in Figure 4.2. TEM images show that SnS powder samples are in flake shape with lengths varying from few hundred nanometers to several micrometers whereas thicknesses of these flakes varies from 50-80 nm. From HRTEM images and SAED patterns, it is clear that SnS powder samples are well crystalline in nature. The interplanar spacings and corresponding planes of these powder samples are given in Table 4.2.

Table 4.2: d-spacing and corresponding plane of the SnS powder samples obtained from HRTEM images

Samples	d-spacing (nm)	Corresponding Plane
SnS-1h	0.3095	101
SnS-3h	0.2777	040
SnS-5h	0.2802	111

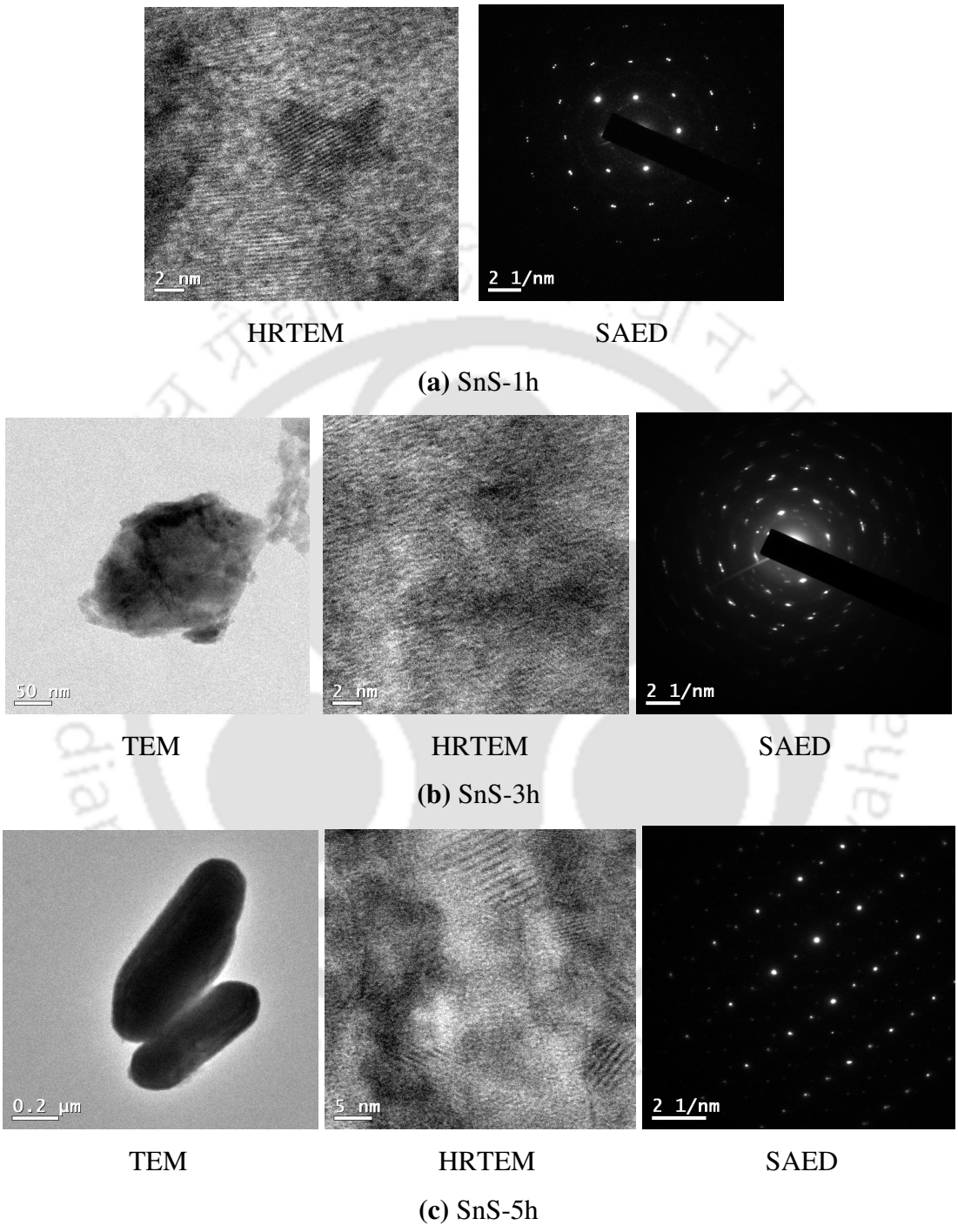

Figure 4.2: TEM, HRTEM and SAED patterns of the SnS powder samples prepared for three different reaction times.

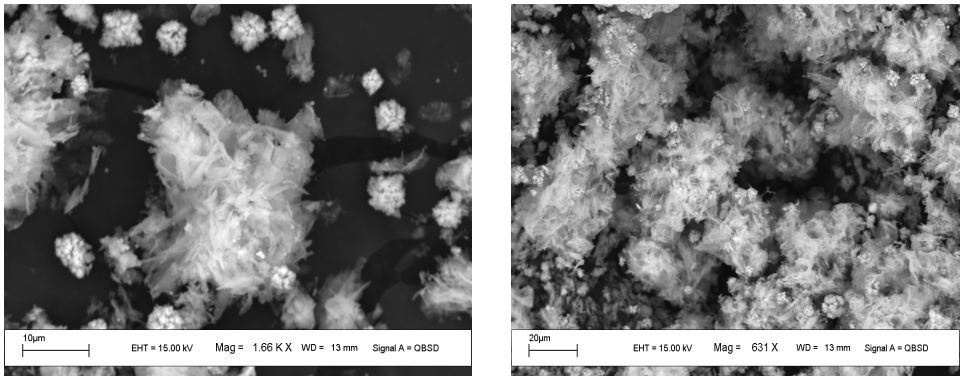

(a) SnS-1h

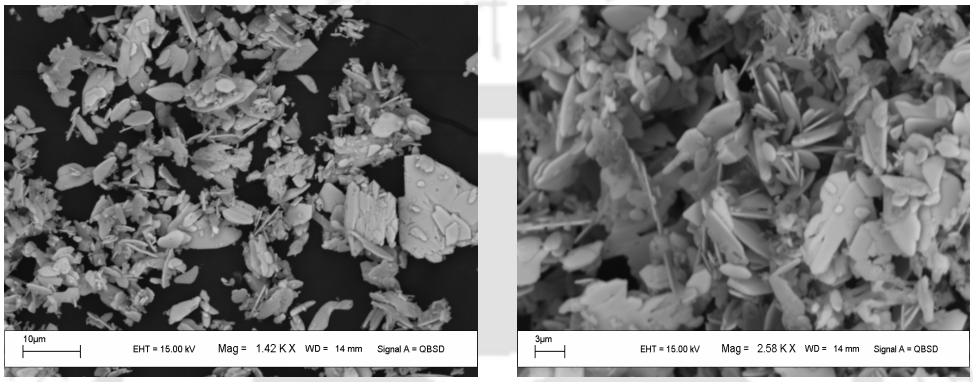

(b) SnS-3h

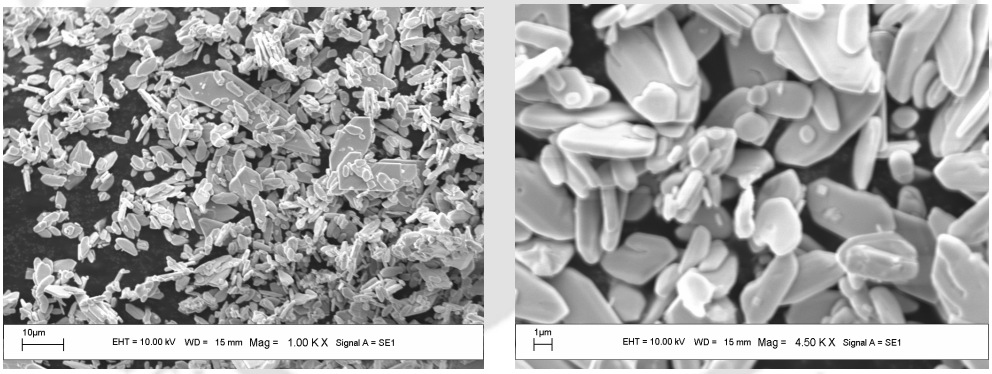

(c) SnS-5h

Figure 4.3: SEM images of the SnS nanostructured powder samples prepared for three different reaction times.

Figure 4.3 represent the SEM images of the SnS powder samples. Figure 4.3 suggest that for samples prepared with short reaction time the shape is like a nanoflower, it changes to nanoflakes as reaction time is increased. It is also observed that thickness of the SnS nanostructured materials increase with increasing reaction time which also support the XRD results. Chemical purity and stoichiometric ratio of the as-synthesized SnS powder samples are obtained by EDAX (Figure 4.4). It is also observed that SnS powder samples are chemically pure and the stoichiometric ratios are almost same for all samples. The atomic

ratio of Sn to S is ~1, indicating that the phase of the obtained product is SnS and there are slight sulfur deficiencies in SnS nanocomposites (Table 4.3).

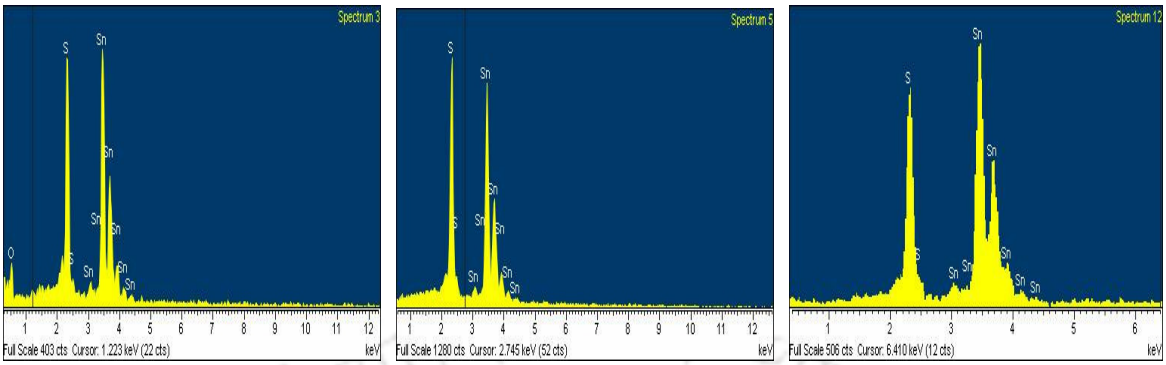

Figure 4.4: EDAX patterns of the SnS powder samples.

Table 4.3: Stoichiometric ratio of SnS powder samples at three different reaction times

Sample	Sn	S
SnS-1h	53.80	46.20
SnS-3h	50.90	49.10
SnS-5h	52.96	47.04

b) Optical Properties

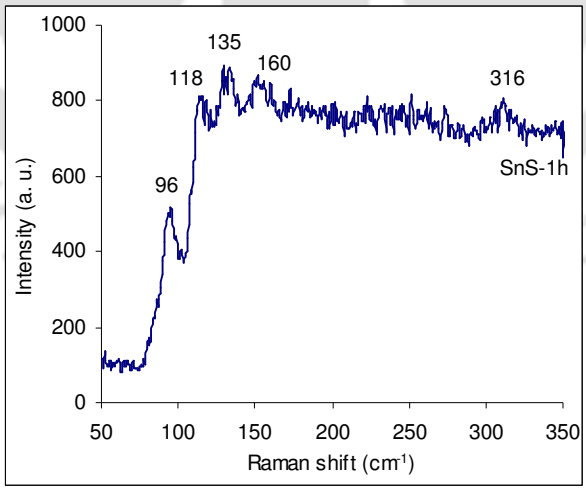

Figure 4.5: Raman spectra of the SnS nanostructured powder sample prepared for 1h reaction time.

Figure 4.5 shows the Raman spectrum of the SnS nanostructured powder samples prepared for 1 h reaction time. In the range of 50-350 cm^{-1}, there are five distinct peaks located at 96, 118, 135, 160 and 316 cm^{-1} respectively. When compared to the predicted data

of orthorhombic SnS crystal [4.20], the peaks observed at 96 and 118 cm^{-1} could be assigned to the A_g modes. The remaining peaks observed at 135, 160 and 316 cm^{-1} could be assigned to the B_{2g} modes of SnS. The results are in agreement with the literature reference value for SnS single crystal [4.20]. As a consequence, the Raman spectra showed that the as-prepared product is composed of single phase SnS with orthorhombic structure.

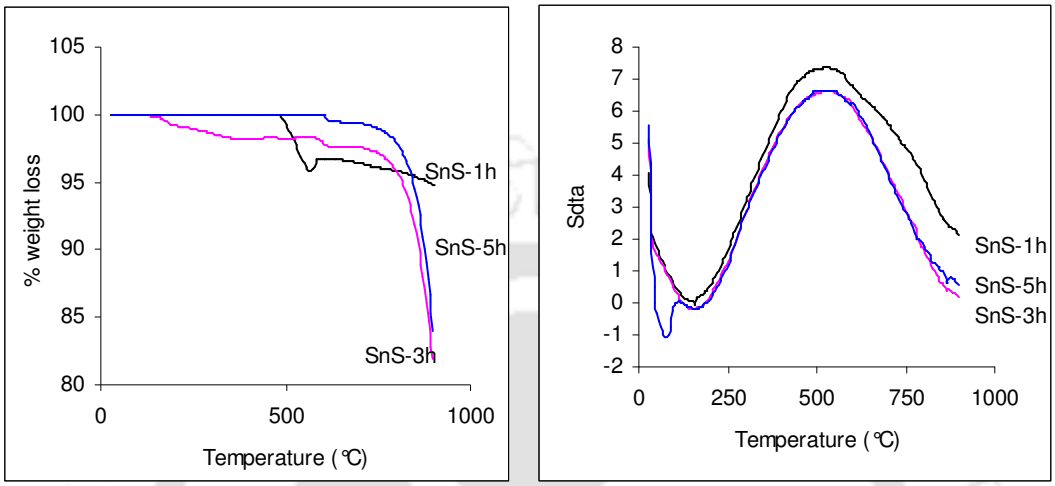

(a) TGA **(b)** SDTA

Figure 4.6: (a) TGA and (b) SDTA curve of the SnS nanostructured powder samples prepared for three different reaction times.

c) Thermal Stability Studies

Thermal stability studies (Figure 4.6) of these SnS nanostructured powder samples are performed by thermo gravimetric analysis (TGA). From Figure 4.6 it is observed that SnS powder samples prepared for 1 h reaction time is stable up to 495 °C due to low crystallinity whereas SnS prepared for 3 h and 5 h are stable up to 620 °C because of the high crystallinity. No weight loss observed in the temperature range of 100-200 °C suggests that SnS powders are totally dried. After 900 °C, only 5%, 18% and 16% weight loss is observed for SnS powder samples prepared for 1 h, 3 h and 5 h reaction time respectively. Table 4.4 presents the results of thermo gravimetric analysis (TGA) and weight loss of these nanocomposites during degradation in an atmosphere of Ar.

Table 4.4: Results of thermal degradation of SnS nanocomposites measured by TGA in Ar atmosphere at 10 ºC/min heating rate

Sample	Maximum break T(ºC)	Residual weight (%)			
		600 ºC	700 ºC	800 ºC	900 ºC
SnS-1h	495	96.76	96.43	95.83	94.78
SnS-3h	740	100.00	97.57	95.97	81.85
SnS-5h	740	100.00	99.35	98.03	83.96

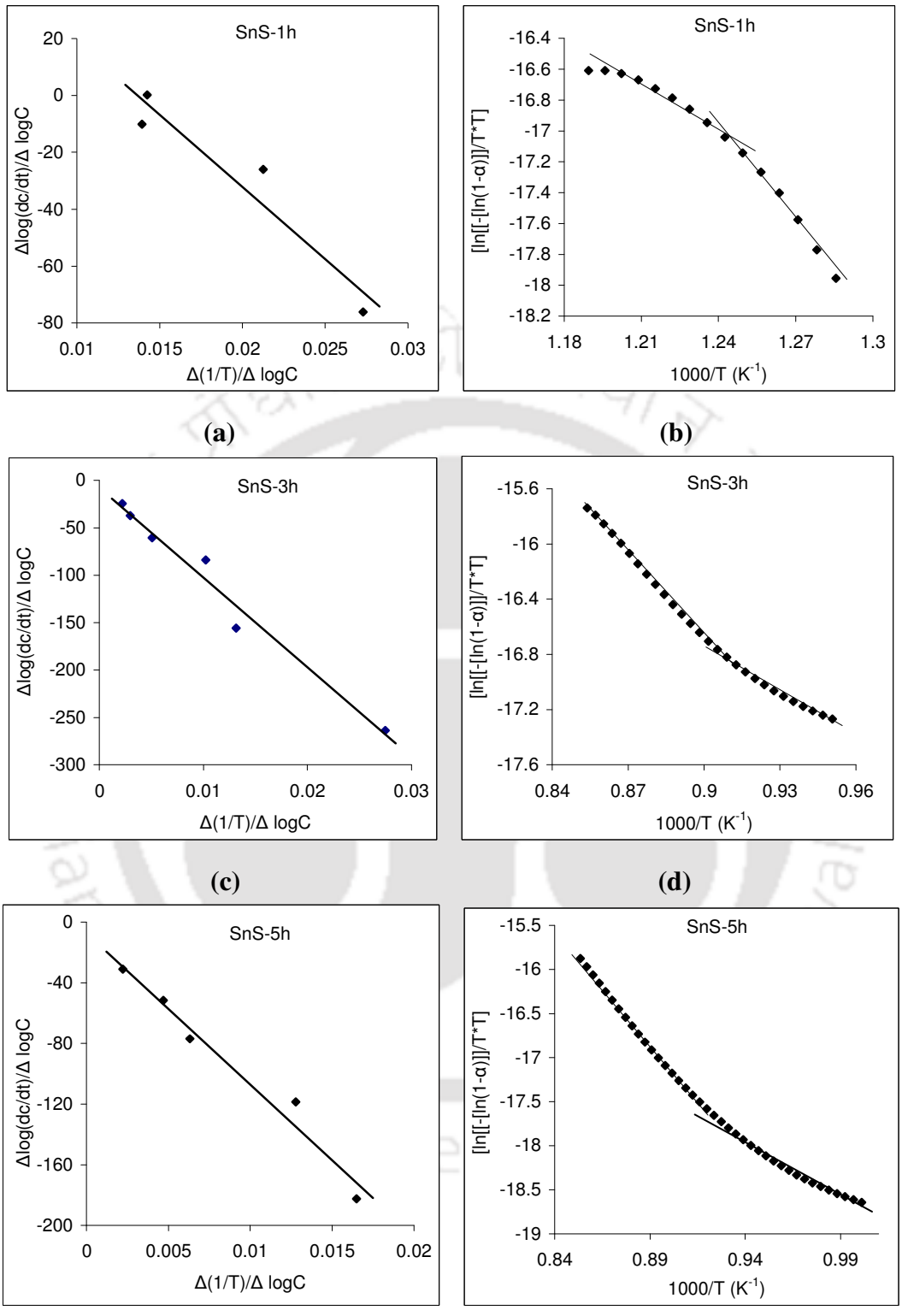

Figure 4.7: Determination of kinetic parameters by (a, c, e) Freeman and Carroll Method and (b, d, f) Coats-Redfern Model from TG data of SnS powder samples prepared for 1 h, 3 h and 5 h respectively.

We have also investigated the simultaneous differential thermal analysis (SDTA) of these SnS powder samples. It is observed that the particle size of the nanostructured materials influences the SDTA results. The smaller the particle size, the larger is the exothermic peak area of the SDTA curve because the decomposition of a sample with a large particle size is slower than that of a sample with a large specific surface area. The observed peak areas of the SDTA curves of the SnS nanocomposites (Figure 4.6b) are also very broad, which indicate that the sizes of the particles are very small. This also supports that the as-synthesized SnS powders are in nano-order ranges.

Kinetic parameter information like thermal activation energy (E), Arrhenius parameter (A) and entropy of activation (ΔS) of the SnS nanostructured powder samples are also obtained by Coats-Redfern and Freeman-Carroll Methods (Chapter 2, subsection 2.4.3) using TG data (Figure 4.7) and the results are summarized in Table 4.5. For Coats-Redfern model, the best fits are obtained for $g(\alpha) = [-\ln (1-\alpha)] = kt$, where k is the Boltzmann's constant and t is the time. This relation corresponds to random nucleation with one nucleus on each particle. From Table 4.5, it is observed that in both kinetic methods, thermal activation energy increases with the increase of reaction time which suggests that thermal stability increases with the increase of reaction times. These results are also in agreement with the XRD and SEM results.

Table 4.5: Kinetic parameters of the SnS powder samples obtained from different kinetic models

Sample	**Methods**				
	Coats-Redfern				**Freeman and Carroll**
	Activation energy E (kJ/mol)		Arrhenius parameters A (s^{-1})	Entropy ΔS (J/degree/mol)	Activation energy E (kJ/mol)
	1^{st} step	2^{nd} step			
SnS-1h	86	227	2667	-187	97
SnS-3h	99	175	16416	-172	181
SnS-5h	112	220	3645	-184	193

d) Electrical Transport Studies

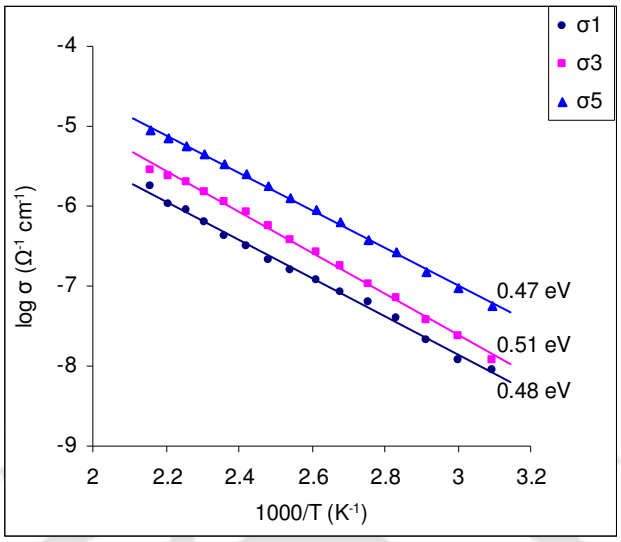

Figure 4.8: Variation of dark conductivity with temperature for the SnS nanostructured thin films (here σ_1, σ_3 and σ_5 indicate the dark conductivities of the nanostructured SnS thin films prepared for 1 h, 3 h and 5 h respectively).

Figure 4.8 shows the dark conductivities of the SnS nanostructured thin films in the temperature range 300- 463 K. It is observed that the dark conductivity is thermally activated following Arrhenius equation,

$$\sigma = \sigma_0 \exp(-E_a/kT)$$

where E_a denotes the activation energy of electrical conduction, σ_0 is a parameter depending on the material properties, k the Boltzmann's constant and T is the absolute temperature. The activation energy from the slope of the straight lines are calculated as 0.48, 0.51 and 0.47 eV for samples prepared for 1 h, 3 h and 5 h respectively suggesting that the deep acceptor levels associated with the excess of tin atoms are responsible for electrical conduction. This is in good agreement with the electrical activation energy of the SnS thin films obtained by Nair *et al*. [4.21] (0.44 eV) and Reddy *et al*. [4.22] (0.35-0.46 eV) for the SnS thin films prepared by two different techniques. They have also shown that the electrical activation energy is decreased with the increase of films thicknesses which is basically due to the charge carrier trapping at the surface and intergrain boundaries which are thickness dependent [4.23]. We don't observe any photocurrent under the illumination of halogen lamp in case of our nanostructured SnS thin films, which may be due to low illumination intensity (10 mW/cm^2),

where as Nair *et al.* [4.21] reported the photo- to dark-current ratio only one order of magnitude or less under 50 mW/cm^2 of light intensity.

4.3.2 PbS Nanocubes

a) Structural Properties

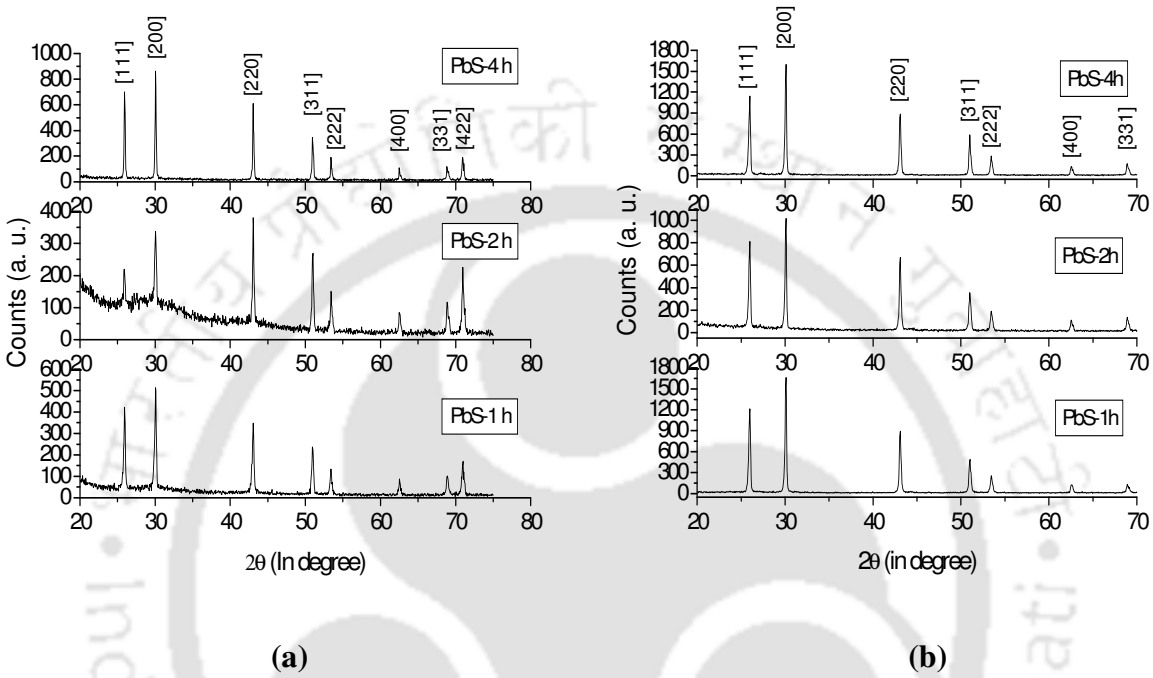

Figure 4.9: XRD pattern of the PbS (a) powder samples and (b) thin films prepared for three different reaction times.

XRD patterns of the PbS powder as well as thin film samples prepared for three different reaction times are presented in Figure 4.9. All the diffraction peaks can be indexed to the face-centered cubic (fcc) phase of PbS with lattice constant a = 5.932 Å, which is in good agreement with the values a = 5.936 Å from the standard card (JCPDS No.5-592). No observable impurity phases could be detected in XRD studies. The sharp diffraction peaks suggest that the products are highly crystalline. The d-spacings are calculated from the Bragg's relation $d = n\lambda/2\sin\theta$, where λ value is 1.54056 Å. The d-values are in good agreement with ASTM data which are summarized in Table 4.6.

It is interesting to note that the ratio of (200) and (111) peaks is nearly same to the conventional value (1.2) for bulk samples, which indicates that the as-grown nanocubes are randomly oriented [4.24]. We have also calculated the average grain size (D), dislocation

density (δ), number of crystallites per unit area (N) and the strain (ε) of the PbS nanostructured from XRD which are summarized in Table 4.7.

Table 4.6: Calculated d-spacings of the PbS powder samples from XRD data

Sl.no	2θ (deg.)	sinθ	d (Å) (expt.)	d* (Å) (ASTM)	Plane (hkl)
1	25.955	0.22457	3.430	3.429	(111)
2	30.067	0.25968	2.966	2.969	(200)
3	43.064	0.36702	2.098	2.099	(220)
4	50.99	0.43043	1.789	1.790	(311)
5	53.429	0.44955	1.713	1.740	(222)

Table 4.7: Physical parameters of PbS nanostructured obtained from XRD

Sample	**Grain size (D) (nm)**	**Dislocation density (δ) (lines/m^2)**	**Number of crystallites per unit area (N)**	**Strain (ε)**
PbS-1h	38	6.93×10^{14}	1.64×10^{17}	9.17×10^{-4}
PbS-2h	44	5.17×10^{14}	1.06×10^{17}	7.97×10^{-4}
PbS-4h	56	3.19×10^{14}	5.13×10^{16}	6.27×10^{-4}

Typical TEM and SEM images of the samples provide direct information about the size and morphology of the PbS particles grown for different periods of time. TEM images (Figure 4.10) of the powder samples confirm the formation of PbS nanocubes. It is observed that the particle size increase with the increase of reaction times. The average particle size of the PbS nanocubes are varying from 25–300 nm. HRTEM and SAED patterns of the PbS nanocubes for 1 h and 2 h powder samples also confirm the single crystalline nature. The interplanar spacing for the samples prepared for 1 h and 2 h are obtained from HRTEM images as 0.28 nm (corresponding to plane 200) and 0.24 nm (corresponding to plane 220) respectively. No HRTEM image is observed for 4 h samples because electron beams cannot penetrate 4 h samples due to larger particle sizes with respect to 1 h and 2 h samples.

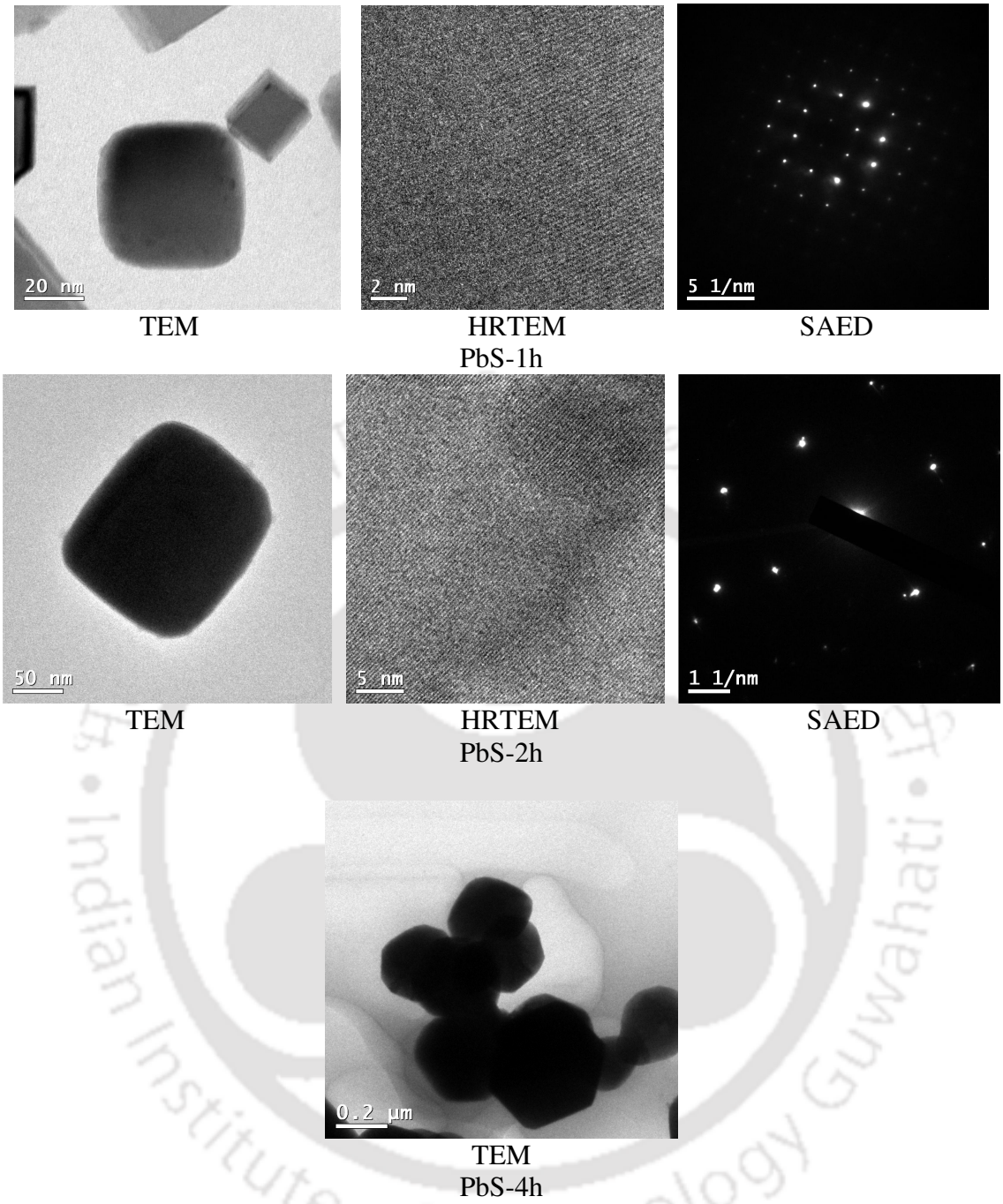

Figure 4.10: TEM, HRTEM and SAED patterns of the PbS nanocubes powder samples prepared for three different reaction times.

SEM images (Figure 4.11) of the PbS powder samples show that these are cubic in shape. Chemical purity and stoichiometric ratio of the PbS powder samples are obtained by EDAX (Figure 4.12). It is observed that PbS powder samples are chemically pure and the stoichiometric ratios are almost same for all three different samples and there are slight sulfur deficiencies in PbS nanocomposites (Table 4.8).

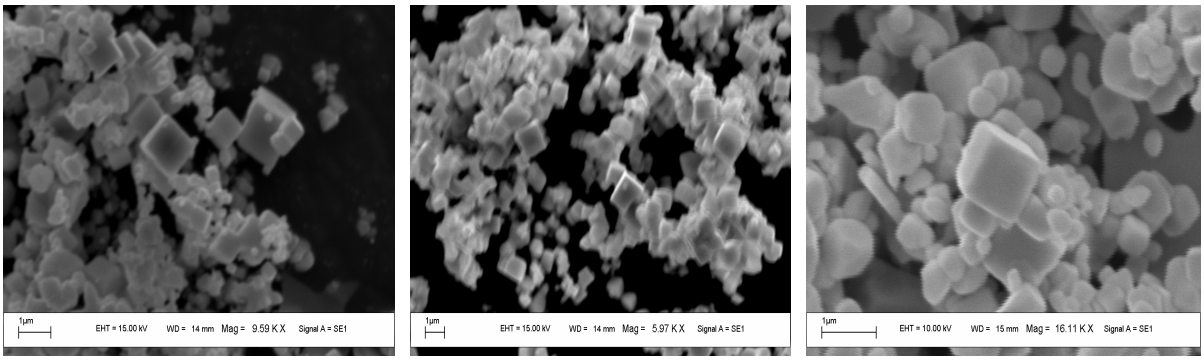

(a) **(b)** **(c)**

Figure 4.11: SEM images of the as-synthesized PbS powder samples prepared for (a) 1 h, (b) 2 h and (c) 4 h reaction times.

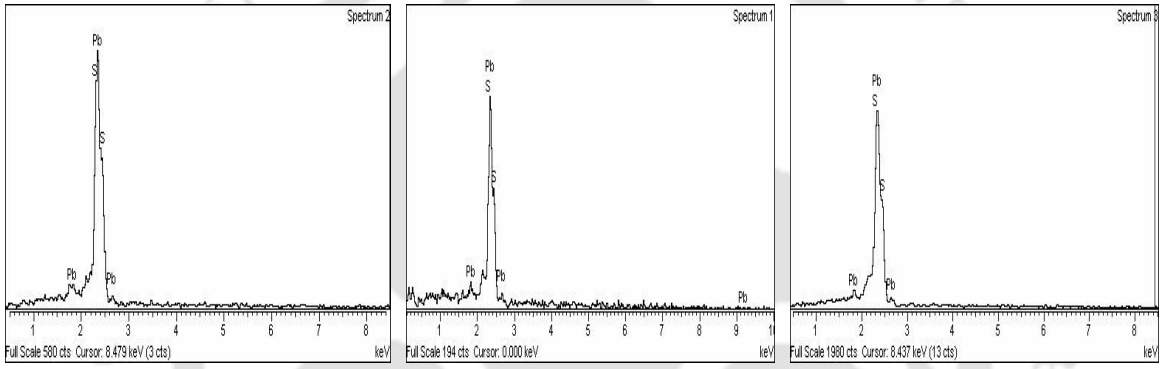

PbS-1h PbS-2h PbS-4h

Figure 4.12: EDX patterns of the PbS nanocubes powder samples

Table 4.8: Stoichiometric ratios of the as-synthesized PbS nanocubes

Sample	Pb	S
PbS-1h	51.48	48.52
PbS-2h	53.84	46.16
PbS-4h	51.86	48.14

b) Optical Properties

Figure 4.13 show the UV-Vis-NIR absorbance and transmission measurements of the PbS nanocubes in ethanol solution. The UV-Vis-NIR absorbance and transmission measurements, done in the range of 200-1000 nm, show a nearly flat transmission (≈ 20%). A slight increase in transmission is observed for particles with 1 h reaction time. No absorption edge is observed even for wavelength down to 200 nm, which indicates that the band gap of these nanostructured is much higher than that for bulk PbS crystals (0.41 eV).

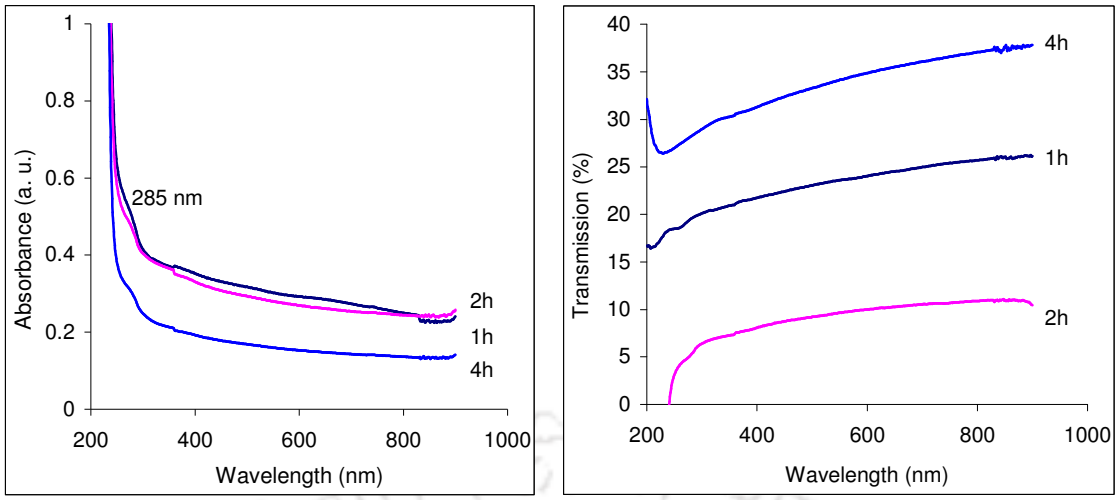

(a) **(b)**

Figure 4.13: (a) Absorbance and (b) transmittance of the PbS nanocubes in ethanol solution.

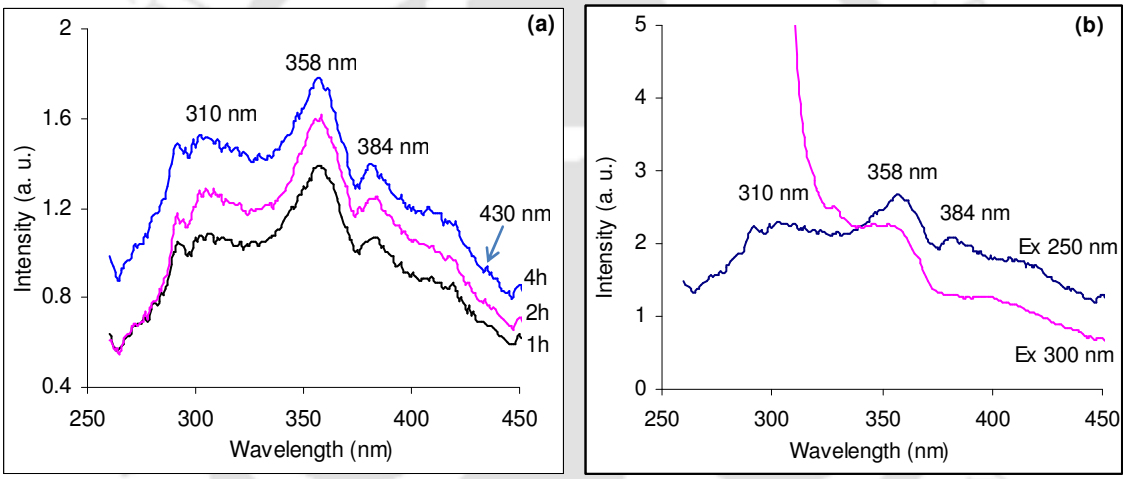

Figure 4.14: PL spectra of the PbS nanocubes (a) at 250 nm of excitation wavelength prepared for three different reaction times and (b) at 250 nm and 300 nm of excitation wavelength prepared for 4 h reaction time.

In order to have an idea of the optical band gap of these nanostructures, PL emission spectra are recorded for excitation wavelength of 250 nm and 300 nm. The emission peak of PL spectra corresponds to the band to band transition or transition involving conduction band edge and surface or defects states. Figure 4.14a shows the PL emission spectra for different samples for excitation wavelength of 250 nm. The emission spectrum shows a broad peak at around 310 nm, relatively two narrow peaks at 358 nm and 384 nm with shoulder at around 430 nm. Similar features are observed for excitation wavelength of 300 nm, where lower wavelength end of 310 nm peak cannot be seen due to high flux of scattered excitation

photons (Figure 4.14b). The peak at 433 nm has been reported to be associated with the transition of electrons for the conduction band edge to holes trapped at interstitial site [4.25]. The origin of transitions involving other peaks are not very clear at this moment but could be due to band to band transition and transition between the conduction band edge and defects states.

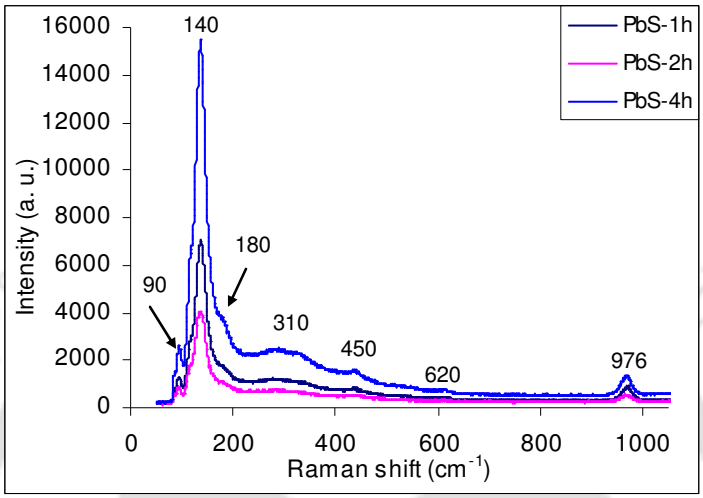

Figure 4.15: Raman spectra of the PbS nanocubes powder samples prepared for three different reaction times.

The Raman spectra of the PbS nanocubes structures (Figure 4.15) indicates seven bands in the range of 50-1100 cm^{-1}, located at around 90, 140, 180, 310, 450, 620 and 976 cm^{-1}. The peak observed at 90 cm^{-1} could be assigned an acoustic mode [4.26]. The strong band centred at 140 cm^{-1} originated from the combination of longitudinal and transverse acoustic modes [4.27]. Additionally, a weak band at about 180 cm^{-1} usually comes from the fundamental longitudinal optical (LO) phonon mode and those at 450 and 620 cm^{-1} are from its first and second overtones (2LO and 3LO), respectively [4.26, 4.27]. It has been reported that the band centred at 976 cm^{-1} could arise from sulfates presented in the sample [4.27]. However, in our sample, the XRD pattern of the PbS nanocubes structures confirmed that the product consist of pure cubic PbS without the presence of sulfates. As a result, the band centred at 976 cm^{-1} could be due to sulfates in the sample originating from the laser-induced degradation, which is consistent with results reported previously [4.28]. The Raman spectra of the other PbS novel nanostructures [4.29] are similar to that of PbS nanocubes synthesized by solvothermal process.

c) Thermal Stability Studies

Thermal stability studies (Figure 4.16) are performed by TGA. No weight loss is observed up to 700 °C suggest that PbS nanocubes prepared by solvothermal process are totally dried. After 900 °C, only 13% weight loss is observed for the samples prepared for 1 h and 7-8% weight loss is observed for 2 h and 4 h reaction time respectively, which could be due to the evaporation of sulfur from the broken PbS bonds.

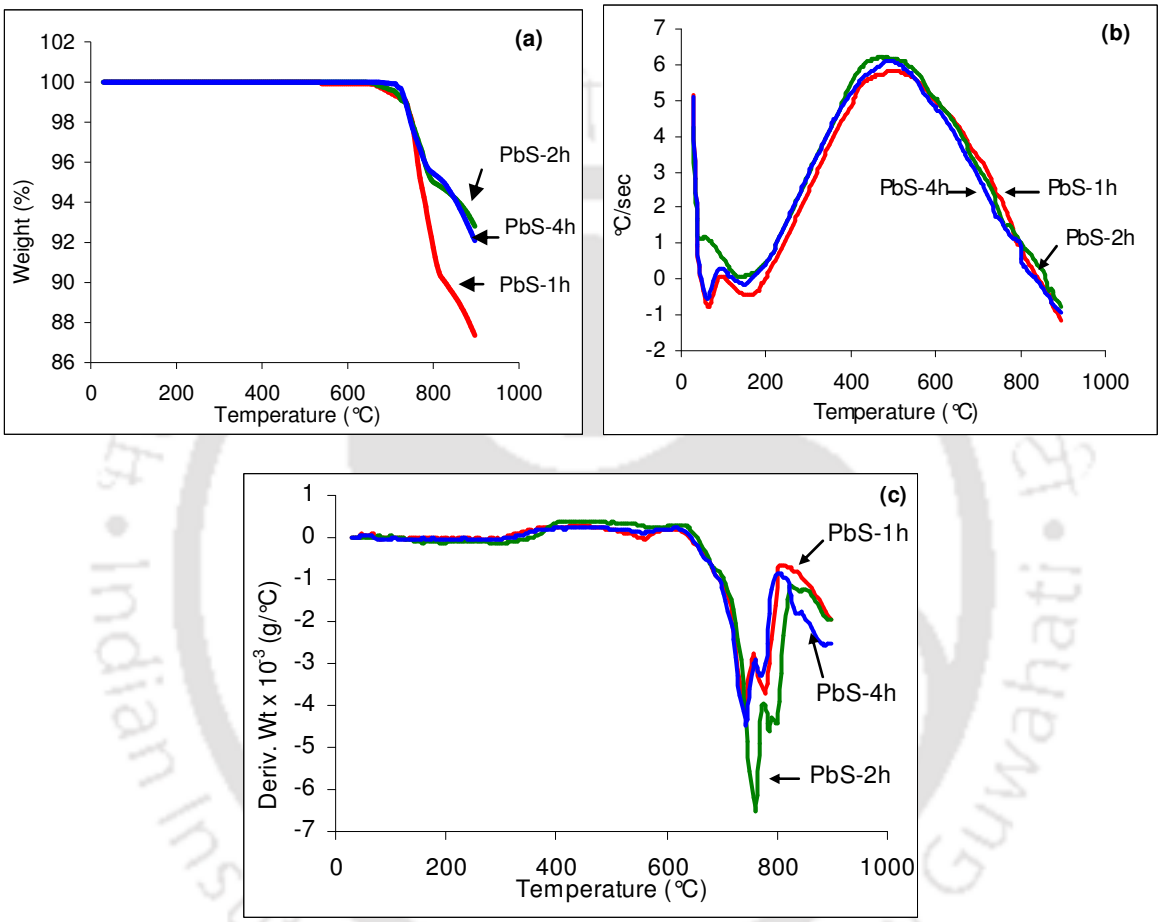

Figure 4.16: (a) TGA, (b) SDTA and (c) DTG curves of the PbS nanocubes powder samples prepared for three different reaction times.

We have also studied the simultaneous differential thermal analysis (SDTA) on these samples. The observed peak areas of the SDTA curves of the PbS nanocubes (Figure 4.16b) are also very broad, which indicate that the sizes of the particles are very small. This also supports that the as-synthesized PbS powders are in nano-order ranges. From derivative thermo gravimetric (DTG) curve (Figure 4.16c) of the PbS nanocubes powder samples two endothermic peak are observed at 760 °C and 800 °C, which could be due to the change in phase or structure.

Kinetic information like thermal activation energy (E), Arrhenius parameter (A) and entropy of activation (ΔS) of the PbS powder samples prepared for three different reaction times are also obtained by Coats-Redfern model (Figure 4.17) and the results are summarized in Table 4.9. For Coats-Redfern model, the best fits are obtained for $g(\alpha) = [-\ln (1-\alpha)] = kt$, where k is the Boltzmann's constant and t is the time. This relation corresponds to random nucleation with one nucleus on each particle. It is observed that the activation energy increases with the increase of reaction time which suggest that thermal stability of these samples are increased with the increase of reaction times.

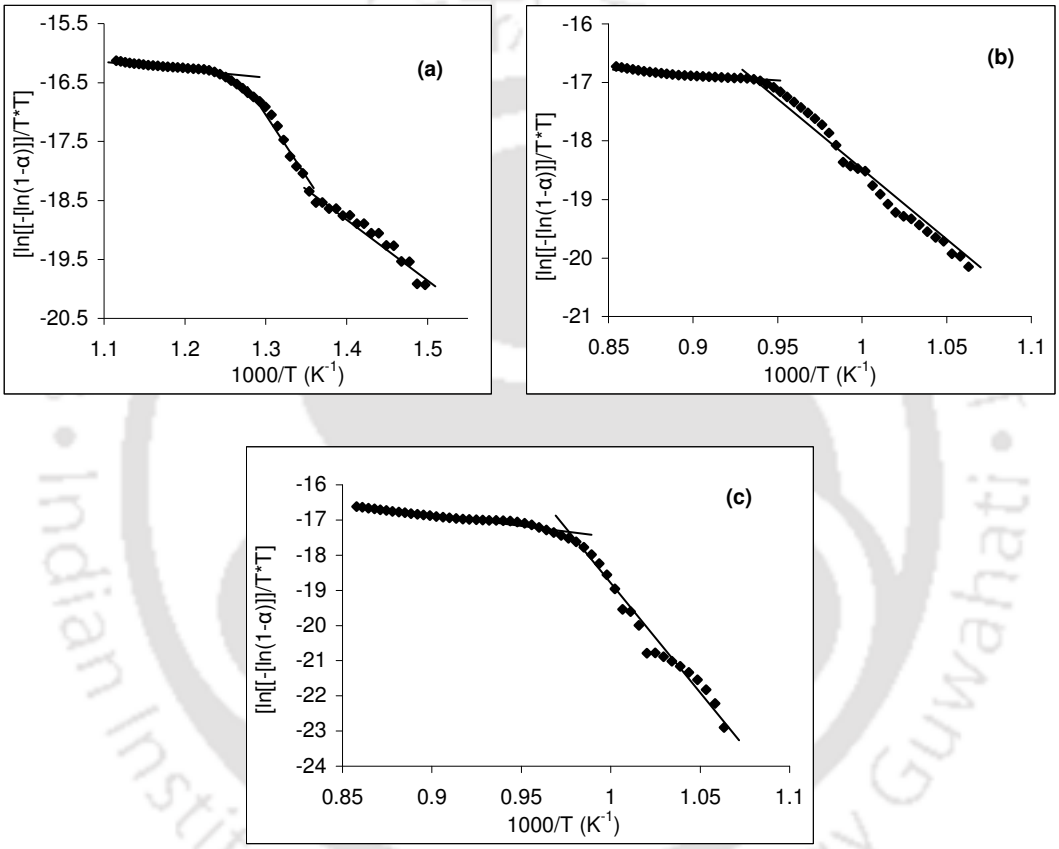

Figure 4.17: Determination of kinetic parameters by Coats-Redfern Model for (a) PbS-1h, (b) PbS-2h and (c) PbS-4h.

Table 4.9: Kinetic parameters of the PbS nanocubes powder samples

Sample	Coats-Redfern model		
	Activation energy E (kJ/mol)	Arrhenius parameters $Ax10^5$ (s^{-1})	Entropy ΔS (J/degree/mol)
PbS-1h	162	5.3	-67
PbS-2h	228	5.8	-39
PbS-4h	271	1.0	-66

d) Electrical Transport Studies

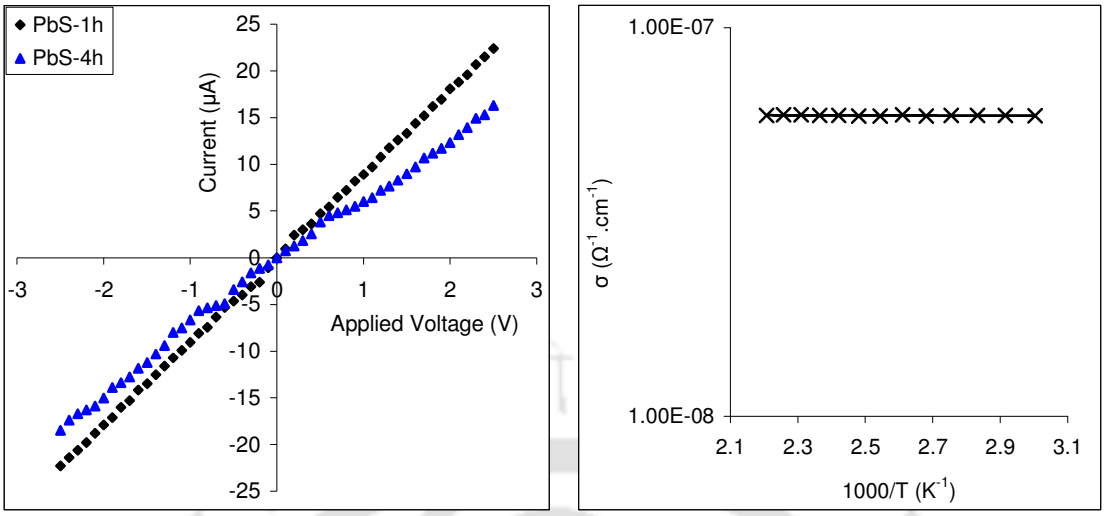

(a) **(b)**

Figure 4.18: (a) I-V characteristics and (b) dark conductivity of the PbS nanocubes.

We have measured the I-V characteristics of the PbS nanostructured thin films to study the metal-semiconductor junctions. From Figure 4.18a, it is observed that I-V curves are nearly a straight line and goes through the origin, which suggests that metal-semiconductor junctions are ohmic in nature. Figure 4.18b shows a plot between σ and 1000/T. The temperature has been varied from 303 K to 453 K. It is observed that the conductivity is nearly constant through this temperature range. So that it's thermal activation energy is nearly zero. The films do not show any photoconductivity for the visible photon flux as PbS is known to be IR detector. The nearly uniform and low dark conductivity for these films ensures these films to be good material for IR detector application.

4.4 Conclusions

SnS and PbS nanostructured powder samples are successfully synthesized by solvothermal process. It is observed that the surface morphology and crystallinity of these materials are totally dependent on the reaction time and crystallinity is increased with the increase of reaction time. These materials also show good optical behaviors. Kinetic parameters such as activation energy (E) for the degradation, Arrhenius parameter (A) and the entropy change (ΔS) of SnS and PbS nanostructured powder samples are calculated by two kinetic models and it is observed that thermal activation energy is increased with the increase of reaction time for sample preparation, which suggest that crystallinity of these samples increase with the increase of reaction time. SnS and PbS nanostructured thin films

are prepared by doctor blade technique for the measurement of optical and electrical transport measurements. Thin films prepared by this technique have also shown good dark conductivity.

4.5 References

[4.1] K. T. R. Reddy, N. K. Reddy and R. W. Miles, Sol. Energy Mater. Sol. Cells **90**, 3041 (2006).

[4.2] D. Avallaneda, G. Delgado, M. T. S. Nair and P. K. Nair, Thin Solid Films **515**, 5771 (2007).

[4.3] K. T. R. Reddy and N. K. Reddy, Mater. Chem. Phys. **102**, 13 (2007).

[4.4] W. Albers, C. Hass, H. J. Vink and J. D. Wasscher, J. Appl. Phys. Suppl. **32**, 2220 (1996).

[4.5] M. Parenteau and C. Carlone, Phys. Rev. B **41**, 5227 (1990).

[4.6] R. D. Engelken, H. E. McCloud, C. Lee, M. Slayton and H. Ghoreishi, J. Electrochem. Soc.**134**, 2696 (1987).

[4.7] M. T. S. Nair and P. K. Nair, Semicond. Sci. Technol. **6**, 132 (1991).

[4.8] M. B. Prince, J. Appl. Phys. **26**, 534 (1955).

[4.9] O. Madelung, M. Schulz, and H. Weiss, Landolt–Börnstein, *Numerical Data and Functional Relationships in Science and Technology*, New Series, Group III, Vol. 17, Part f (Springer, Berlin, 1983).

[4.10] L. Pintilie, M. Alexe, I. Pintilie, and T. Botila, Appl. Phys. Lett. **69**, 1571 (1996).

[4.11] R. Bayon, R. Musembi, A. Belaidi, M. Bar, T. Guminskaya, M. Ch. Lux-Steiner and Th. Dittrich, Sol. Energy Mater. Sol. Cells **89**, 13 (2005).

[4.12] S. Gunes, K. P. Fritz, H. Neugebauer, N. S. Sariciftci, S. Kumar and G. D. Scholes, Sol. Energy Mater. Sol. Cells **91**, 420 (2007).

[4.13] F. Hulliger, F. Levy, D. Reidel (Eds.), *Structural Chemistry of Layer Type Phases*, Dordrecht, Holland/Boston, 1976.

[4.14] W. Albers, C. Hass and E. Van der Masesn, J. Phys. Chem. Solids **15**, 306 (1960).

[4.15] J. H. Zhan, X. G. Yang, D. W. Wang, S. D. Li, Y. Xie, Y. Xia and Y. T. Qian, Adv. Mater. **12**, 1348 (2000).

[4.16] W. S. Sheldrik and M. Wachhold, Angew. Chem. Int. Ed. Engl. **36**, 206 (1997).

[4.17] S. Gorai, D. Ganguli and S. Chaudhuri, Mater. Sci. Eng. B **116**, 221 (2005).

[4.18] Z. Zhang, X. Shao, H. Yu, Y. Wang and M. Han, Chem. Mater. **17**, 332 (2005).

[4.19] D. B. Kuang, A. W. Xu, Y. P. Fang, H. Q. Liu, C. Frommen and D. Fenske, Adv. Mater. **15**, 1747 (2003).

[4.20] H. R. Chandrasekhar, R. G. Humphreys, U. Zwick and M. Cardona, Phys. Rev. B **15**, 2177 (1977).

[4.21] M. T. S. Nair and P. K. Nair, Semicond. Sci. Technol. **6**, 132 (1991).

[4.22] N. K. Reddy and K. T. R. Reddy, Solid State Electron. **49**, 902 (2005).

[4.23] J. W. Orton, B. J. Goldsmith, J. A. Chapman and M. J. Powell, J. Appl. Phys. **53**, 1602 (1982).

[4.24] G. Zhou, M. Lu, Z. Xiu, S. Wang, H. Zhang, Y. Zhou and S. Wang, J. Phys. Chem. B **110**, 6543 (2006).

[4.25] S. Xiong, B. Xi, D. Xu, C. Wang, X. Feng, H. Zhou and Y. Qian, J. Phys. Chem. C **111**, 16761 (2007).

[4.26] (a) T. D. Krauss and F. W. Wise, Phys. Rev. B **55**, 9860 (1997). (b) T. D. Krauss, F. W. Wise and D. B. Tanner, Phys. Rev. Lett. **76**, 1376 (1996). (c) T. D. Krauss and F. W. Wise, Phys. Rev. Lett. **79**, 5102 (1997).

[4.27] G. D. Smith, S. Firth, R. J. H. Clark and M. Cardona, J. Appl. Phys. **92**, 4375 (2002).

[4.28] H. Q. Cao, G. Z. Wang, S. C. Zhang and X. R. Zhang, Nanotechnology **17**, 3280 (2006).

[4.29] S. Xiong, B. Xi, D. Xu, C. Wang, X. Feng, H. Zhou and Y. Qian, J. Phys. Chem. C **111**, 16761 (2007).

CHAPTER-5

Synthesis and Studies of Conjugated Polymers Blend with Nanostructured Semiconductors

CHAPTER 5: Synthesis and Studies of Conjugated Polymers Blend with Nanostructured Semi-conductors

5.1 Introduction

Over the last decades a significant amount of research activity has focused on semi-conducting (conjugated) polymers like **p**oly **a**cetylene (PA), **p**oly **p**ara-**p**henylene (PPP), **p**oly para-**p**henylene-**v**inylene (PPV), **p**oly**t**hiophenes (PT), **p**oly**f**luorene (PF) and their derivatives because of their potential applications in light-emitting devices [5.1-5.4], photovoltaic cells [5.5, 5.6], biosensors [5.7], organic lasers [5.8], rechargeable batteries [5.9, 5.10] all polymer field effect transistors [5.9], non-linear optics [5.11], separation of gases [5.12] and ion exchange membranes [5.13] combined with attractive material properties such as low weight and ease of processing. The conductivity of these polymers, which are otherwise highly insulating can be enhanced by several orders of magnitude by doping with metals and other compounds making these useful for device applications. However, most of these doped polymers often have limitations like poor stability of physical and chemical properties in different environments. Doped PPP, on the other hand have been found to have high thermally stability and resistant to oxidation and chemical degradation and thus more useful for device application. Besides being stable, PPP has several other advantages such as the simplest rigid-rod like structure composed of phenylene rings connected between para (1, 4) positions, high tensile strength, high compressive strength, high electrical conductivity on doping [5.14-5.17], wide conductivity range and high quantum yield in electroluminescence [5.18]. Importantly, PPP has also been reported to show blue luminescence [5.19]. Several transition metal catalyzed routes for the synthesis of PPP that have appeared in literature [5.20] report average molecular weight of these polymers in the range of approximately M_n=30000 with poly dispersity index 1.18 [5.21].

Polyfluorene and its copolymers have also emerged as an attractive class of light emitting polymers for LEDs due to their high photoluminescence (PL) quantum yields in the solid-state, thermal stability, good solubility, and good charge transport properties [5.22–5.25]. Recent studies have shown that polyfluorene copolymer systems have advantages such as: often possessing the properties of two monomers, conferring ready tuning of optical properties, facile device fabrication and improved device performance by energy transfer between the two components with different band gaps [5.26–5.28]. To improve the quantum

efficiency, it is very effective to use Förster energy transfer [5.29–5.32]. The energy transfer in blend systems fundamentally requires a sufficient spectral overlap between the emission of the high band gap material and the absorption of the low band gap material and an appropriate intimate morphology of the two species [5.33].

Recently, there has also been a lot of research interest in nanoparticles. The nanoparticles exhibit physical and chemical properties, which are significantly different from their bulk counterpart and can be tailored by controlling the size of these particles [5.34]. Because of the very high surface to volume ratio, nanoparticles are very sensitive to their environment. When coated with polymers, their encapsulation reduces the non-radiative contribution of surface states and enhances consequently the quantum efficiency. Composites of nanoparticles and conjugated polymers are interesting as they enhance the electroluminescence and electrical properties by encompassing the properties of both materials [5.35-5.39].

In this thesis work, PPP is prepared in high yield by oxidative polymerization method from 1,4-dihexyloxy benzene. This method employs mild reaction conditions like room temperature stirring, besides using one of the cheapest and easily available catalysts ($FeCl_3$) and giving desired polymer with high molecular weight and in high yield (80.7%). The molecular weight of PPP is determined by gel permission chromatography (GPC) and is found to be 37360 with a poly dispersity index (PDI) of 1.34. Whereas, PF is prepared by polymerization of 2,7-Dibromo-9,9-dihexyl-9H-fluorene using Suzuki coupling. The formation and purity of the PPP and PF are confirmed by the ^{1}H NMR and ^{13}C NMR. Both these polymers are doped with II-VI and IV-VI nanostructures and their structural, optical, thermal and electrical properties are studied. Both polymers and their blends have shown good optical properties and their electrical conductivity has enhanced several orders of magnitude after incorporation of nanostructured semiconductors.

5.2 Experimental Details

5.2.1 Synthesis of Poly (para-phenylene) (PPP)

a) Synthesis of (1, 4)-dihexyloxy benzene

KOH (8.72 g, 0.155 mol) and dry dimethyl sulfoxide (DMSO, 48 mL) are stirred in an inert atmosphere of N_2 at room temperature for 2 h, followed by addition of hydroquinone (2 g, 0.018 mol) and bromohexane (9.44 mL, 0.072 mol). The reaction mixture is then stirred

for 24 h at room temperature and finally poured into water (500 mL). The organic layer is collected and the aqueous layer is extracted with hexane (4×50 mL). The combined organic layers are dried over anhydrous Na_2SO_4 and filtered. The solvent is evaporated to give a brownish yellow gel. Silica gel chromatography yields white flaky solid.

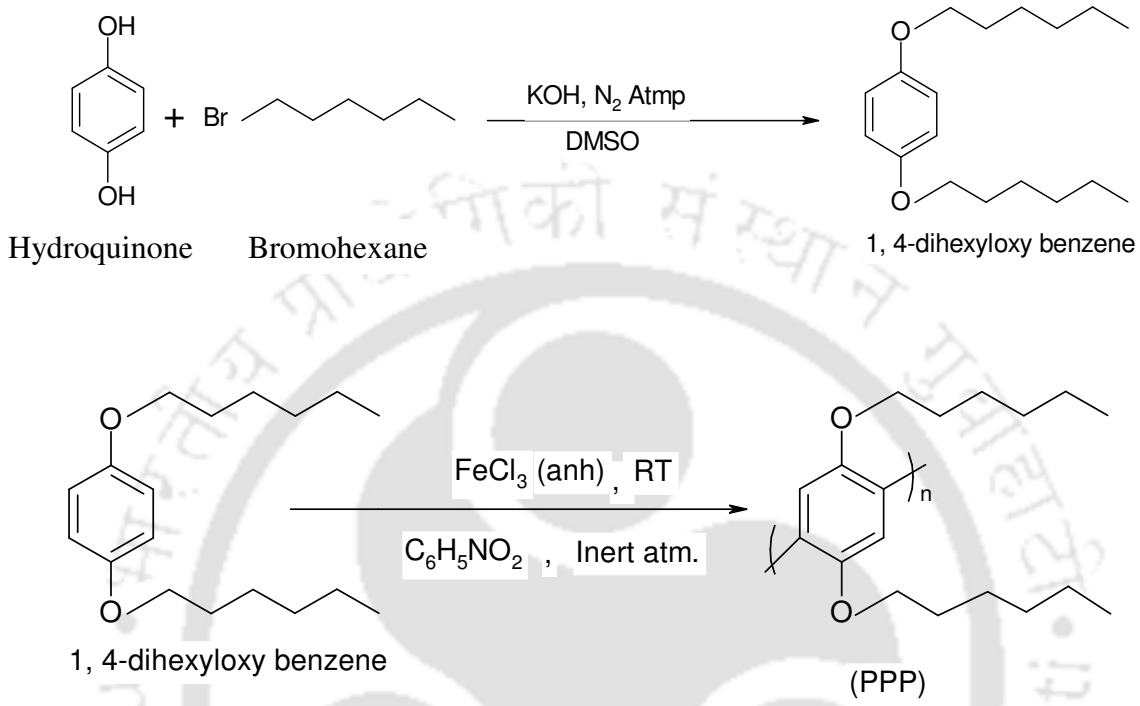

Figure 5.1: Reaction process for the synthesis of PPP.

b) Synthesis of Poly (1, 4-dihexyloxy benzene)

In a 100 mL, three-necked round bottom flask equipped with a nitrogen inlet, anhydrous ferric chloride (0.592 g, 3.64 mmol) is dissolved in 13 mL nitrobenzene. 1,4-dihexyloxy benzene (0.25 g, 0.89 mmol) dissolved in 12.5 mL nitrobenzene is added to the flask by a syringe. The reaction mixture is stirred at room temperature for 36 h, followed by precipitation using ethanol. This mixture is then further stirred for an hour, centrifuged and washed repeatedly with ethanol. The resulting polymer is dried under reduced pressure to give a light brown powder. Gel permeation chromatography (GPC) analysis shows a number-average molecular weight of M_n = 37360 g mol^{-1} and a poly dispersity index (PDI) of 1.34. Thus, polymer with enhanced molecular weight is obtained as compared to those reported in literature [5.20, 5.21].

5.2.2 Synthesis of Polyfluorene (PF)

a) Synthesis of 2, 7-Dibromo-9, 9-dihexyl-9H-fluorene

2,7-Dibromofluorene (1 g, 3.1 mmol), 1-bromohexane (1.26 g, 7.7 mmol), sodium hydroxide (730 mg, 13 mmol), and tetra butyl ammonium iodide (TBAI, 50 mg, 0.3 mmol) are suspended in 50 mL of water and heated at 60 °C for 24 h. The solvent is removed by using a rotary evaporator. The crude product is suspended in chloroform, washed with water, dilute acetic acid, then twice more with water, and then purified by column chromatography on silica using hexane as the mobile phase.

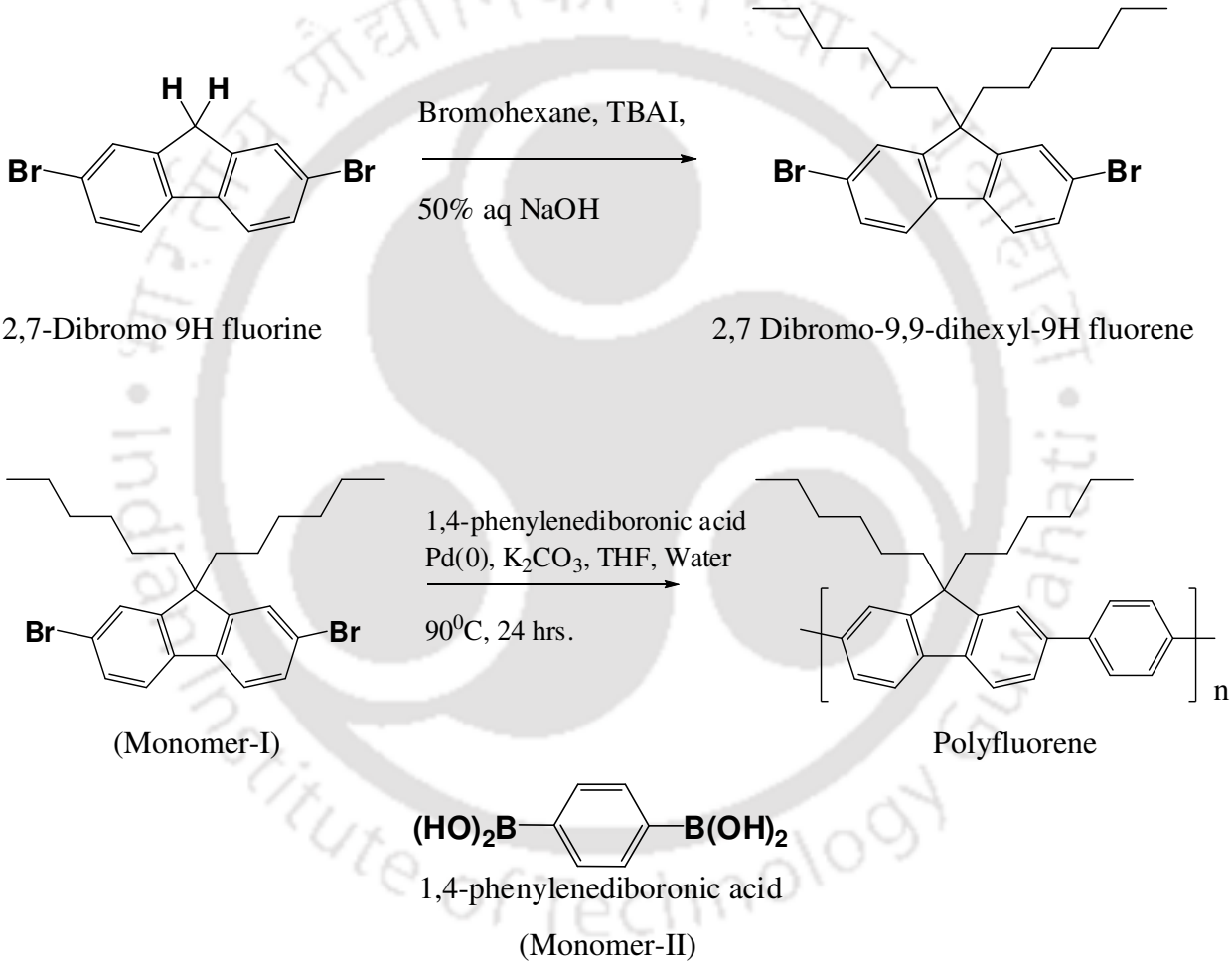

Figure 5.2: Reaction process for the synthesis of PF.

b) Synthesis of Poly (2, 7-Dibromo-9, 9-dihexyl-9H-fluorene)

In a 100 mL three-necked round bottom flask equipped with a nitrogen inlet, Pd(0) and K_2CO_3 is dissolved in 50 mL tetrahydrofuron (THF) and water solutions. 2,7-Dibromo-

9,9-dihexyl-9H-fluorene (0.25 g, 0.89 mmol) and 1,4-phenylenediboronic acid is added in the above solutions. This mixture is stirred for 24 h at 90 °C and then centrifuged and washed repeatedly with ethanol. The resulting polymer is dried under reduced pressure to give a light brown powder.

5.2.3 Synthesis of CdS Nanoparticles

CdS nanoparticles are synthesized by aqueous media process. To synthesize CdS nanoparticles, cadmium acetate (0.637 g, 0.0024 mol) is poured in 100 mL distilled water and stirred for 10 min, followed by H_2S gas purging for 3 h. A yellow precipitate is obtained which is washed several times by distilled water followed by centrifugation. The yellow powder is collected and dried in a vacuum desiccator for 3 h. CdS nanoparticles are formed as per the following chemical reactions.

$$FeS + H_2SO_4 \rightarrow FeSO_4 + H_2S\uparrow$$

$$(CH_3COO)_2Cd.H_2O + H_2S + H_2O \rightarrow CdS\downarrow + CH_3COOH + H_2O$$

5.2.4 Characterizations

a) PPP incorporated with CdS Nanoparticles

As-synthesized PPP, CdS nanoparticles and their blends are characterized by ^{1}H and ^{13}C NMR, GPC, XRD, TEM, SEM and EDAX, UV-Vis optical absorption and PL. Thermal stability is carried out by TGA. To study the structural and optical properties of the CdS nanoparticles doped PPP, 12 mg of PPP is dissolved in 25 mL of tetrahydrofuran (THF). CdS (0.1 to 1.0 equivalent) is added to 2.5 mL of PPP solution, which is sonicated for 1 h and stirred further for 24 h to uniformly disperse the CdS nanoparticles in PPP matrix. UV-Vis and PL measurements are performed on these composite solutions. For SEM studies, thin film of CdS doped PPP is deposited on glass substrates by drop casting technique. For the preparation of sample (CdS nanoparticles doped PPP) for TGA, 0.5 mg of PPP is taken in 1 mL of THF and sonicated for 10 min. CdS nanoparticles (0.5 mg) is added to this solution and the mixture is stirred for 24 h. Finally solvent is evaporated from the solution to get the desired dry sample. The electrical transport properties for these composites are measured by preparing thin films on a glass substrate by drop casting technique (1:1 w/w of CdS and PPP in THF is taken). Conductivity of the CdS doped PPP thin films are measured in the

temperature range from 333–473 K. Evaporated nickel electrodes are used as electrical contacts (with electrode gap = 2 mm and length = 2 cm) in a coplanar geometry. The samples are mounted inside a metallic chamber with a transparent window. All the measurements are performed in high vacuum.

b) PF incorporated with Semiconducting Nanoparticles

As-synthesized PF is characterized by ^{1}H and ^{13}C NMR, GPC, XRD, TEM, SEM and EDAX, UV-Vis optical absorption and PL. To study the structural and optical properties of the PF incorporated with CdS, ZnS, SnS and PbS nanostructured (syntheses process of these nanostructured are described in Chapter 2, subsection 2.2.1), 10 mg of PF is dissolved in 1 mL of chloroform in five separate vial. CdS (5 mg), ZnS (5 mg), SnS (5 mg) and PbS (5 mg) is added to 1 mL of PF solution separately, which is sonicated for 3 h to uniformly disperse the nanoparticles in PF matrix. UV-Vis absorbance, transmittance and PL measurements are performed on these composite solutions. For TEM studies, each of these composite solutions is drop casted on carbon coated Cu grids. For SEM studies, thin films of PF incorporated with nanostructured semiconductors are deposited on Al foil wrapped on glass substrates by drop casting technique. I-V characteristics for the pure PF and its nanostructure blends are measured at room temperature by preparing thin films on ITO coated glass substrates by drop casting technique (1:2 w/w of nanoparticles and PF in chloroform are taken). Evaporated Al electrodes are used as top electrode (with 3 mm diameter) and ITO is used as a bottom electrode in sandwich geometry. The samples are mounted inside a metallic chamber with a transparent window. All the measurements are performed in high vacuum.

5.3 Results and Discussions

5.3.1 PPP and its Nanomaterials Blends

a) Structural Properties

The powder XRD patterns of PPP and CdS nanoparticles are shown in Figure 5.3. PPP is found to be purely amorphous in nature, whereas CdS nanoparticles exhibit several diffraction peaks with varying FWHM. The observed peak positions for these nanoparticles are same as that for bulk CdS having a wurzite structure with lattice parameters ($a = b =$ 4.132 Å and $c = 6.734$ Å). The average particle size of CdS nanoparticles as calculated by Scherrer's formula is 8-10 nm.

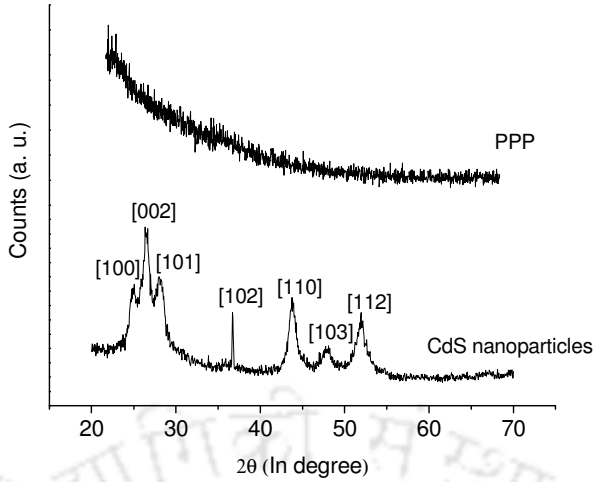

Figure 5.3: XRD patterns of the pure PPP and CdS nanoparticles powder samples.

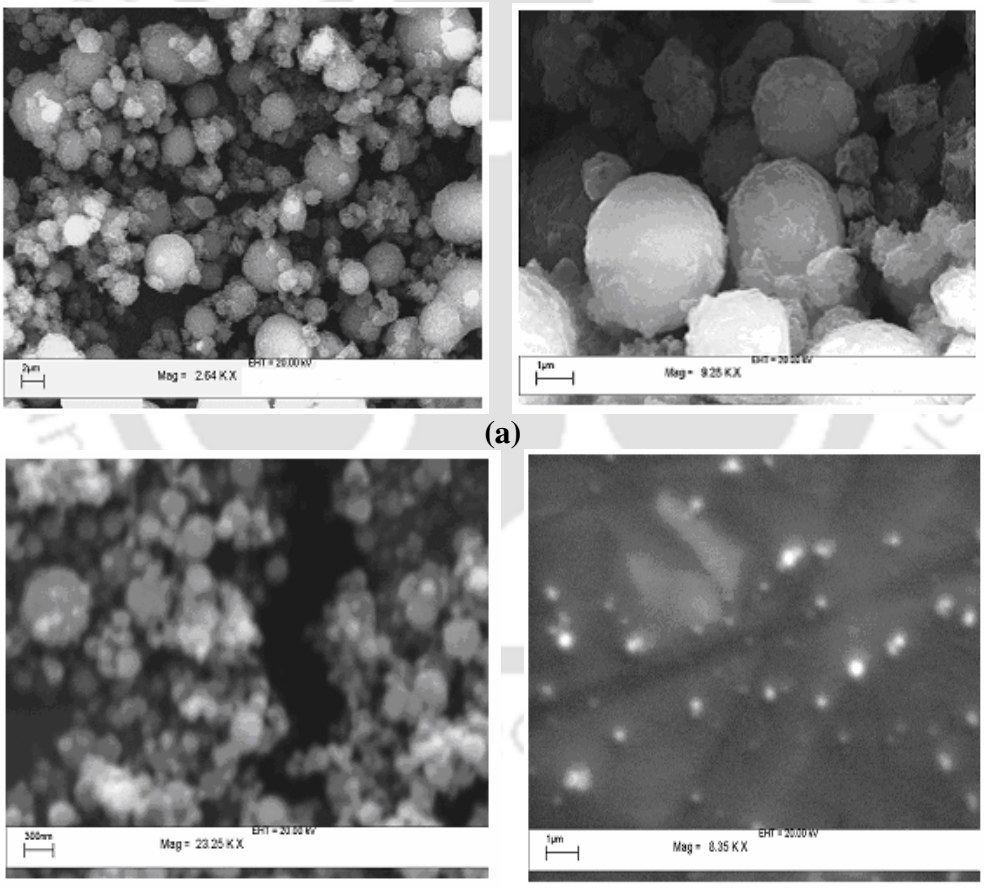

Figure 5.4: SEM images of (a) pure PPP powder sample, (b) CdS nanoparticles powder sample and (c) CdS nanoparticles doped PPP thin film.

SEM images (Figure 5.4) show the uniform spherical balls of the PPP powder and of the CdS nanoparticles. The chemical purity and stoichiometric ratio of the as-synthesized PPP and CdS nanoparticles are determined from the EDAX. The spectrum of CdS nanoparticles show the presence of only Cd and S (stoichiometric ratio 51.25:48.75) signifying the chemical purity of the compound. The particle size of the PPP and CdS nanoparticles varies in the range of 1-3 μm and 20-30 nm respectively. SEM image of CdS doped PPP thin film (Figure 5.4c), suggests that CdS nanoparticles are uniformly dispersed in PPP matrix.

b) Optical Properties

Figure 5.5 represent the UV-Vis absorption spectra of pure PPP, CdS nanoparticles and their composites. PPP and CdS are ultrasonically dispersed in THF to record the absorption spectra in the range of 200-800 nm. Pure PPP (Figure 5.5a) shows a broad absorption peak at 373 nm (FWHM= 77.17 nm). The corresponding band gap is 3.32 eV. Absorption spectrum of CdS (Figure 5.5b) is similar to its bulk counterpart. The absorption increases with energy of photons. An onset of absorption is observed at 490 nm (corresponding E_g = 2.53 eV) which is slightly higher than bulk CdS (E_g = 2.41 eV). This blue shift in absorption is due to reduced size of nanoparticles. Absorption spectra of CdS doped PPP solution is shown in Figure 5.5c for different ratio of CdS-PPP. It is observed that as the concentration of CdS increases, the absorption increases linearly (Figure 5.5d), although no shift in peak position has been observed. A linear dependence of absorbance on CdS concentration is in accordance with the Beer-Lambert's law.

The room temperature photoluminescence (PL) spectra of the PPP, CdS nanoparticles and their composites are presented in Figure 5.6. PPP and CdS are ultrasonically dispersed in THF to record the PL spectra. The emission spectrum for the pure PPP (Figure 5.6a) measured at room temperature using 378 nm excitation shows emission maxima at 426 nm (corresponding band gap is 2.91 eV). The PL spectrum (Figure 5.6b) for the CdS nanoparticles (400 nm of excitation) gives a sharp emission peak at 529 nm (corresponding band gap is 2.34 eV). Figure 5.6c shows the PL-titration spectra for CdS doped PPP solutions (different concentrations) with excitation wavelength of 378 nm. As CdS nanoparticles are added to the PPP solution, the intensity of PL emission peak quenches significantly. The decrease in intensity is more for higher CdS concentration. This may be a result of static quenching [5.40]. The absorption spectra of CdS overlap the emission spectrum of PPP.

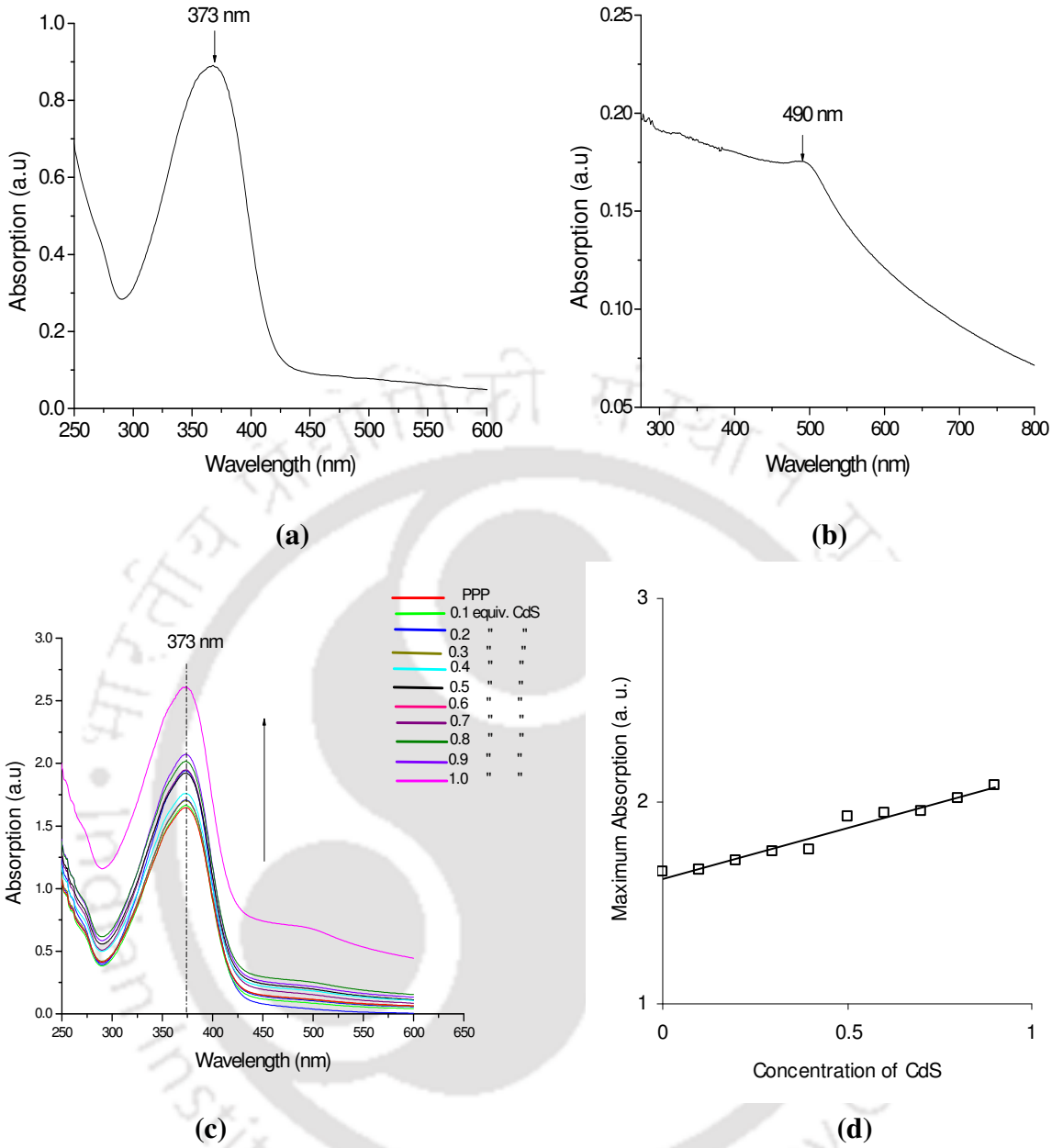

Figure 5.5: UV-Vis absorption spectra of (a) pure PPP solution, (b) CdS nanoparticles solution, and (c) UV-Vis titration spectra of CdS nanoparticles doped PPP solution and (d) Variation of maximum absorption (at 373 nm) with the concentration of CdS nanoparticles.

Thus there is transfer of energy from PPP to CdS nanoparticles. As the concentration of CdS increases, the transfer of energy is more, this reduces the intensity of emission significantly. A linear dependence (Figure 5.6d) of the maximum intensity on the concentration of CdS further confirms this transfer of energy between the PPP and CdS nanoparticles. This observation is similar to that reported by Liang *et al.* for BSA/CdS [5.41].

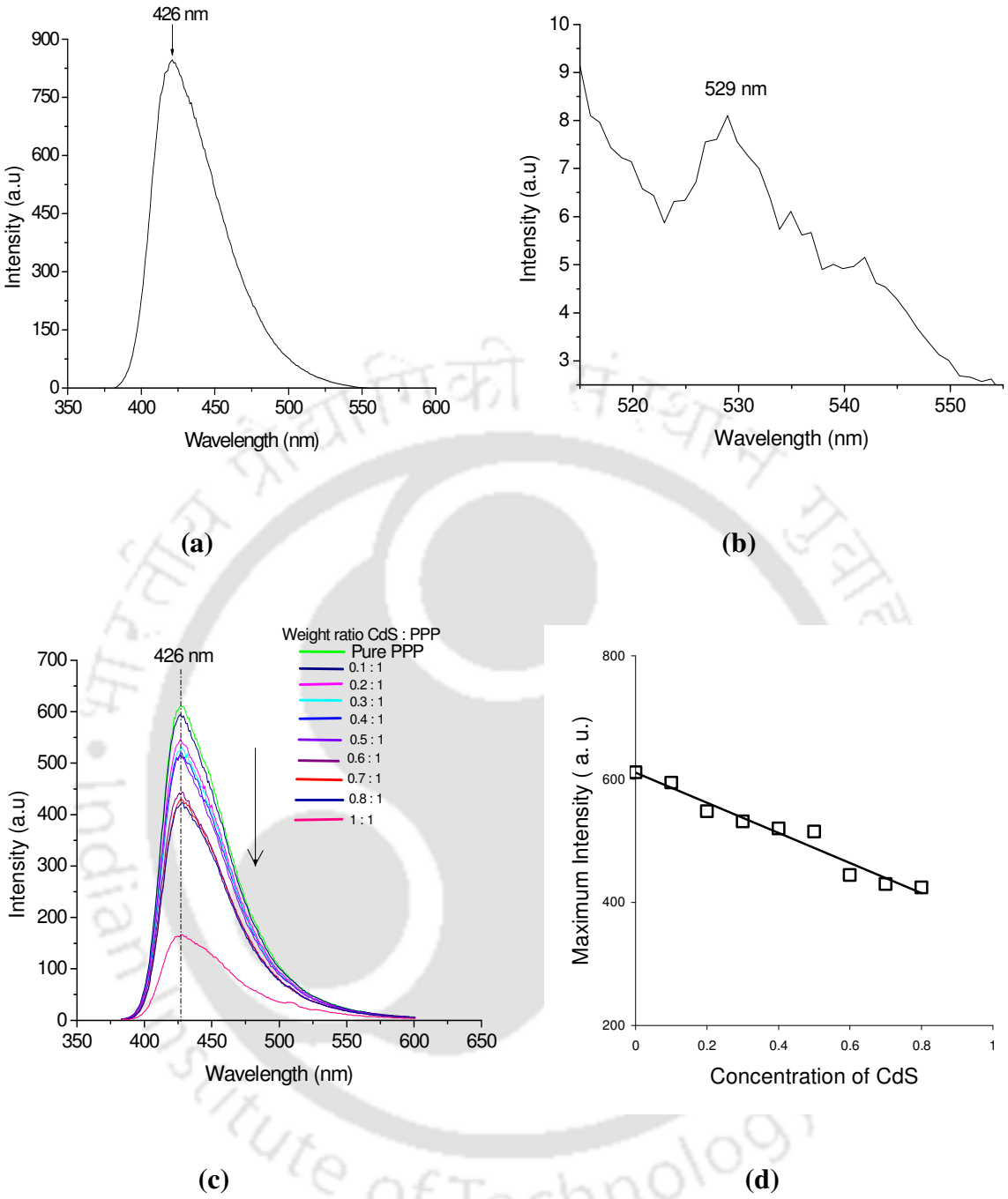

Figure 5.6: Photoluminescence spectra of (a) pure PPP solution, (b) CdS nanoparticles solution and (c) PL-titration spectra of the CdS nanoparticles doped PPP and (d) Variation of intensity maxima with the concentration of CdS nanoparticles.

c) Thermal Stability Studies

The thermal stability studies on pure PPP, CdS nanoparticles and their composites are done by performing TGA (Figure 5.7) in the temperature range of 25-600 ºC for PPP and 25-900 ºC for both CdS nanoparticles and CdS doped PPP (1:1 *w/w*) at a heating rate of 10

ºC/min in inert atmosphere of Ar. PPP is found to be thermally stable up to 325 ºC (Figure 5.7a) and after which a gradual degradation is observed due to the step-by-step polymer breakdown with total decomposition at 600 ºC. 35% weight loss is observed

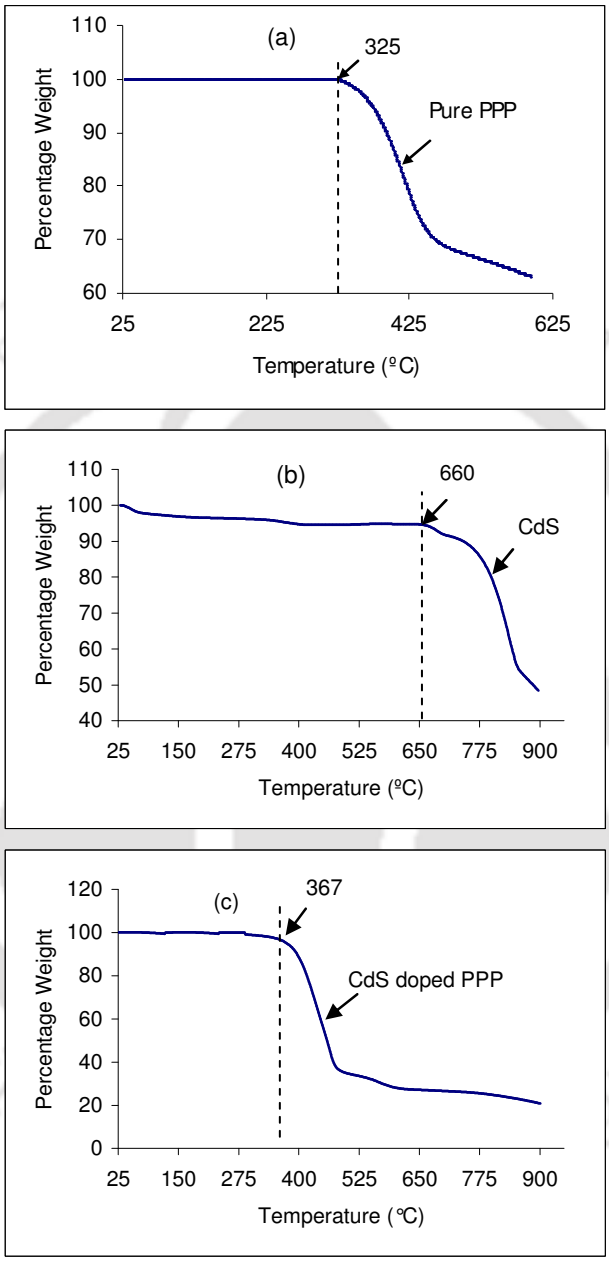

Figure 5.7: Thermo gravimetric analysis of (a) pure PPP powder, (b) CdS nanoparticles powder and (c) CdS nanoparticles doped PPP composites.

from 325-600 ºC temperature range. In case of CdS nanoparticles no weight loss of material up to 660 ºC suggests that (Figure 5.7b) the synthesized CdS nanoparticles are completely dry and highly stable up to nearly 660 ºC. A sharp fall after 660 ºC is observed and about 50%

weight loss is calculated at 900 ºC, which is basically due to the decomposition in to Cd and S from the broken CdS bond. TGA of the CdS doped PPP (Figure 5.7c) show enhanced thermal stability of up to 367 ºC, as compared to the virgin PPP (325 ºC) thus indicating that the thermal stability of PPP can be enhanced by adding specific dopants like CdS nanoparticles.

Kinetic information like thermal activation energy (E), Arrhenius parameter (A) and entropy of activation (ΔS) of the pure PPP, CdS nanoparticles and their blends are also obtained by Coats-Redfern model (Figure 5.8, Chapter 2, subsection 2.4.3) and the results are summarized in Table 5.1. For Coats-Redfern model, the best fits are obtained for g(α) = [-ln (1-α)] = kt, where k is the Boltzmann's constant and t is the time. This relation corresponds to random nucleation with one nucleus on each particle.

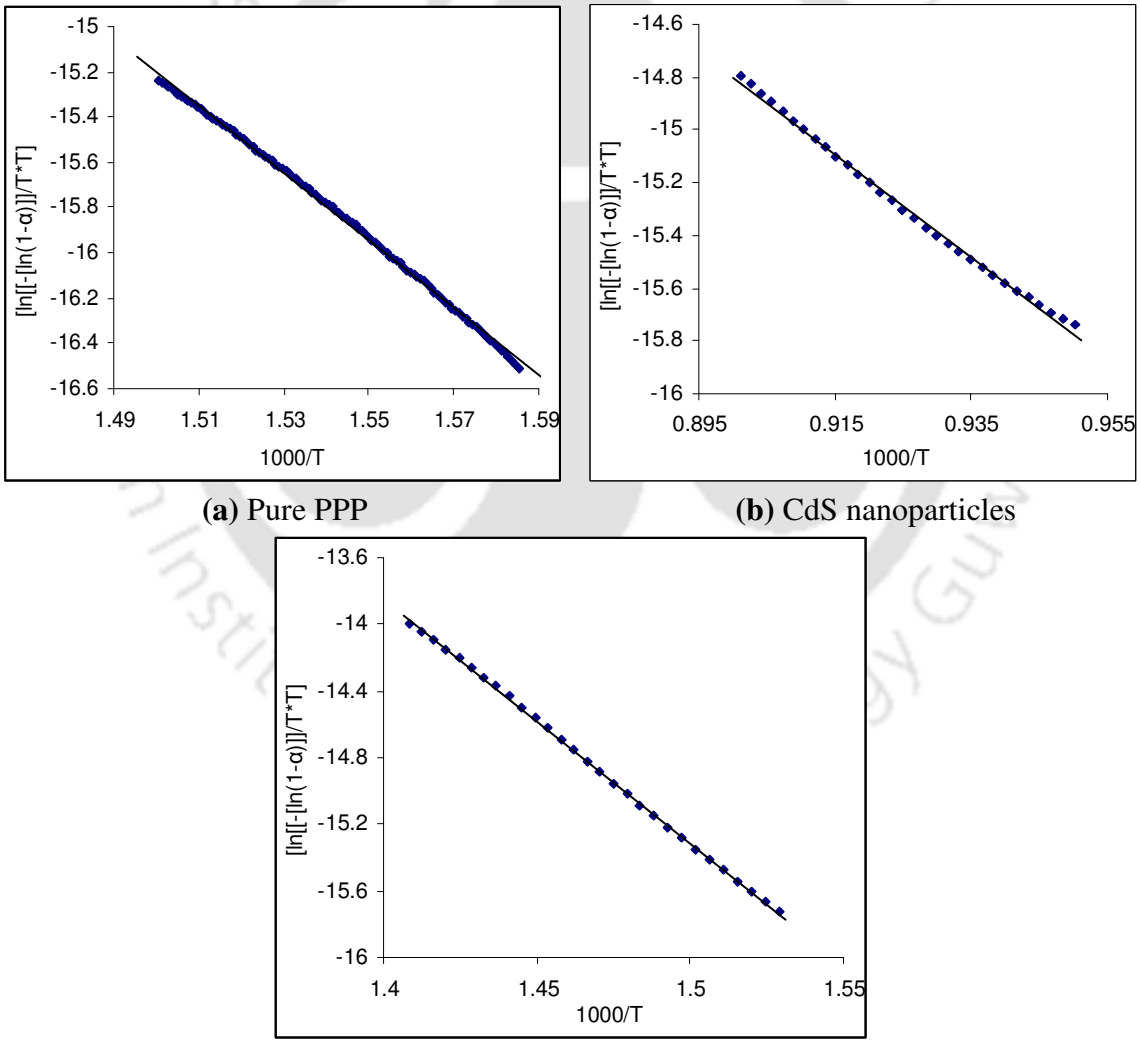

(a) Pure PPP **(b)** CdS nanoparticles

(c) PPP-CdS blend

Figure 5.8: Determination of kinetic parameters of (a) pure PPP, (b) CdS nanoparticles and (c) CdS doped PPP by Coats-Redfern model.

Table 5.1: Kinetic parameters of the PPP, CdS nanoparticles and CdS doped PPP powder samples

Sample	Coats-Redfern model		
	Activation energy E (kJ/mol)	Arrhenius parameters A (s^{-1})	Entropy ΔS (J/degree/mol)
PPP	124	3270	-76
CdS	162	2520	-107
PPP-CdS	122	2004	-80

d) Electrical Transport Studies

Figure 5.9 show the conductivity and I-V measurements on thin films of CdS nanoparticles and CdS doped PPP (1:1 *w/w*) which are investigated in vacuum. The temperature dependence of conductivity follows Arrhenius behavior,

$$\sigma = \sigma_0 \exp(-E_a/kT)$$

where E_a denotes the thermal activation energy of electrical conduction, σ_0 is a parameter depending on the material nature and k represents Boltzmann's constant. From Figure 5.9a it is observed that both dark and photoconductivity of the CdS nanoparticles thin films are thermally activated with single activation energy in the entire temperature range. The activation energy of dark and photoconductivity (under illumination of 10 mW/cm^2) is 0.21 eV and 0.16 eV respectively. The virgin PPP films are found to be highly insulating ($\sigma \approx 10^{-13}$ Ω^{-1} cm^{-1}) near room temperature. When doped with CdS nanoparticles, conductivity is enhanced by several orders of magnitude near room temperature. The activation energy for CdS doped PPP (Figure 5.9b) in the range 333 to 403 K is 0.68 eV, which decreases to 0.08 eV beyond this 413-473 K temperature when σ reaches 10^{-4} Ω^{-1} cm^{-1}. A small change in conductivity is observed when light from halogen lamp (10 mW/cm^2) is illuminated on these films. The change is not large as the absorption maxima of these doped polymer film is at 373 nm, which falls within the UV range and the halogen lamp has negligible flux of UV photons. The I-V characteristics of the CdS nanostructured thin films (Figure 5.9c) and CdS doped PPP (Figure 5.9d) are also measured to study the metal-semiconductor junctions. It is observed that I-V curves are straight lines and go through the origin, which suggest that metal-semiconductor junctions are ohmic in nature.

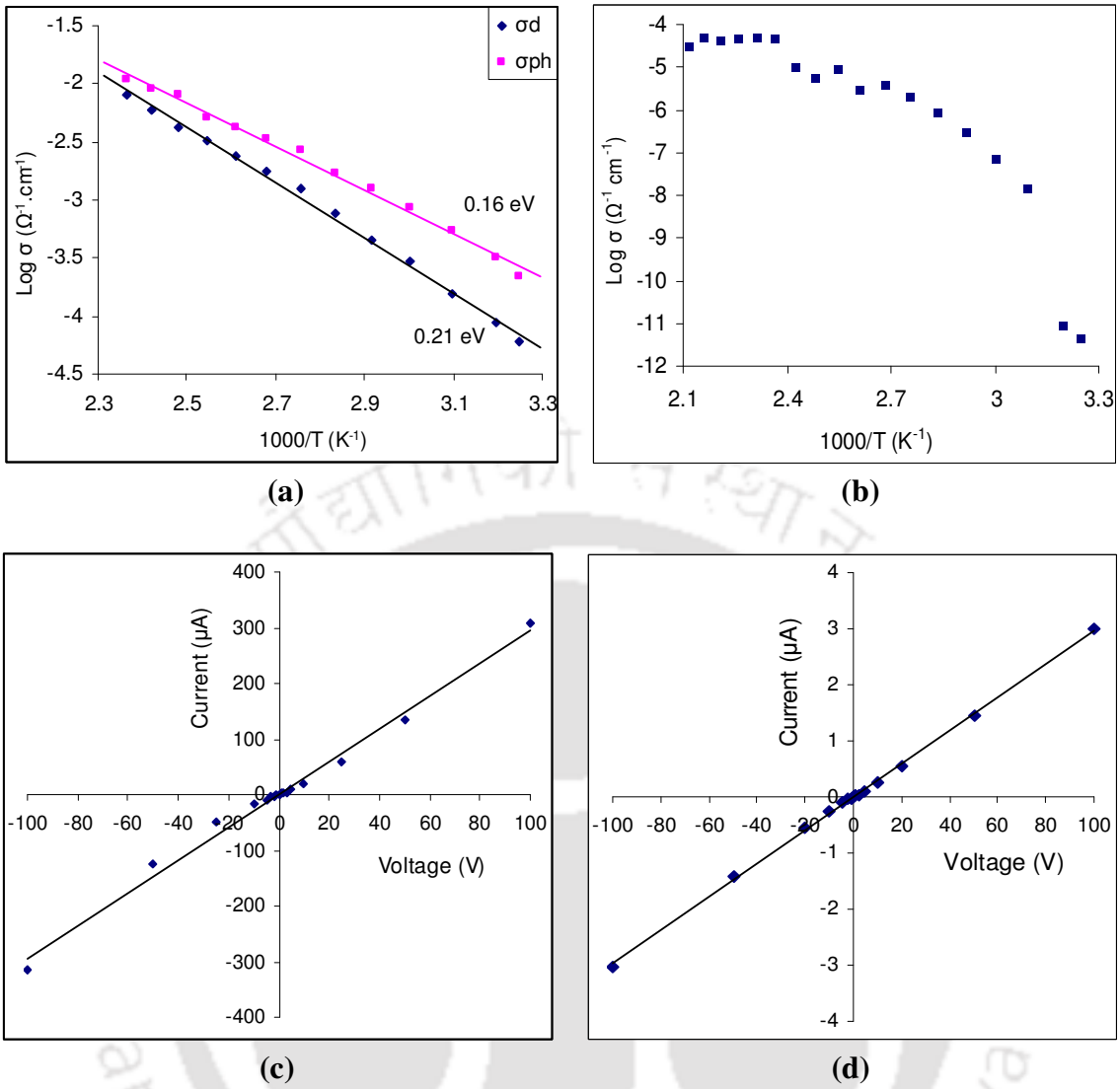

Figure 5.9: (a) Dark and photoconductivity of CdS nanoparticles, (b) Dark conductivity of the CdS nanoparticles doped PPP, (c) I-V curve of CdS nanoparticles at 150 °C and (d) I-V curves of CdS doped PPP at 100 °C.

5.3.2 PF and its Nanomaterials Blends

Polyfluorene constitute a family of interesting organic semiconductors for application in light emitting diodes (LEDs). They display electroluminescence (EL), photoluminescence (PL) and a high ionization potential. Pure polyfluorene is totally soluble in chloroform and produce bright yellow solution. Color of this solution changes when CdS, ZnS, SnS and PbS nanostructured materials are incorporated in PF (Figure 5.10) which could be due to the attachment of nanomaterials with the side chains of the polymer.

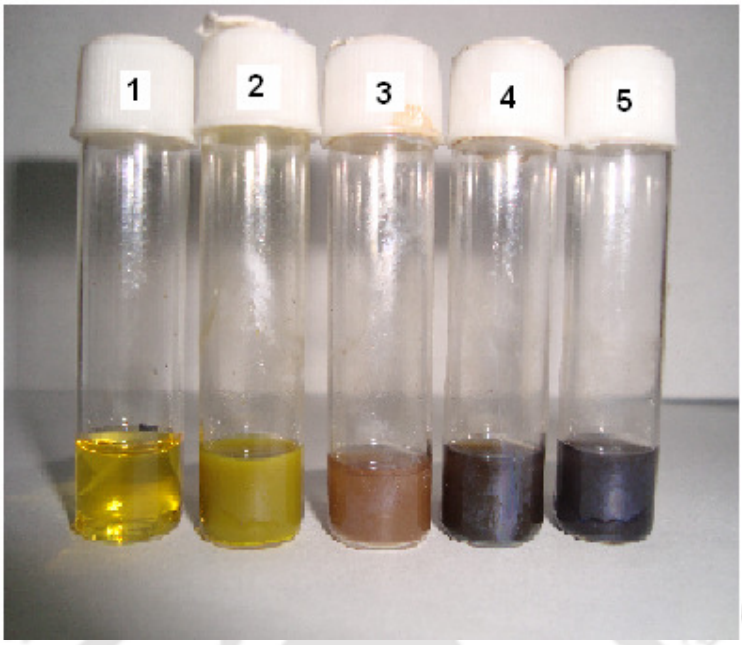

Figure 5.10: (1) Pure PF, (2) PF blend with CdS nanorods, (3) PF blend with ZnS disc like nanoparticles, (4) PF blend with SnS nanoflakes, (5) PF blend with PbS nanocubes in chloroform solvent.

a) Structural Properties

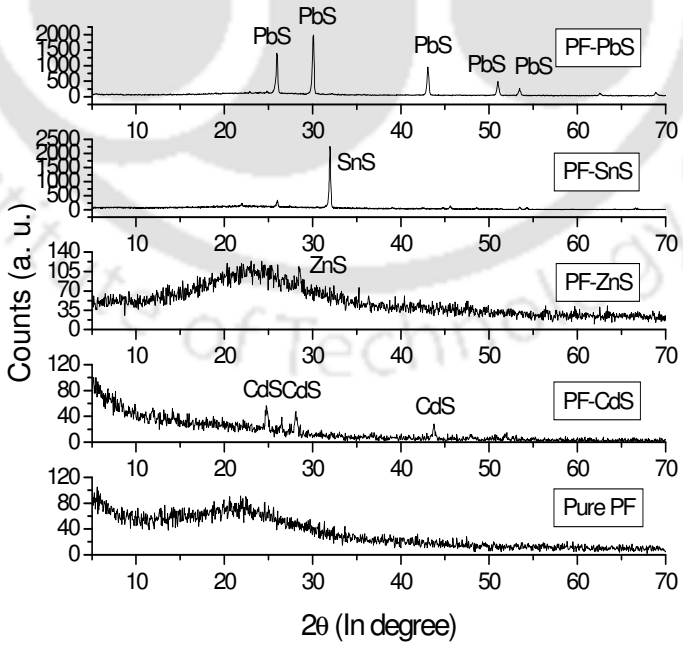

Figure 5.11: XRD patterns of PF and its nanocomposites blend thin films.

Figure 5.11 show the XRD patterns of the PF and its nanostructured blends thin films. Pure PF thin film shows a broad diffraction pattern, which is basically due to the amorphous nature of the conjugated polymer. XRD pattern of the PF incorporated with nanocomposites thin films show the sharp peaks of the respective nanostructured semiconductors, which suggest that nanoparticles are well dispersed in polymer matrix.

Figure 5.12 show the SEM images of the pure PF and its nanocomposites blend thin films. Figure 5.12a shows the SEM image of the pure PF chains. SEM images show that nanomaterials are well dispersed in polymer matrix and nanomaterials are covered by polymer thin layer.

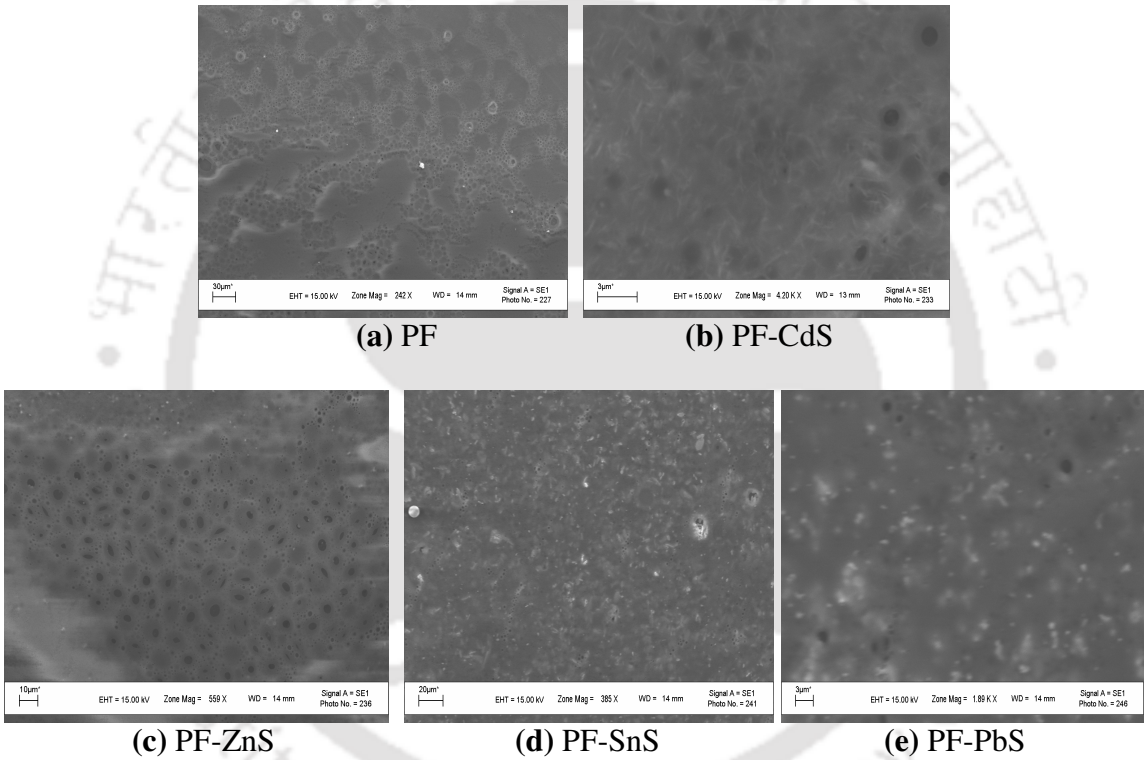

Figure 5.12: SEM images of the PF and its blends with nanocomposites.

TEM images of PF and its nanomaterials blends are presented in Figure 5.13. It is observed that nanostructured materials are encapsulated by polymer.

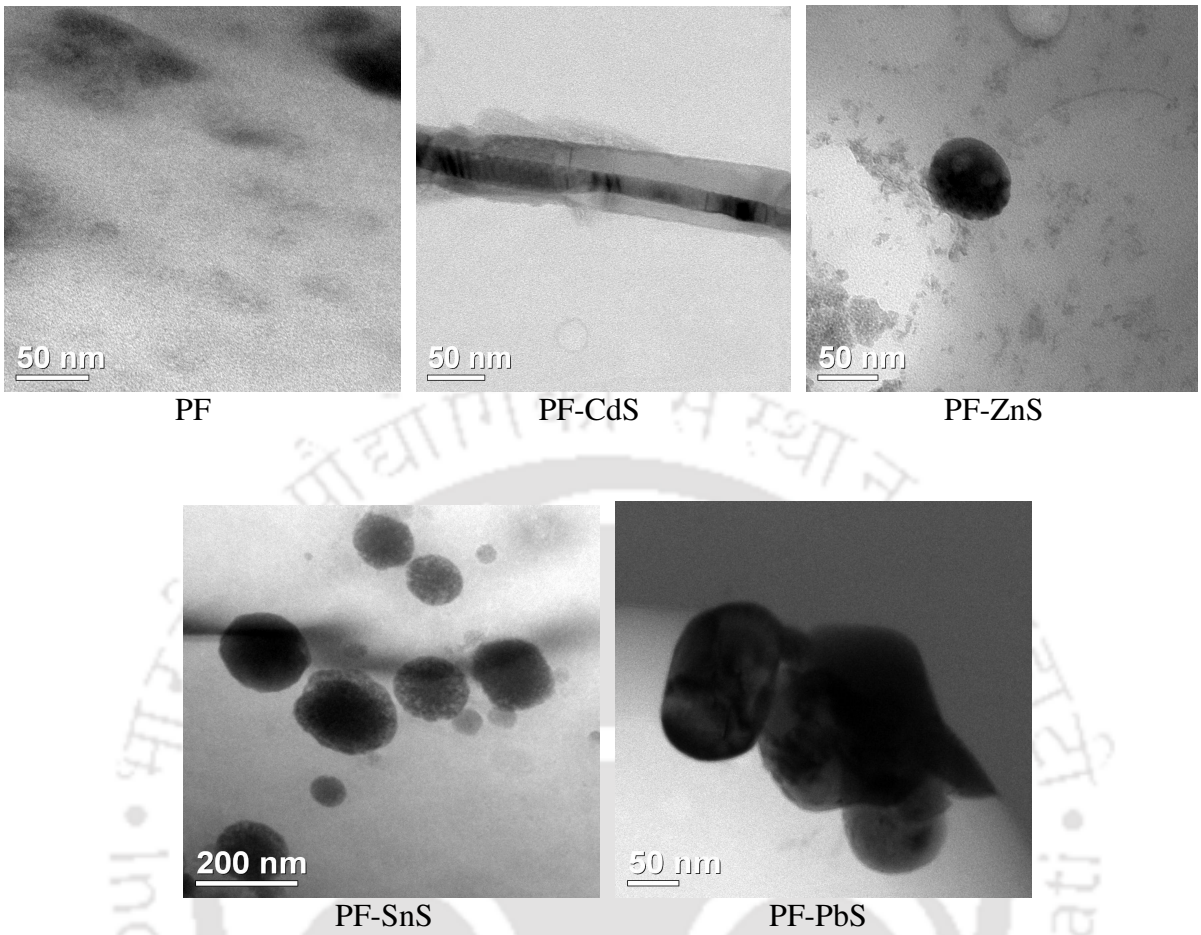

Figure 5.13: TEM images of PF and its nanomaterials blends.

b) Optical Properties

UV-Vis-NIR transmittance spectra of the PF and its nanomaterials blends in chloroform solutions and thin films state are presented in Figure 5.14. Polymer and its nanomaterials blends totally absorb the photons of wavelength below 400 nm.

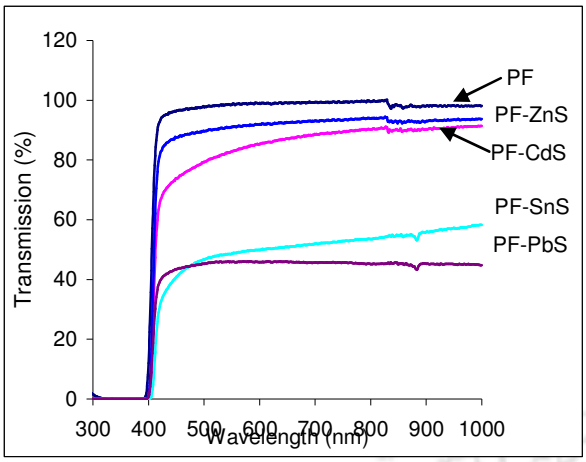

(a)

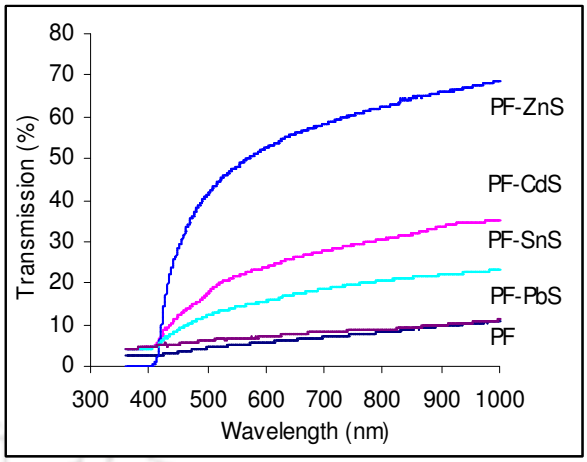

(b)

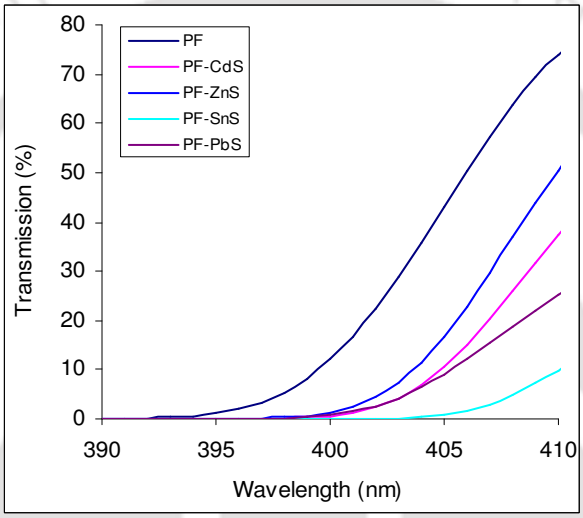

(c) Figure (a) in expanded scale

Figure 5.14: UV-Vis-NIR transmittance spectra (a) Solution in chloroform solvent and (b) Thin films prepared on glass substrates and (c) Figure (a) in expanded scale.

Figure 5.15 show the UV–Vis-NIR absorption spectra of the polymers and its blends with nanocomposites in chloroform solution and in the thin films coated onto the glass slides. Polymer in dilute chloroform solution and in the solid state has shown absorption maxima at 378 and 390 nm respectively. From the onsets of the absorption spectra, the band gap of polymer is calculated to be 3.28 and 3.18 eV for solution and thin film state respectively. The absorption in the range from 378 to 390 nm is due to π-π* transition of conjugated polyfluorene backbone. Onsets of absorption spectra of the PF incorporated with nanostructured materials shifts to 393 nm (corresponding band gap 3.16 eV) in dilute chloroform states where as in thin film states absorption peaks are centered at 390 nm. It is observed that incorporating these different nanomaterials into the fluorene backbone has

substantial effect on the extent of conjugation, resulting in modified electronic transitions and shifts in the absorption peaks.

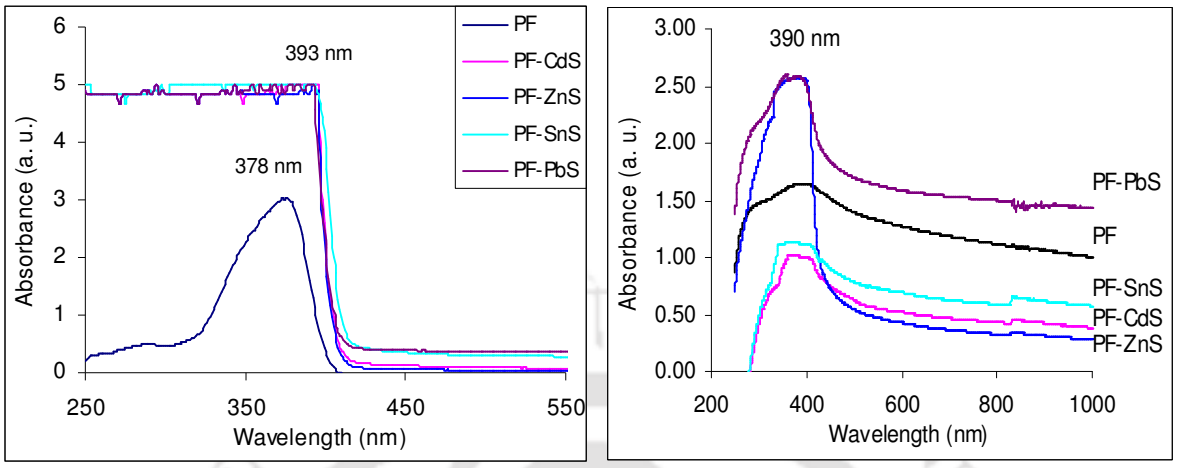

(a) Solution in chloroform **(b)** Thin films

Figure 5.15: UV-Vis absorbance spectra of PF and its nanomaterials blends in (a) solutions and (b) thin films.

The fluorescent wavelength of a polymer fundamentally depends on the band gap between the HOMO and LUMO, which depends on delocalization of π-electrons along the polymer backbone. The characteristic peak in the emission spectrum arises as an excited electron relaxes into vibronic energy level of the HOMO. The optical spectra of conjugated polymers are typically broad, which is due to the coupling of several different vibronic modes. Figure 5.16 reveals the photoluminescence spectra of polymers and its blend with nanocomposites in dilute chloroform solutions and thin films at excitation wavelength of 370 nm. Two peaks are observed at 411 and 433 nm respectively for pure PF dilute chloroform solution. When the polymer is incorporated with semiconducting nanomaterials (like CdS, ZnS, SnS and PbS) the emission peaks are shifted by 2-5 nm. In case of thin films, emission peaks are observed at 421 and 441 nm respectively. In comparison with dilute solutions, the emission spectra of polymers in film state are slightly red-shifted and can be attributed to the aggregation of polymer chains.

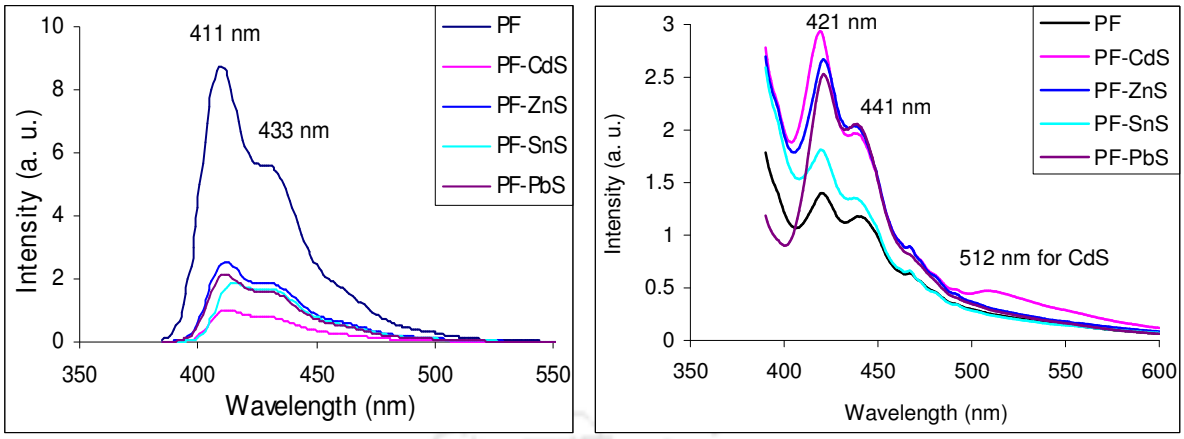

(a) Solutions in chloroform **(b)** Thin films

Figure 5.16: PL spectra of PF and its nanocomposites blends in (a) solutions and (b) thin films.

c) Thermal Stability Studies

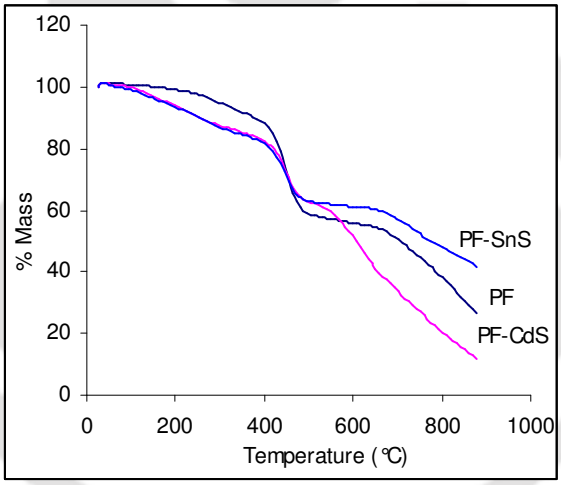

Figure 5.17: Thermo gravimetric analysis of (a) pure PF, (b) CdS nanorods doped PF and (c) SnS nano-flakes doped PF composites at inert atmosphere of Ar.

The thermal stability studies on pure PF and its blend with CdS nanorods and SnS nanoflakes are determined by performing TGA (Figure 5.17). In all the cases a gradual degradation is observed due to the step-by-step polymer breakdown. 74%, 88% and 58% weight loss is observed for pure PF, CdS nanorods doped PF and SnS nanoflakes doped PF respectively after 900 °C.

Kinetic information like thermal activation energy (E), Arrhenius parameter (A) and entropy of activation (ΔS) of the pure PF and its blends with CdS nanorods and SnS nano-flakes are obtained by Coats-Redfern model (Figure 5.18) and the results are summarized in Table 5.2. For Coats-Redfern model, the best fits are obtained for $g(\alpha) = [-\ln (1-\alpha)] = kt$, where k is the Boltzmann's constant and t is the time. This relation corresponds to random nucleation with one nucleus on each particle.

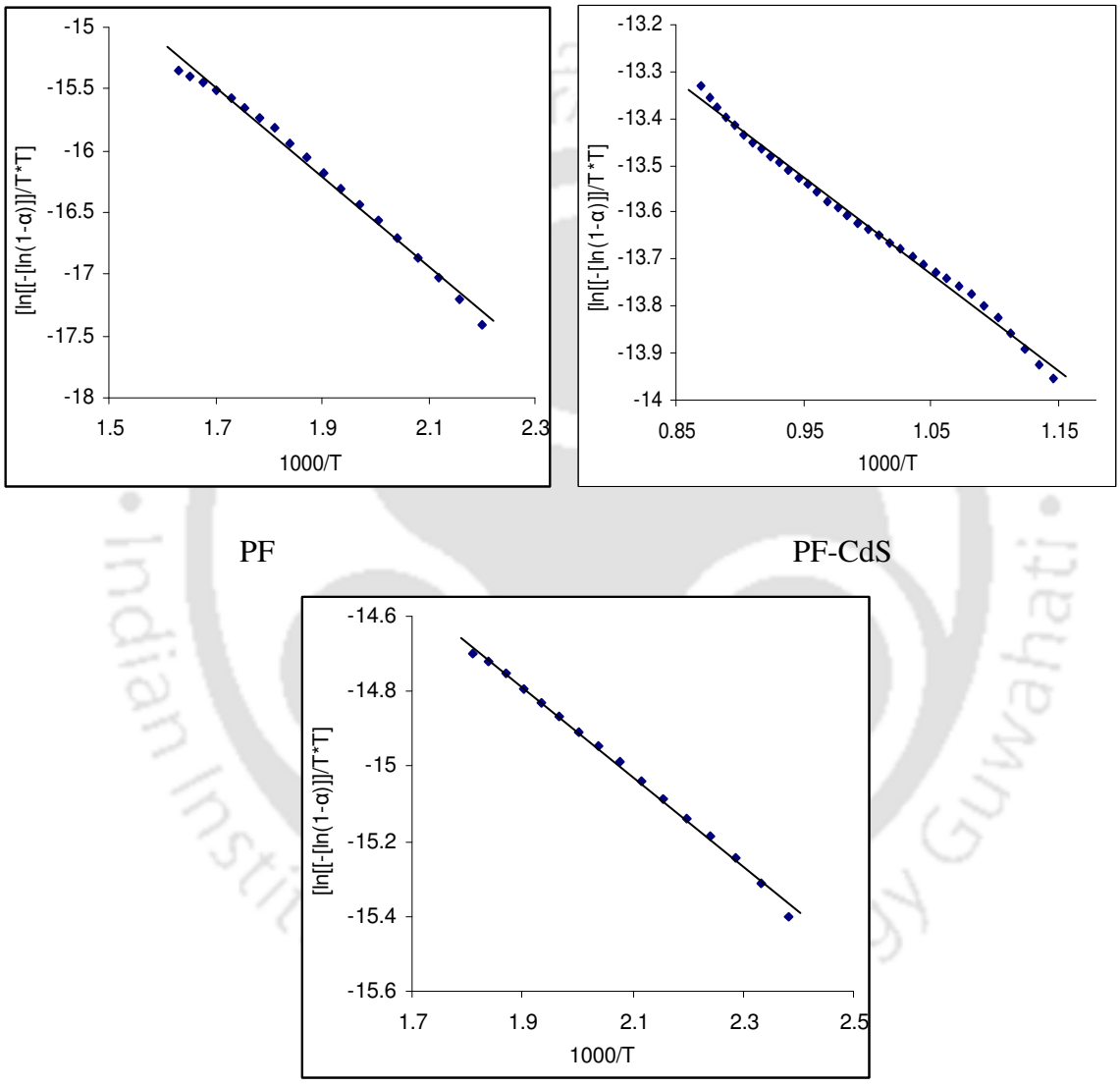

Figure 5.18: Determination of kinetic parameters of (a) pure PF, (b) CdS nanorods doped PF and (c) SnS nano-flakes doped PF obtained by Coats-Redfern model.

Table 5.2: Kinetic parameters of the PF, CdS nanorods doped PF and SnS nanoflakes doped PF powder samples

Sample	Coats-Redfern model		
	Activation energy E (kJ/mol)	Arrhenius parameters $Ax10^3$ (s^{-1})	Entropy ΔS (J/degree/mol)
PF	30	6.7	-70
PF-CdS	17	36.3	-56
PF-SnS	10	54.3	-52

d) Electrical Transport Properties

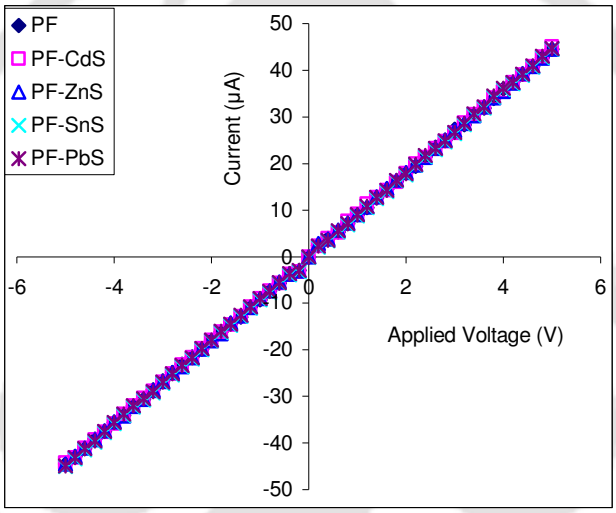

Figure 5.19: I-V characteristics of pure PF and its nanocomposites blends.

I-V characteristics of the pure PF and its nanomaterials blends are presented in Figure 5.19. For all the samples, I-V curves are straight lines and go through the origins which suggest that the junction of the evaporated Al and polymer and its nanocomposites blends behave ohomic nature. Pure PF shows conductivity around 2.8 x 10^{-11} Ω^{-1} cm^{-1} at 300 K. After incorporation of nanostructured materials in PF matrix the dark conductivity of their blends increases slightly. No photoconductivity is observed in PF and its blends with nanocomposites at room temperature under illumination of 10 mW/cm^2 of incident light.

5.4 Conclusions

In summary, two straightforward, high yielding and economical methods to synthesize PPP and PF are reported. Composites of these polymers and nanoparticles are prepared, that could be processed in the same way as organic polymers. PPP, PF and their blends with nanoparticles show good optical absorption and luminescence spectra. Both polymers and their composites show blue luminescence, which suggest that these materials are suitable for blue LEDs. Nanoparticles doped PPP thin films exhibit high electrical conductivity and better thermal stability than the neat polymers. At room temperature, the conductivity of the pure PF is very low. After incorporation of semiconducting nanomaterials, conductivity of PF is slightly improved. The utility of such composite materials that combines the finest properties of each component has potential applications in a range of optoelectronic devices and sensor materials.

5.5 References

[5.1] J. H. Burroughes, D. D. C. Bradley, A. R. Brown, R. N. Marks, K. Mackay, R. H. Friend, P. L. Burn and A. B. Holmes, Nature **347**, 539 (1990).

[5.2] T. M. Hagler, K. Pakbaz, J. Moulton, F. Wudl, P. Smith and A. J. Heeger, Polym. Commun. **32**, 339 (1991).

[5.3] D. Braun and A. J. Heeger, Thin Solid Films **216**, 96 (1992).

[5.4] D. Braun and A. J. Heeger, Appl. Phys. Lett. **58**, 1982 (1991).

[5.5] G. Yu, J. Gao, J. C. Hummelen, F. Wudl and A. J. Heeger, Science **270**, 1789 (1995).

[5.6] T. Stubinger and W. Brutting, J. Appl. Phys. **90**, 3632 (2001).

[5.7] H. Shinohara, T. Chiba and M. Aizawa, Sens. Actuators **13**, 79 (1988).

[5.8] P. Görrn, T. Rabe, T. Riedl, W. Kowalsky, F. Galbrecht and U. Scherf, Appl. Phys. Lett. **89**, 161113 (2006).

[5.9] W. S. Schlindwein, Y. Gofer, H. Sarker, T. O. Poehler and P. C. Searson, J. Electroanal. Chem. **460**, 46 (1999).

[5.10] J. L. Bredas, R. R. Chance and R. Silbey, Phys. Rev. B **26**, 5843 (1982).

[5.11] T. P. Nguyen and V. H. Tran, Mater. Sci. Eng. B **31**, 255 (1995).

[5.12] T. Sata, Y. Ishii, K. Kawamura and K. Matsusaki, J. Electrochem. Soc. **146**, 585 (1999).

[5.13] N. R. Anderson, B. R. Mattes, H. Reiss and K. B. Kanner, Synth. Met. **41**, 1151 (1991).

[5.14] D. M. Ivory, G. G. Miller, J. M. Sowa, L. W. Shacklette, R. R. Chance and R. H. Baugham, J. Chem. Phys. **71**, 1506 (1979).

[5.15] J. Fink, B. Scheerer, M. Stamm, B. Tieke, B. Kanellakopuolos and E. Dornberger, Phys. Rev. B **30**, 4867 (1984).

[5.16] Z. Yang and H. J. Geise, Synth. Met. **47**, 95 (1992).

[5.17] G. Crecelius, M. Stamm, J. Fink and J. J. Ritsko, Phys. Rev. Lett. **50**, 1498 (1983).

[5.18] C. Seoul, W. J. Song, G. W. Kang and C. Lee, Synth. Met. **130**, 9 (2002).

[5.19] G. Grem, G. Leditzky, B. Ullrich and G. Leising, Adv. Mat. **4**, 36 (2004).

[5.20] (a) T. Yamamoto, Y. Hayashi and A. Yamamoto, Bull. Chem. Soc. Jpn. J. Polymer **51**, 2091 (1978). (b) M. Rehahn, A. D. Schluter, G. Wegner and W. Feast, J. Polymer **30**, 1054 (1989). (c) M. Rehahn, A. D. Schluter, G. Wegner and W. Feast, J. Polymer **30**, 1060 (1989). (d) A. D. Schluter, J. Polym. Sci. Part A: Polym. Chem. **39**, 1533 (2001). (e) M. Bouachrine, J. P. Lere-Porte and J. J. E. Moreau, Phosphorus, Sulfur Silicon Relat. Elem. **152**, 265 (1999).

[5.21] R. Miyakoshi, K. Shimono, A. Yokoyama and T. Yokozawa, J. Am. Chem. Soc. **128**, 16012 (2006).

[5.22] A. P. Kulkarni and S. A. Jenekhe, Macromolecules **36**, 5285 ((2003)).

[5.23] U. Scherf and E. J. W. List, Adv. Mater. **14**, 477 (2002).

[5.24] M. Leclerc, J. Polym. Sci. Part A: Polym. Chem. **39**, 2867(2001).

[5.25] L. Akcelrud, Prog. Polym. Sci. **28**, 875 (2003).

[5.26] S. H. Jin, S. Y. Kang, M. Y. Kim, Y. U. Chan, J. Y. Kim, K. Lee and Y. S. Gal, Macromolecules **36**, 3841(2003).

[5.27] G. Klarner, M. H. Davey, W. D. Chen, J. C. Scott and R. D. Miller, Adv. Mater. **10**, 993 (1998).

[5.28] W. Wu, M. Inbasekaran, M. Hudack, D. Welsh, W. Yu, Y. Cheng, C. Wang, S. Kram, M. Tacey, M. Bernius, R. Fletcher, K. Kiszka, S. Munger and J. O'Brien, Microelectron. J. **35**, 343 (2004).

[5.29] R. Gupta, M. Stevenson, M. D. McGehee, A. Dogariu, V. Srdanov, J. Y. Park and A. J. Heeger, Synth. Met. **102**, 875 (1999).

[5.30] A. Dogariu, R. Gupta, A. J. Heeger and H. Wang, Synth. Met. **100**, 95 (1999).

[5.31] L. Ding, F. E. Karasz, Z. Lin, M. Zheng, L. Liao and Y. Pang, Macromolecules **34**, 9183 (2001).

[5.32] T. Virgili, D. G. Lidzey and D. D. C. Bradley, Synth. Met. **111–112**, 203 (2000).

[5.33] T. Forster, Discuss. Faraday Soc. **27**, 7 (1959).

[5.34] C. N. R. Rao, G. U. Kulkarni, P. J. Thomas and P. P. Edwards, Chem. Soc. Rev. **29**, 27 (2000).

[5.35] P. Englebienne and A. Van Hoonacker, J Coll. Inter. Sci. **292**, 445 (2005).

[5.36] C. Dridi, M. Haouari, H. Ben Ouada, A. P. Legrand, J. Davenas, M. Bernard, J. J. Andre, A. Haj Said and F. Mattoussi, Mater. Sci. Eng. C **26**, 415 (2006).

[5.37] W. Qingqing, Z. Gaoling and H. Gaorong, Mater. Lett. **59**, 2625 (2005).

[5.38] Y. Ohara, T. Nakabayashi, K. Iwasaki, T. Torimoto, B. Ohtani and N. Ohta, C. R. Chimie **9**, 742 (2006).

[5.39] A. S. Susha, F. Caruso, A. L. Rogach, G. B. Sukhorukov, A. Kornowski, H. Mohwald, M. Giersig, A. Eychmuller and H. Weller, Colloids Surf. A **163**, 39 (2000).

[5.40] G. Z. Chen, X. Z. Huang and J. G. Xu, "*The analytical methods of fluorescence*", Science Press, Beijing (1990).

[5.41] L. Tan, L. Y. Liu, Q. J. Xie, Y. Y. Zhang and S. Z. Yao, Anal. Sci. **20**, 441 (2004).

CHAPTER-6

Fabrication and Studies of Nano-structured p-SnS/n-CdS Based Heterojunction Solar Cells

CHAPTER 6: Fabrication and Studies of Nano-structured p-SnS/n-CdS Based Heterojunction Solar Cells

6.1 Introduction

Our society is dependent on coal, oil and natural gas as source of energy, but these fossil fuels will be depleted someday in the future because these are limited. In addition, these fossil fuels cause adverse effect on climate due to emission of carbon dioxide (CO_2), resulting in the global warming. Under these circumstances, interest in photovoltaic (PV) solar cell is increasing rapidly as an alternative and clean energy source.

Photovoltaic solar cells provide clean electrical energy because the solar energy is directly converted into electrical energy without emitting CO_2. The solar energy is unlimited, free of charge and distributed uniformly to all human beings. Crystalline silicon solar cell has been extensively studied and used for practical terrestrial applications. However, the expensive material cost and lots of energy necessary for manufacturing these solar cells have caused high cost and long energy payback time, which has prevented the large spread of photovoltaic (PV) power generation and use among common people.

Recently, thin film solar cells using compound semiconductors (like CdS, CdTe, $CuInSe_2$, GaAs, SnS) have been actively studied instead of the bulk silicon solar cell. Among these, tin sulfide (SnS) is one of the promising materials for low cost thin film solar cells, because of a band gap of 1.3~1.4 eV and a fundamental absorption coefficient larger than 10^4 cm^{-1} [6.1]. Undoped SnS films always show p-type conduction and p-n junction has been prepared with n-type materials like CdS. A few research groups have reported the use of SnS thin films deposited by electrochemical, spray pyrolysis or thermal evaporation as absorber components in SnS/CdS solar cells. In the year 1994, Nagouchi *et al*. [6.2] have reported the photovoltaic properties of p-SnS/n-CdS heterojunction solar cells, where CdS and SnS films are prepared by vacuum evaporation technique using evaporated Ag as a back contact. They have observed short-circuit current density (J_{SC}) of 7 mA/cm^2, an open-circuit voltage (V_{OC}) of 0.12 V, a fill factor (FF) of 0.35 and conversion efficiency of 0.29% under the illumination of 100 mW/cm^2. In 2003, another report [6.3] appears on heterojunction solar cell having a photovoltaic structure with brush plated SnS with Voc=370 mV, short circuit current of 780 mA and efficiency 0.63%. Reddy *et al*. [6.4] have prepared the SnS/CdS heterojunctions by spray pyrolysis process. In their cells, thicknesses of both the SnS and CdS layers are

approximately 0.6 μm and a thin layer of indium with a thickness of 0.4 mm is formed on the CdS to act as the top contact. They [6.4] have obtained open-circuit voltage (V_{OC}) of 260 mV, short-circuit current density (J_{SC}) of 9.6 mA/cm^2 and fill factor (FF) of 0.53 under the illumination of 100 mW/cm^2 with conversion efficiency of 1.3% for an area of 0.3 cm^2. For a similar structure, Gunasekaran *et al*. [6.5] have reported the electrochemically deposited SnS thin layers of 2 μm thickness. The cells have shown V_{OC}=270 mV, J_{SC}=2.36 mA/cm^2, fill factor FF=0.35 and efficiency (η) 0.2% for an area of 0.01 cm^2 using evaporated indium (In) contacts. In SnS/CdS heterojunctions reported by Ghosh *et al*. [6.6], the SnS and CdS layers are deposited by thermal evaporation technique. Thicknesses of the SnS and CdS layers are 1 μm and 0.3 μm respectively. They have obtained V_{OC}=260 mV, J_{SC}=9.6 mA/cm^2, FF=0.53 and efficiency of 0.09% for an area of 0.4 cm^2 using Ag paste on the SnS surface to act as the back contact.

In the present thesis work, p-SnS/n-CdS nanostructured based solar cells are prepared by doctor blade technique (discussed in Chapter 2, section 2.3) and their physical parameters like FF, V_{OC}, I_{SC}, series resistance, shunt resistance are obtained. Maximum conversion efficiency of 0.32% (under illumination of 100 mW/cm^2), 166 Ω of series resistance and 2 kΩ of shunt resistance are obtained for the best cell.

6.2 Theory of Solar Cells

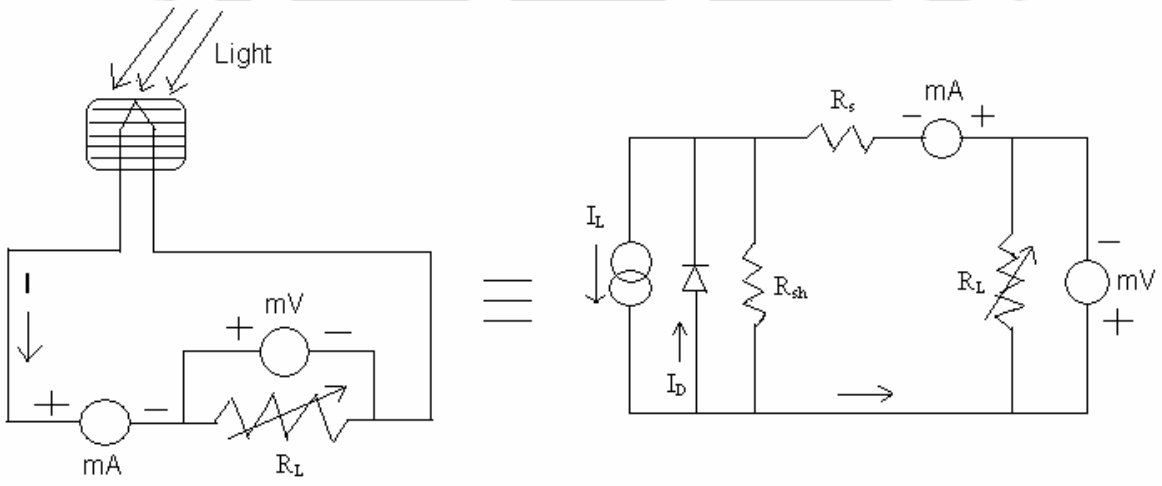

(a) Working circuit **(b)** Equivalent circuit

Figure 6.1: (a) Working circuit and (b) Equivalent circuit of the solar cell.

Equivalent circuit of the solar cell is given in Figure 6.1. Here I_L indicates the current generated under illumination, I_D indicates the current through diode, R_{Sh} and R_S are the shunt

and series resistances respectively of the solar cell. R_L is the load resistance connected with the solar cell.

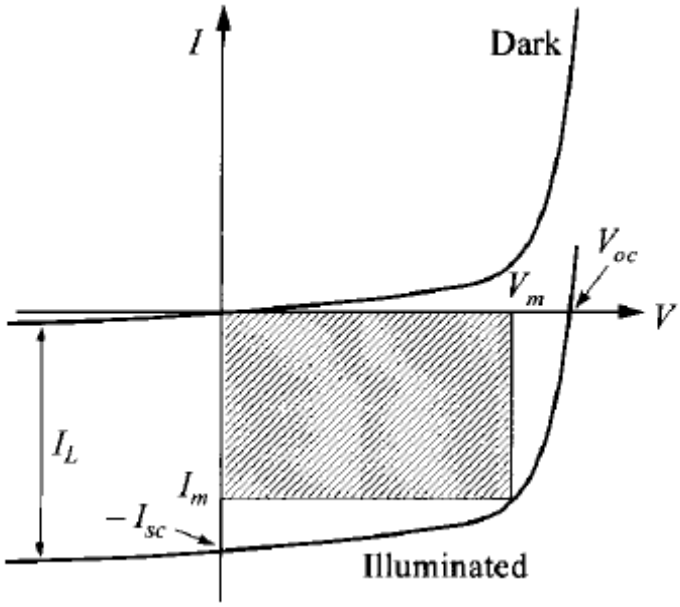

Figure 6.2: I-V characteristics of solar cell under dark and illumination. Determination of maximum power output is indicated [6.7].

Figure 6.2 shows the current-voltage (I-V) characteristics of the typical solar cell under dark and illumination at room temperature. The diode equation of the thin film solar cell under illumination condition corrected for series resistance (R_s) and shunt resistance (R_{sh}) can be represented as

$$I = I_0\left[\exp\frac{q(V-IR_s)}{nkT}-1\right]-\frac{V-IR_s}{R_{sh}}-I_L \quad \ldots\ldots\ldots\ldots\ldots\ldots (1)$$

where I_L is the light current, I_0 is the reverse saturation current and n is the diode ideality factor, which can all be dependent on bias voltage and temperature. However, for an ideal diode n being constant and I_0 is only dependent on temperature. Usually, n has a value between 1 and 2.

The short-circuit current $I_{SC} = I|_{V=0}$ and the open-circuit voltage $V_{OC} = V|_{I=0}$ are measured from the I–V characteristics. The series and shunt resistance are calculated using following equations:

$$R_s = \left[\frac{dV}{dI}\right]_{V=V_{OC}} \quad \text{..... (2)}$$

$$R_{sh} = \left[\frac{dV}{dI}\right]_{I=I_{SC}} \quad \text{..... (3)}$$

The fill factor and efficiency are evaluated using standard equations:

Fill factor $FF = \frac{I_m V_m}{I_{SC} V_{OC}}$ ..... (4)

and efficiency ($\eta\%$) = $\frac{P_{out}}{P_{in}} = \frac{I_{SC} x V_{OC} x FF}{P_{in}}$ ..... (5)

The spectral response (SR) measurement of a solar cell is one of the richest in information tests currently performed in design and fabrication processes. The spectral response at a given wavelength is defined as

$$SR(\lambda) = \frac{J_{ph}(\lambda)}{I(\lambda)} \quad \text{..... (6)}$$

where $J_{ph}(\lambda)$ is the total photogenerated short circuit current density at a given wavelength and $I(\lambda)$ is the spectral irradiance of the incident light. In state of the art solar cells, the photogenerated current can be approximated by the short-circuit current, which is then measured at several wavelengths using monochromatic light from a filtered light source.

6.3 Experimental Details

The p-SnS/n-CdS nanostructured based heterojunction solar cells are prepared using doctor blade technique. To fabricate the complete cell structure, initially CdS nanorods thin films are prepared on indium tin oxide (ITO) coated glass substrates. These samples are dried for 10-12 h at 60 °C. SnS nanoflakes thin layers are then deposited on the dry CdS layers again by doctor blade technique and these samples are dried for another 10-12 h at 60 °C. A silver (Ag) paste dot is then made on SnS layer which is used as back contact while ITO is used as transparent electrode. The p-SnS/n-CdS heterojunctions thus have the following structure: Glass/ITO/n-CdS/p-SnS/Ag which is shown in Figure 6.3. Thicknesses of the CdS

and SnS layers are in the range of 1-1.5 μm and 1-3 μm respectively as measured by cross-sectional SEM images. I-V characteristics of the three different solar cells are observed under dark and illumination. The light is shone through the glass side on the cell structure. Spectral response of the solar cells is also measured at different wavelengths by monochromator.

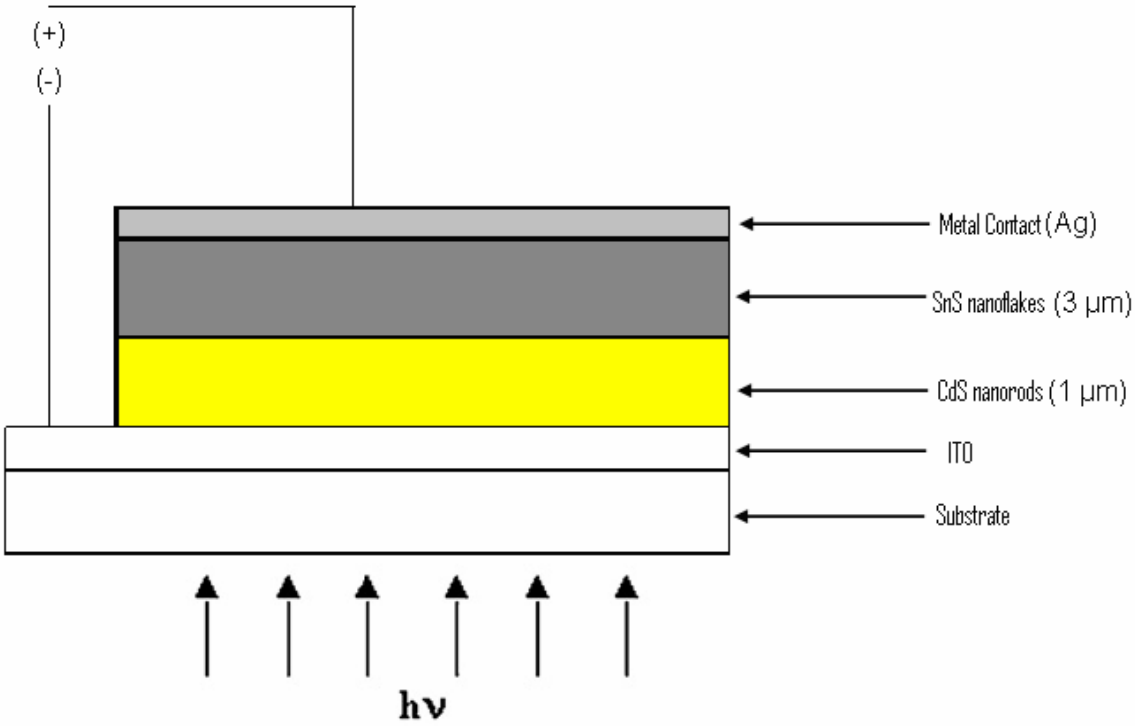

Figure 6.3: Schematic diagram of the SnS/CdS based heterojunction solar cell.

6.4 Results and Discussions

Figure 6.4 shows the I-V characteristics of the p-SnS/n-CdS nanostructured based heterojunction solar cells which are fabricated for the present studies. The light is shone through ITO coated glass substrate. Different physical parameters of the SnS/CdS solar cells are obtained which are tabulated in Table 6.1. Maximum short circuit current of 240 μA, open circuit voltage of 100 mV and efficiency of 0.32% are obtained for cell-1. Series and shunt resistances of the three different cells are in the range of 166-545 Ω to 2.0-5.7 kΩ respectively. Fill factors of these cells are varying from 0.43 to 0.65.

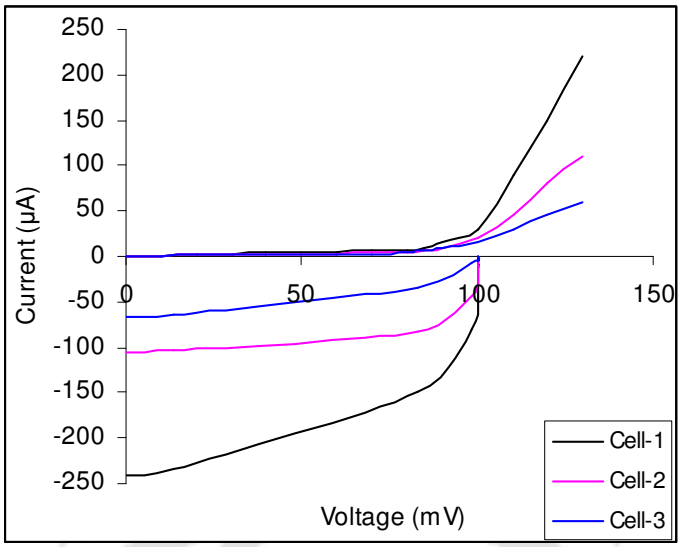

Figure 6.4: I-V characteristics of the three different SnS/CdS based heterojunction solar cells.

Table 6.1: Parameters of nanostructured SnS/CdS based heterojunction solar cells

Sample	Short circuit current (I_{sc}) (μA)	Open circuit voltage (V_{oc}) (mV)	Fill Factor (FF)	Series resistance (Ω)	Shunt resistance (kΩ)	Efficiency (η%)
Cell-1	240	100	0.52	166	2.0	0.32
Cell-2	105	100	0.65	200	5.0	0.18
Cell-3	66	100	0.43	545	5.7	0.07

Figure 6.5 shows the spectral response of the nanostructured SnS/CdS based heterojunction solar cells. The spectral response of the heterojunction is determined using monochromator and standard photodiode. The cells have a high absorptivity in the visible wavelength range of 500–900 nm, as shown in Figure 6.5. It is observed that the maximum 75% incident photons are absorbed at 600 nm of wavelength.

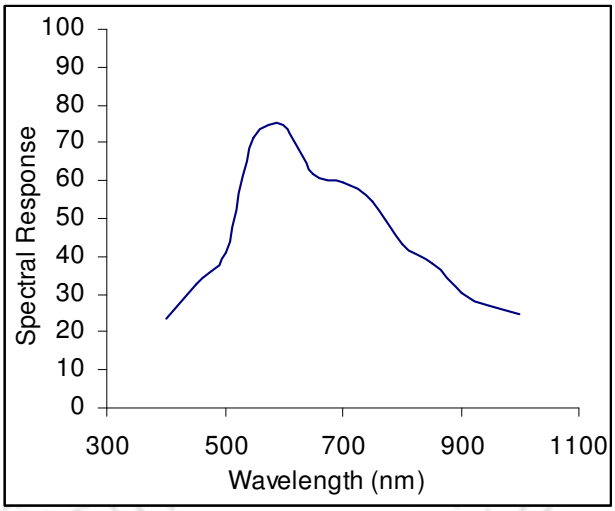

Figure 6.5: Spectral response of the SnS/CdS heterojunctions.

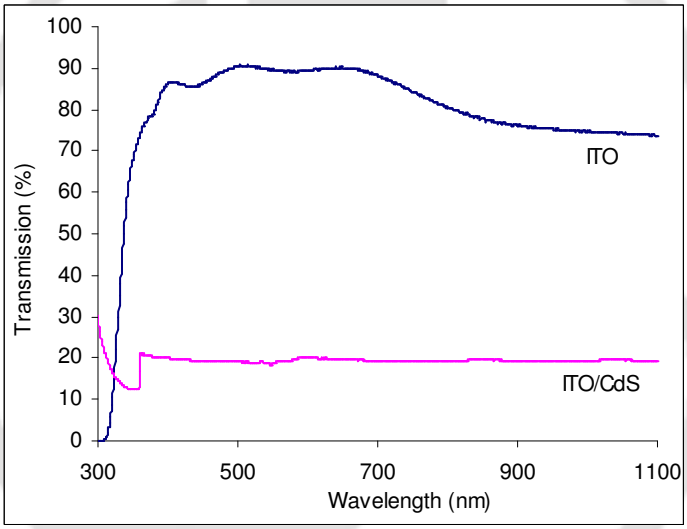

Figure 6.6: Transmission spectra of ITO and ITO/CdS glass substrates.

The efficiency obtained for these SnS/CdS heterojunction is very low compared to the other thin film solar cells. The major cause to the relatively low efficiency of the SnS/CdS heterojunction is the large value of series resistance (R_S). This is presumably because of the small grain size of the SnS thin film which is attributed to a large number of grain boundaries. These act as effective recombination centers resulting in lowering the minority carrier lifetime. The efficiency obtained for the as-prepared solar cells is much below than the theoretically predicted value (25%). The efficiency of the cells is directly related to the electron-hole pair produced in the junction of the two layers which is dependent on the incident photons. Though the transmittance of the ITO coated glass substrate is nearly about

90% which is reduced to only 20% in case of ITO/CdS coated glass substrate (Figure 6.6). Due to low incident photons, electron-hole pair produced in the depletion region is also very less. For this reason the efficiency of the cells is very low. Efficiency of the solar cells can be improved by optimizing the different physical parameters like thickness of the window as well as absorber layer and reducing series resistance.

6.5 Conclusions

Nanostructured p-SnS/n-CdS based heterojunction solar cells are successfully prepared by doctor blade technique. The efficiency obtained is much below than the theoretically predicted value; these are not far from those reported in literatures. Efficiency of the SnS/CdS heterojunctions can be improved by optimizing the thickness of the window and absorber layers and to increase in the photoconductivity and p-type conductivity of the SnS thin film. The suitable lattice matching of the window layer with high photo-response might enhance the overall efficiency of the SnS based solar cell.

6.6 References

[6.1] M. Parenteau and C. Carlone, Phys. Rev. B **41**, 5227 (1990).

[6.2] H. Noguchi, A. Setiyadi, H. Tanamura, T. Nagatomo and O. Omoto, Sol. Energy Mater. Sol. Cells **35**, 325 (1994).

[6.3] B. Subramanian, C. Sanjeeviraja and M. Jayachandran, Sol. Energy Mater. Sol. Cells **79**, 57 (2003).

[6.4] K. T. R. Reddy, N. K. Reddy and R. W. Miles, Sol. Energy Mater. Sol. Cells **90**, 3041 (2006).

[6.5] M. Gunasekaran and M. Ichimura, Sol. Energy Mater. Sol. Cells **91**, 774 (2007).

[6.6] B. Ghosh, M. Das, P. Banerjee and S. Das, Sol. Energy Mater. Sol. Cells **92**, 1099 (2008).

[6.7] S. M. Sze and K. K. Ng, *Physics of Semiconductor Devices* (3rd Edition), Wiley Interscience (2007).

CHAPTER-7

Summary and Conclusions

CHAPTER 7: Summary and Conclusions

The thesis presents the syntheses and studies of II-VI (CdS, ZnS), IV-VI (SnS, PbS) nanostructures, conjugated polymers (PPP, PF) and its blends with nanostructures for their structural, thermal, optoelectronic properties and photovoltaic applications.

The nanocrystalline CdS, ZnS, SnS and PbS semiconductors are successfully prepared using Solvothermal process with three different reaction times. PPP and PF conjugated polymers are prepared by oxidative polymerization technique and Suzuki coupling process respectively. Polymers blend with nanostructured materials are also prepared. Thin films of the nanostructured semiconductors are prepared by doctor blade technique whereas thin films of polymers and its blends with nanostructures are prepared by drop casting technique. Different characterization techniques like XRD, TEM, SEM, EDAX, UV-Vis-NIR absorbance and transmittance, PL, TGA and electrical transport are used to characterize and study various physical properties on these materials. Different models are also used to investigate and obtain their different important physical parameters. The key results and observations made during the course of study are as follows:

As-synthesized CdS powder samples consist of nanorods and the typical diameter varying from 10-50 nm and length varying from 80-750 nm. In optical absorbance spectra, a peak is observed at 488 nm which is basically due to the band to band absorption of the CdS nanorods. CdS nanorods thin films also show a sharp emission peak at 520 nm. The Raman spectra consist of a single fundamental band at approximately 312 cm^{-1} for all the samples in powder form and can be assigned to the longitudinal optical phonon (LO) mode. Thermal stability studies on these as-synthesized powder samples have shown that CdS nanorods are stable up to 650 °C. The films show a good photosensitivity ($S= \sigma_L/ \sigma_d$) $\approx 10^5$ at 300 K (under ~ 10 mW/cm^2 light from halogen lamp), which is decreased to 5.76 at 453 K. CdS thin films have also shown persistent photocurrent (PPC). The observed PPC and its slow decay with time in case of CdS nanostructured thin films have been explained by potential barrier fluctuation model. ZnS powder samples consist of disc like nanoparticles with diameters varying from 50 nm to several micrometers and surface morphology and crystallinity of the ZnS powder samples are improved with reaction times. A broad emission peak is observed at 363 nm (3.42 eV) for all the samples along with two sharp peaks at 422 nm and 439 nm for excitation wavelength at 250 nm. The dark conductivity for these nanostructure thin films is of the same order as that of bulk samples. The thermal activation energy for the dark and

photoconductivity is calculated as 1.68 eV and 1.5 eV respectively (under the illumination of 10 mW/cm^2).

SnS powder samples consist of nanoflakes with thickness varying from 50-80 nm and length varying from 200 nm to several micrometers. From TGA curves it is observed that as-synthesized SnS powder samples are stable up to 620 °C. The dark conductivity of the SnS thin films show thermally activated behavior in the temperature range from room temperature to 463 K. The activation energy from the slope of the ln σ vs 1000/T is found to be nearly 0.48 eV. The average particle size of the PbS nanocubes is found to vary from 25–300 nm with an increase in size with increasing reaction times. PbS nanocubes show good photoluminescence properties. The emission spectrum shows a broad peak at around 310 nm along with two relatively narrow peaks at 358 nm and 384 nm and a shoulder at around 430 nm for 250 and 300 nm of excitation wavelengths. The Raman spectra of the as-prepared PbS powder sample indicates seven bands in the range of 50-1100 cm^{-1}, located at around 90, 140, 180, 310, 450, 620 and 976 cm^{-1}. The I-V characteristics of the PbS thin films using silver paste exhibits ohmic nature. The conductivity is nearly constant in the temperature range 300-450 K. This is due to its low band gap.

Both PPP and PF shows blue luminescence and are suitable for blue LEDs. UV-Vis and PL titration are done on PPP solution after incorporation of CdS nanoparticles. Although no shift in peak position has been observed. The thermal stability of PPP is enhanced by adding CdS nanoparticles. The virgin PPP films are found to be highly insulating ($\sigma \approx 10^{-13}$ Ω^{-1} cm^{-1}) near room temperature. When doped with CdS nanoparticles, conductivity is enhanced by several orders of magnitude near room temperature. The activation energy for PPP-CdS blend in the range 333 to 403 K is found to be 0.68 eV. Above 403 K, when conductivity is ~ 10^{-4} Ω^{-1} cm^{-1}, the activation energy is decreased to 0.08 eV. Structural and morphological properties of the PF and its nanostructured blends are studied by XRD, TEM and SEM. The absorption peaks located in the range from 378 to 390 nm are due to π-π* transition of conjugated polyfluorene backbone. Onsets of absorption spectra of the PF incorporated with nanostructured materials is found to have shifted to 393 nm (corresponding band gap 3.16 eV) in dilute chloroform solution, whereas in thin film, absorption peaks are centered at 390 nm. In emission spectroscopy, two peaks are observed at 411 and 433 nm respectively for pure PF dilute chloroform solution for the excitation wavelength of 370 nm. In case of thin films, emission peaks are observed at 421 and 441 nm respectively. In comparison with dilute solutions, the emission spectra of polymers in film state are slightly

red-shifted and can be attributed to the aggregation of polymer chains. For all the samples, I-V curves are straight lines passing through origin and suggest that evaporated Al forms an ohmic contact with polymer and its nanocomposites blends. Pure PF shows conductivity around 2.8×10^{-11} $\Omega^{-1}cm^{-1}$ at 300 K. After incorporation of nanostructured materials in PF matrix, the dark conductivity of their blends has increased slightly. No photoconductivity is observed in PF and its nanocomposites blends at room temperature under illumination of 10 mW/cm^2 of incident light.

p-SnS/n-CdS nanostructured based heterojunction solar cells are also prepared and their important physical parameters are obtained. Typical parameters for these solar cells under illumination of 100 mW/cm^2 are: Open circuit voltage (V_{OC}) = 100 mV, short circuit current (I_{SC}) = 240 μA, fill factor (FF) = 0.52, series resistance (R_S) = 166 Ω, shunt resistance (R_{Sh}) = 2 kΩ and efficiency (η) of 0.32%. Spectral response curve indicates that around 75% of incident photons are absorbed in the wavelength range of 500-600 nm. It is observed that efficiency of the cells depends on the thickness of the CdS and SnS layers. As the thickness of SnS layers is increased efficiency increase. Efficiency of the solar cells can be improved by optimizing the different physical parameters like thickness of the window as well as absorber layer and reducing series resistance.

The present investigations on II-VI and IV-VI nanostructured semiconductors and conjugated polymers have revealed that there are several aspects of interest in these materials. Band gap of these nanostructured semiconductors can be tuned with varying particle size as per the requirement of device applications. Due to good optoelectronic properties and high thermal stability these nanostructured and conjugated polymers and their alloyed would be used for different optoelectronic device fabrications like LEDs, solar cells, different kind of sensors etc. In our case, the maximum efficiency of the p-SnS/n-CdS based heterojunction solar cell is obtained only 0.32%, which is far behind the theoretical predicted value. Lots of scopes would remain to improve the efficiency of these heterojunction solar cells.

APPENDIX I: Important Properties of CdS, ZnS, SnS and PbS

TABLE I: Important Properties of CdS (at 300 K)

Sl. No.	Parameters	Values	Reference
1.	Band gap (eV)	2.41	[1]
2.	Transport properties	n-type	[1]
3.	Carrier concentration (cm^{-3})	10^{16}- 10^{19}	[2]
4.	Electron Mobility ($cm^2V^{-1}s^{-1}$)	100	[2]
5.	Resistivity (Ω cm)	10-10^{12}	[2]
6.	Refractive Index	2.51	[2]
7.	Lattice parameters (Å)	a = 4.131 c = 6.711	[2]
8.	Nearest neighbor distance (Å)	2.52	[2]
9.	Life time of carriers (sec)	$\tau_e=10^{-3}$ $\tau_h=10^{-8}$	[2]
10.	Melting Point (°C)	1475	[3]
11.	Specific heat (cal $mole^{-1}$ deg^{-1})	13.7	[3]
12.	Pressure coefficient (meV/GPa)	-5.6	[4]
13.	Exciton binding energy (meV)	29	[4]
14.	Exciton Bohr radius (Å)	28	[4]
15.	Molar mass (g/mol)	144.46	[5]
16.	Appearance	Yellow-orange solid.	[5]
17.	Density (g/cm^3)	4.82	[5]

References:

[1] S. S. Nair and M. A. Khadar, Sci. Technol. Adv. Mater. **9**, 035010 (2008).
[2] *Optical properties of semiconductors* by Moss.
[3] *Semiconducting II-VI, IV-VI, and V-VI compounds* by N. Kh. Abrikosov, V. F. Bankina, L. V. Poretskaya, L. E. Shelimova, and E. V. Skudnova.
[4] N. Herron, Y. wang, H. Eckert, J. Am. Chem. Soc. **112**, 1322 (1990).
[5] http://en.wikipedia.org/wiki/Cadmium_sulfide.

TABLE II: Important Properties of ZnS (at 300 K)

Sl. No.	Parameters	Values	References
1.	Band gap (eV)	3.54 (cubic) 3.91 (hexagonal)	[1]
2.	Density (g/cm^3)	4.090	[1]
3.	Molar mass (g/mol)	97.474	[1]
4.	Melting Point (°C)	1185	[1]
5.	Color	White to yellow	[1]
6.	Transport properties	n-type	[2]
7.	Resistivity (Ω cm)	10^{10}-10^{12}	[3]
8.	Carrier concentration (cm^{-3})	10^{16}	[3]
9.	Electron Mobility ($cm^2V^{-1}s^{-1}$)	165	[4]
10.	Lattice parameters (Å)	a = 5.41	[4]
11.	Nearest neighbor distance (Å)	2.34	[4]
12.	Refractive Index	2.4	[5]
13.	Pressure coefficient (meV/GPa)	-4.0	[6]
14.	Life time of carriers (sec)	10^{-7}	[7]
15.	Exciton binding energy (meV)	40	[8]
16.	Exciton Bohr radius (Å)	24	[8]
17.	Specific heat ($Jg^{-1}K^{-1}$)	0.527	[9]

References:

[1] http://en.wikipedia.org/wiki/Zinc_sulfide.
[2] S. S. Nair and M. A. Khadar, Sci. Technol. Adv. Mater. **9**, 035010 (2008).
[3] H. Katayama, S. Oda and H. Kukimoto, Appl. Phys. Lett. **27**, 697 (1975).
[4] http://www.semiconductors.co.uk/propiivi5410.htm.
[5] http://www.sttic.com.ru/lpcbc/DANDP/zns_adv.html.
[6] S. Ves, U. Schwarz, N. E. Christensen, K. Syassen, and M. Cardona, Phys. Rev. B **42**, 9113 (1990).
[7] X. Li, C. Fan, Z. Zhang, X. Xiao, Chin. Phys. Lett. **11**, 127 (1994).
[8] X. Wang, Y. Zhu, H. Fan, M. Zhang, B. Xi, H. Wang and Y. Qian, J. Cryst. Growth **310**, 2525 (2008).
[9] http://www.cvdmaterials.de/cvd_zinc_sulfide.htm.

TABLE III: Important Properties of SnS (at 300 K)

Sl. No.	Parameters	Values	References
1.	Band gap (eV)	1.31	[1]
2.	Transport properties	p-type	[1]
3.	Carrier concentration (cm^{-3})	10^{15}	[2]
4.	Electron Mobility ($cm^2V^{-1}s^{-1}$)	130	[2]
5.	Resistivity (Ω cm)	30	[2]
6.	Refractive Index	2.01	[2]
7.	Lattice parameters (Å)	a = 3.989 b = 4.33 c = 11.18	[3]
8.	Nearest neighbor distance (Å)	3.016	[4]
9.	Pressure coefficient (meV/GPa)	137.6	[5]
10.	Life time of carriers (sec)	10^{-2}	[6]
11.	Exciton binding energy (meV)	-	-
12.	Exciton Bohr radius (Å)	70	[7]
13.	Specific heat (J $mole^{-1}$ K^{-1})	34.47	[8]
14.	Molar mass (g/mol)	150.76	[9]
15.	Appearance	dark brown solid	[9]
16.	Density (g/cm^3)	5.22	[9]
17.	Solubility in water	Insoluble	[9]
18.	Melting Point (˚C)	882	[9]
19.	Boiling point (˚C)	1230	[9]

References:

[1] R. H. Bube, *Photoconductivity of Solids* (Wiley, New York) pp. 233, 1960.
[2] N. K. Reddy, K. T. R. Reddy, Physica B **368**, 25 (2005).
[3] JCPDS file reference number 39–354.
[4] http://cnx.org/content/m16927/latest/.
[5] N. S. Dantas, A. F. da Silva and C. Persson, Opt. Mater. **30**, 1451 (2008).
[6] A. M. Elkorashy, Physic B **168**, 257 (1991).
[7] G. H. Yue, L. S. Wang, X. Wang, Y. Z. Chen and D. L. Peng, Nanoscale Res. Lett. **4**, 359 (2009).
[8] P. Tandon and K. N. Uttam, Ind. J. Pure Appl. Phys. **47**, 725 (2009).
[9] http://en.wikipedia.org/wiki/Tin(II)_sulfide.

TABLE IV: Important Properties of PbS (at 300 K)

Sl. No.	Parameters	Values	References
1.	Band gap (eV)	0.41	[1]
2.	Transport properties	p-type	[1]
3.	Carrier concentration (cm^{-3})	10^{18}	[2]
4.	Electron Mobility ($cm^2V^{-1}s^{-1}$)	500-600	[2]
5.	Life time of carriers (sec)	10^{-6}-10^{-10}	[2]
6.	Resistivity (Ω cm)	10^{5}-10^{6}	[3]
7.	Refractive Index	4.3	[4]
8.	Lattice parameters (Å)	a=5.936	[5]
9.	Nearest neighbor distance (Å)	2.99	[6]
10.	Pressure coefficient (meV/GPa)	123.6	[7]
11.	Exciton binding energy (meV)	300	[8]
12.	Exciton Bohr radius (nm)	18	[9]
13.	Specific heat ($J\ g^{-1}\ K^{-1}$)	0.0511	[10]
14.	Molar mass (g/mol)	239.30	[11]
15.	Density (g/cm^3)	7.60	[11]
16.	Melting point (°C)	1118	[11]
17.	Boiling point (°C)	1281	[11]
18.	Solubility in water (kg/kg)	2.6×10^{-11}	[11]

References:

[1] D. E. Aspnes and M. Cardona, Phys. Rev. **173**, 714 (1968).
[2] Vysshikh Uchebnykh Zavedenii Fizika, No. 6, 64, (1970).
[3] K. M. Gadave, S. A. Jodguri and C. D. Lokhande, Thin Solid Films **245**, 7 (1994).
[4] E. D. Palik, *Handbook of Optical Constants of Solids;* Academic: Orlando, FL, (1985).
[5] JCPDS file reference number 5–592.
[6] S. Mandal and R. Pati, Chem. Phys. Lett. **479**, 244 (2009).
[7] N. S. Dantas, A. F. da Silva and C. Persson, Opt. Mater. **30**, 1451 (2008).
[8] http://www3.interscience.wiley.com/journal/77004445/abstract.
[9] J. L. Machol, F. W. Wise, R. C. Patel and D. B. Tanner, Phys. Rev. B **48**, 2819 (1993).
[10] J. Feng, J. Yan, and S. Zhou, PIERS ONLINE **3**, 847 (2007).
[11] http://en.wikipedia.org/wiki/Lead(II)_sulfide.

List of Publications

A. International Journals

1. Evolution of nanostructure with reaction time for ZnS synthesized by solvothermal process; **Gouri Sankar Paul** and Pratima Agarwal, *Physica Status Solidi (c)* (Article in Press).

2. Structural, optical and thermal studies on PbS nanocubes; **Gouri Sankar Paul** and Pratima Agarwal, *Physica Status Solidi (c)* (Article in Press).

3. Persistent photocurrent and decay studies in CdS nanorods thin films; **Gouri Sankar Paul** and Pratima Agarwal, *Journal of Applied Physics* **106**, 103705 (2009).

4. Structural and Optical Studies of CdS Nanocomposites Synthesized by Various Routes; **Gouri Sankar Paul** and Pratima Agarwal; *Journal of Nanoscience and Nanotechnology* **8**, 4188 (2008).

5. Structural and stability studies of CdS and SnS nanostructures synthesized by various routes; **Gouri Sankar Paul**, Purabi Gogoi and Pratima Agarwal; *Journal of Non-Crystalline Solids* **354**, 2195 (2008).

6. Synthesis and Study of CdS Nano-particle Doped Poly (1, 4 dihexyloxybenzene); **Gouri Sankar Paul**, Pranjol Jyoti Sarmah, Parameswar Krishnan Iyer, Pratima Agarwal; *Macromolecular Chemistry and Physics* **209**, 417 (2008).

7. Structural and stability studies of SnS nano-flakes synthesized by solvothermal process for solar photovoltaic applications**; Gouri Sankar Paul** and Pratima Agarwal; *IEEE Conference Proceedings* (DOI: 10.1109/IWPSD.2007.4472663).

B. Conference Proceedings (International)

1. Electrical transport and transient photocurrent studies on CdS nanorods thin films; **Gouri Sankar Paul** and Pratima Agarwal; *Proceedings of the International Conference on Advanced Nanomaterials and Nanotechnology (ICANN-2009)*, 9-11th December, 2009, IIT Guwahati, India (Abstract No. A-652).

2. Structural and thermal studies on PbS nanocubes; **Gouri Sankar Paul** and Pratima Agarwal; *Proceedings of the International Conference in Amorphous and Nanocrystalline Semiconductors (ICANS23)*, 23-28th August, 2009, Utrecht, The Netherlands (pp. 224).

3. Evolution of nanostructure with reaction time for ZnS synthesized by solvothermal process; **Gouri Sankar Paul** and Pratima Agarwal; *Proceedings of the International Conference in Amorphous and Nanocrystalline Semiconductors (ICANS23)*, 23-28th August, 2009, Utrecht, The Netherlands (pp. 225).

4. Structural and transport studies on nanostructured SnS synthesized by solvothermal process; **Gouri Sankar Paul** and Pratima Agarwal, *APS March Meeting 2009*, 16-20th March, 2009, Pittsburgh, Pennsylvania, USA.

5. Transport and Transient Photocurrent Studies of CdS Nanorods Thin Films for Solar Photovoltaic Applications; **Gouri Sankar Paul** and Pratima Agarwal; *Proceedings of the 18th International Photovoltaic Science and Engineering Conference and Exhibition (PVSEC18)*, 19-23rd January, 2009, Kolkata, India (pp. 169).

6. Synthesis and Structural Studies of PbS Nanocubes; **Gouri Sankar Paul**, Sandeep Bhowmik and Pratima Agarwal; *Proceedings of the International Conference on Advances in Nanotechnology (ICANAT-2008)*, 06-08th November, 2008, Raipur, India.

7. Structural and stability studies of SnS nano-flakes synthesized by solvothermal process for solar photovoltaic applications**; Gouri Sankar Paul** and Pratima Agarwal; *Proceedings of the Fourteenth International Workshop on The Physics of Semiconductor Devices*, 16-20th December, 2007, IIT Bombay, India (pp. 884).

8. Structural and stability studies of CdS and SnS nanostructures synthesized by solvothermal process; **Gouri Sankar Paul**, Purabi Gogoi and Pratima Agarwal; *Proceedings of the International Conference in Amorphous and Nanocrystalline Semiconductors (ICANS22)*, 19-25th August, 2007, Colorado, USA.

9. Optical and Transport Studies of CdS Nanocomposites Synthesized by Various Routes; **Gouri Sankar Paul** and Pratima Agarwal; *Proceedings of the Advanced Nano Materials*

– *ANM 2007, International Conference in Experimental Condensed Mater Physics*, 8-10th January, 2007, IIT Bombay, India (pp. 146).

10. Synthesis and characterization of CdS nanoparticles doped Poly (para-phenylene); **Gouri Sankar Paul**, Pranjol Jyoti Sarmah, Parameswar Krishnan Iyer and Pratima Agarwal, *Proceedings of the International Workshop on Physics of Mesoscopic and Disordered Materials, MESODIS 2006*, 4-8th December, 2006, IIT Kanpur, India.

C. Conference /Symposium/ Workshop Proceedings (National)

1. Transport Properties Studies of Nanostructured SnS Thin Films; **Gouri Sankar Paul**, Bappaditya Pal and Pratima Agarwal; *Proceedings of the 53rd DAE Solid State Physics Symposium*, pp. 457, 16-20th December, 2008, BARC, India.

2. Synthesis and studies of SnS nano-flakes synthesized by solvothermal process for application as a solar photovoltaic material; **Gouri Sankar Paul** and Pratima Agarwal; *Proceedings of the 52nd DAE Solid State Physics Symposium*, pp. 389, 27-31st December, 2007, University of Mysore, Karnataka, India.

3. Transport Properties Studies of the CdS Nanorods Thin Film Prepared by Thermal Evaporation Technique; **Gouri Sankar Paul** and Pratima Agarwal, *Proceedings of the 51st DAE Solid State Physics Symposium*, pp. 699, 26-30th December, 2006, Barkatullah University, Bhopal, India.

****

Addendum

1. The Objectives of The PhD Work (To be added as 1.4a at the end of section 1.4 page no. 21)

Main objectives of the present thesis work are as follows:

(a) To synthesize CdS, ZnS, SnS and PbS nanostructures by solvothermal process for different reaction times and to observe the evolution process of nanostructured semiconductors.

(b) To investigate the PPP and PF conjugated polymers and their blend with various nanostructured semiconductors.

(c) To study the structural, optical, thermal and electrical transport properties of these materials.

(d) To fabricate and study the p-SnS/n-CdS nanostructured based heterojunction solar cells.

2. Optical and Electrical Characterizations

(A) Optical Characterization (To be added in sub-section 2.4.2, page no. 32)

a) UV-Visible Transmittance and Absorbance

The absorbance and transmittance of any kind of materials can be expressed by Beer-Lambert Law, which is given below:

Beer-Lambert Law

The law states that there is a exponential dependence between the transmission (or transmissivity), T, of light through a substance (Figure A.1) and the product of the absorption coefficient of the substance, α, and the distance the light travels through the material (i.e. cuvette width in case of solution and thickness in case of film), ℓ. The absorption coefficient can, in turn, be written as a product of a molar absorptivity of the absorber, ε, and the concentration c of absorbing species in the material.

For liquids and solids, these relations are usually written as

$$T = I/I_0 = e^{-\alpha \ell} = e^{-\varepsilon \ell c} \quad \text{..... (A.1)}$$

where I_0 and I are the intensity (or power) of the incident light and that after the material, respectively.

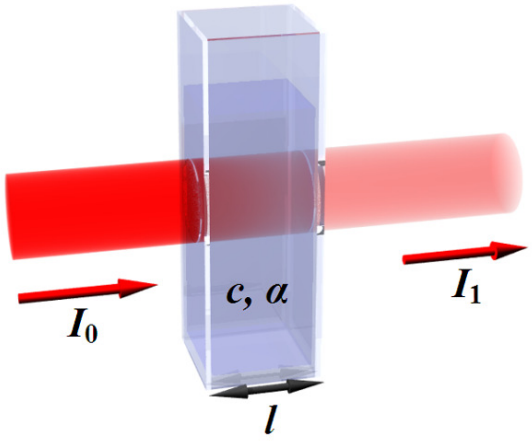

Figure A.1: Diagram of Beer–Lambert absorption of a beam of light as it travels through a cuvette of width ℓ.

The transmission (or transmissivity) is expressed in terms of an absorbance which for liquids and solids is defined as

$$A = - \ln (I/I_0) \quad \text{..... (A.2)}$$

This implies that the absorbance becomes linear with the concentration (or number density of absorbers) according to

$$A = \varepsilon \ell c = \alpha \ell \quad \text{..... (A.3)}$$

Thus, if the path length and the molar absorptivity are known and the absorbance is measured, the concentration of the substance can be deduced.

In the present thesis work, UV-Vis-NIR spectrophotometer (Shimadzu UV 3101PC) is used to determine the absorption or transmission of UV-VIS light (200 to 1100 nm) by a sample (powder in solution form or thin films). For measurements of transmittance and absorbance, powder samples are ultrasonically dispersed in ethanol for 3 h and then placed in a quartz cuvette. For absorbance and transmittance measurements of thin films, samples are placed in a sample holder and then scan for the wavelength range of 200-1100 nm. Step size of the data reading is 1 nm. Band gap of the semiconductors are calculated from the onset of change in curvature of the UV-Vis absorption spectra.

b) Photoluminescence

Photoluminescence (PL) is a process in which a substance absorbs photons ($h\upsilon > E_g$) and then re-radiates photons of lower energy. Quantum mechanically, this can be described as an excitation to a higher energy state and then return to a lower energy state accompanied by the

emission of a photon. This is one of many forms of luminescence (light emission) and is distinguished by photoexcitation (excitation by photons), hence the prefix *photo-*. The time period between absorption and emission is typically extremely short, of the order of 10 nanoseconds.

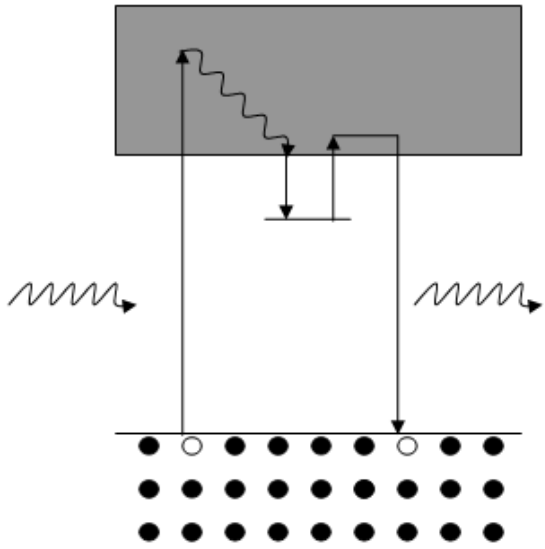

Figure A.2: Excitation and recombination mechanism in photoluminescence with a trapping level for electrons.

In PL spectroscopy, when solution and thin films of the materials are excited by monochromatic photon flux, then photons with energy more than band gap are absorbed and electrons are excited to the conduction band. These electrons then recombine with holes either directly via band to band transition or via defects levels. The energy of emitted photons is the characteristic signature of the various transitions. The energy of the photons emitted during recombination via defect levels is smaller than that in case of band to band transition. Therefore, from PL spectra, we can calculate the corresponding band gap and defects levels associated with the vacancies of the materials.

PL measurements are carried out by Aminco Bowman Series 2 Luminescence Spectrometer in case of our powder and thin film samples. For PL measurements of the powder samples, powders are ultrasonically dispersed in ethanol for 3 h and then placed in a quartz cuvette. Optical filters (450 nm, 500 nm) are used at the emission site to cut the higher order harmonics of the excitation wavelength. Photoluminescence excitation (PLE) is also measured with a fixed emission wavelength (e.g. 520 nm for CdS nanorods thin films). Step size of the data reading is 1 nm.

c) Raman Spectroscopy

Study of Raman effect is particularly important in elucidating molecular structure. The mechanism of Raman scattering is different from that of infrared absorption, and Raman and IR spectra provide complementary information. If a molecule is irradiated by monochromatic light of frequency υ, then, because of electronic polarization induced in the molecule by this incident light, light of frequency υ (Rayleigh scattering) as well as of $\upsilon \pm \upsilon_i$ (Raman sacttering) is emitted (υ_i represents a vibrational frequency). Thus the vibrational frequencies are observed as Raman shifts from the incident frequency υ in the ultraviolet or visible region.

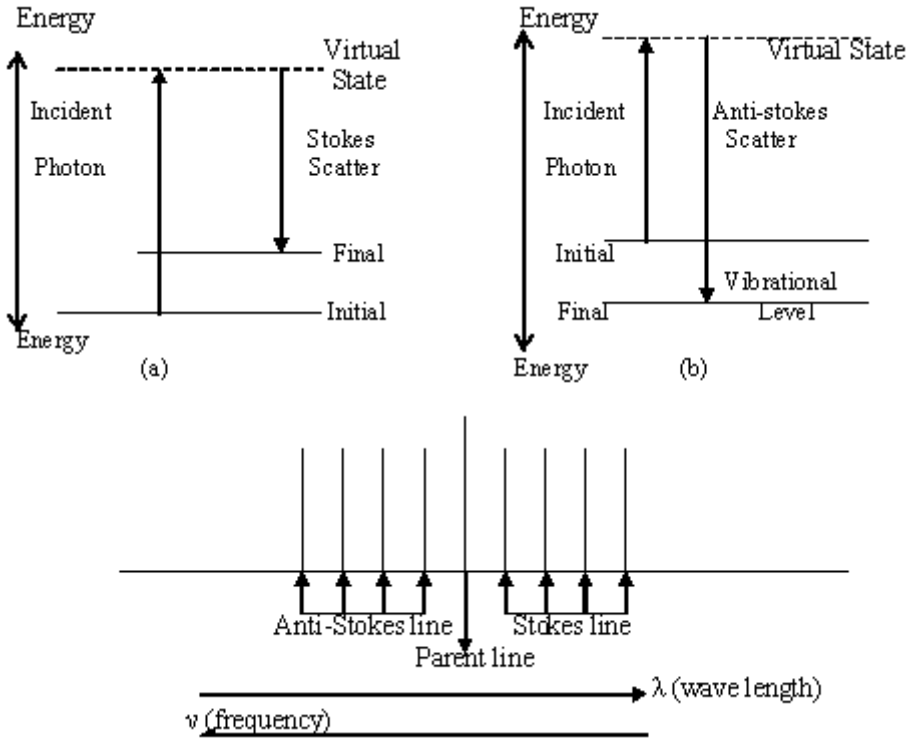

Figure A.3: Energy level diagram for Raman scattering; (a) Stokes Raman Scattering (b) Anti-Stokes Raman Scattering.

From Raman spectra different phonon vibrational modes such as longitudinal optical (LO), transverse optical (TO) and transverse acoustic (TA) and longitudinal acoustic (LA) are observed and these are assigned by the reported literatures.

In this thesis work, Raman spectroscopy of all the as-synthesized powder samples are observed by Lab RAM HR instrument excited by 488 nm of Ar ion laser with 2 mW incident power. The spot size of the incident laser is around 5 μm and the laser exposure times are

varying from 20-120 sec. Data is recorded in the range of 50-1500 cm^{-1}. Peak positions of the CdS, ZnS, SnS and PbS nanostructured powder samples are assigned by the reported data.

(B) Electrical Characterization (To be added after sub-section 2.4.4, page no. 37)

Electrical Characterizations of the thin films of nanostructured sulfide materials, polymers and their blends are done on two different geometry - one is coplanar and other is sandwich geometry. Conductivity of the samples in coplanar geometry is calculated by equation (A.7).

$$J = \sigma E$$

$$\sigma = \frac{J}{E} = \frac{I/A}{V/d} = \frac{I.d}{t.l.V} \quad \text{..... (A.4)}$$

where J is the current density, σ conductivity, E applied electric filed, I measuring current, d separation between electrodes, t thickness, l electrode length and V applied voltage.

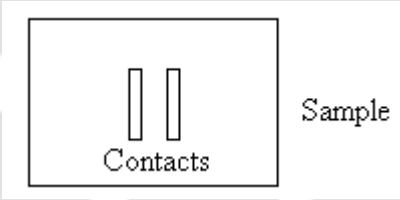

Figure A.4: Coplanar geometry

In case of sandwich geometry, separation between two electrodes is thickness (t) of the films which is around few μm and spot size of the top electrode is around 3 mm. Conductivity of the samples in sandwich geometry is calculated by equation (A.8).

$$J = \sigma E$$

$$\sigma = \frac{J}{E} = \frac{I/A}{V/t} = \frac{I.t}{\pi r^2.V} \quad \text{..... (A.5)}$$

here r is the diameter of the top electrode.

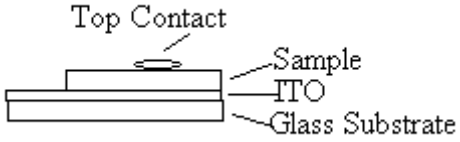

Figure A.5: Sandwich geometry

3. Equation 2.2 (page no. 31) in Chapter 2 is stroked out.

4. Origin of PL peaks for PbS nanocubes (To be added after sub-section 4.3.2(b) in page no. 87)

Figure 4.13(a) and Figure 4.14(a) shows the respective UV-Vis absorbance and PL spectra of the solution of PbS nanocubes prepared for three different reaction times in spectroscopic grade ethanol. Figure 4.13(a) is the normalized absorbance with respect to wavelength and this is not valid for band gap calculation. Similar kind of UV-Vis absorption spectra also observed by Trindade et. *al* [A.1] in PbS nanoparticles in toluene solution. Lead sulfide being a narrow band gap material offers large tunability. Band gap of PbS can be varied in a wide range, up to 2.3 eV, from the bulk value of 0.41 eV, by changing the mean cluster size of the nanoclusters [A.2]. From Figure 4.13(b) it is observed that for 4 h sample transmission is much more than the 1 h and 2 h samples and drastic change is observed at 300 nm. In case of 4 h sample, different particle sizes are observed. Due to this large particle size distribution, bigger particles are settled in the bottom of the solution for higher molecular weight of the PbS and incident photon flux is transmitted through the relatively lower particle size which are dispersed in solvent, which results in the higher transmittance. In Fig. 4.14 a, PL peaks observed in PbS solution are basically due to sulfur vacancies present in the PbS nanocubes and these are not representing the band to band transitions.

References

[A.1] T. Trindade, P. O'brien, X. M. Zhang and M. Motevalli, J. Mater. Chem. **7**, 1011 (1997).

[A.2] F. W. Wise, Acc. Chem. Res. **33**, 773 (2000).